NUMERICAL AND EXPERIMENTAL INVESTIGATION OF CRYO-FREEZING WITH LARGE BLOOD VESSELS

GE MENGYI

(B.Eng., Peking University, China)

A THESIS SUBMITTED

FOR THE DEGREE OF DOCTOR OF PHILOSOPHY

DEPARTMENT OF MECHANICAL ENGINEERING

NATIONAL UNIVERSITY OF SINGAPORE

2016

DECLARATION

I hereby declare that this thesis is my original work and it has been written by me in its entirety. I have duly acknowledged all the sources of information, which have been used in the thesis.

This thesis has also not been submitted for any degree in any university previously.

Ge Mengyi

July 2016

ACKNOWLEDGEMENTS

I would like to express my deepest gratitude to my supervisors Prof. Shu Chang, Prof. Chua Kian Jon, Ernest, Prof. Yang Wenming, who offered me the opportunity to join this project, welcome me as a member of the research group and gave me the chance to study and discover in Singapore. Their guidance and immense knowledge helped me in my research, and my research could not be accomplished without their supervision.

I would like to thank the members in Thermal Process Lab 1 (TPL1) and Energy Conversion Lab at NUS. Thanks for their incredible support and encouragements. I would like to thank the Department of Mechanical Engineering at NUS for the financial support during my pursuit of the PhD.

A special thanks to my family. Words cannot express my gratitude to my father, mother, and beloved husband for the sacrifices that they've made on my behalf. I would also like to thank all of my friends who supported me in many ways and incented me to strive towards my goal.

Ge Mengyi

July 2016

TABLE OF CONTENTS

SUMMARY

Cryosurgery is accepted as a favorable treatment option for eradicating undesirable cancerous tissue due to its minimally invasive nature. To perform a cryosurgical procedure successfully, it is important to monitor the in vivo growth of the ice-ball with high accuracy to avoid insufficient or excessive freezing. However, treating tumors with large volume, irregularly shaped tumors and tumors embedded with large blood vessels may cause insufficient freezing, which is the major reason for tumor survival.

A finite difference study of a biological liver tissue undergoing cryo-freezing using the immersed boundary method (IBM) is presented in this thesis. The liver tissue is treated as a non-ideal material having temperature-dependent thermophysical properties. The influence of heating effect due to blood flow (through the vessel surface) has been investigated by applying the boundary condition-enforced IBM. Results indicated that the heat source term due to the blood flow in the vessel embedded in the bioheat transfer equation significantly impacts the tissue temperature profiles and thermal gradient histories. In addition, the ice fronts, namely, 0 ℃ and -40 ℃, progression can vary by as much as 35% at 500s, when the distance between the cryoprobe and the major blood vessel varies. This work has also demonstrated that applying the IBM to a bioheat model focusing on tissue cryo-freezing is highly appropriate as far as the analysis of tissue freezing in the vicinity of major blood vessels is concerned.

The effects of the blood vessel structure and injected nanoparticles on the cryo-freezing of a clinically-extracted vascular tissue are numerically investigated. Based on the measured experimental temperature field, the numerical results agreed quite well with the experimental data. This improved cryo-freezing model is able to significantly simplify the mesh generation process at the boundary resulting in improved computational efficacy. For simulating the temperature profile of a tumor which is sited in a dominantly vascularized tissue, our model is able to capture with ease the thermal effect at junctions of the blood vessels. We also analysed the effects of blood vessel complexity and nanoparticles on ice-ball deformation which cannot be easily quantified through clinical experiments. Results indicated that the thermal effects of large blood vessels, especially for a more complex blood vessel boundary, remarkably affect the temperature and deformation distributions. In addition, the numerical results showed that, the inclusion of nanoparticles enlarged the cryo-freezing area as they enhance the thermal conductivity and thermal capacity of tissue.

LIST OF TABLES

LIST OF FIGURES

NOMENCLATURE

c	Specific heat
d_n	The diameter of the branches
d_p	Particle diameter
h	Local volumetric/interfacial convective heat transfer coefficient
Δh	The uniform mesh size
$\bar{h}$	Interfacial layer thickness
k	Thermal conductivity
k_{eff}	Effective thermal conductivity tensor
k'	The thermal equilibration parameter (0 or 1)
l_n	The length of the branches
N	The number of the branches
P	The perimeter of the selected blood vessel
Q	Virtual boundary heat flux
q	Heat source
q'''_m	Metabolic heat rate
q_l	Latent heat
T	Temperature
T_{ml}	Lower phase transition temperatures of tissue
T_{mu}	Upper phase transition temperatures of tissue

T^*	The predicted temperature
ΔT	Temperature correction
T_x	The minimum temperature on the horizontal mid-plane
T_y	The minimum temperature on the vertical plane
t	Time
Δt	Time step size
$\vec{v}$	Blood velocity
$\mathbf{x}$	Eulerian coordinates
x, y, z	Coordinate components for the Eulerian mesh
$\Delta x, \Delta y, \Delta z$	Mesh spacing
$\mathbf{X}$	Lagrangian coordinates
X, Y, Z	Coordinate components for the Lagrangian point

Greek symbols

α	Irregularity
β	Blood vessel complexity
δ	Dirac delta function
ε	Porosity
ρ	Density
τ_q	Phase-lags arising due to thermal inertia
τ_θ	Phase-lags arising due to micro-structural interaction
$\mathbf{\Phi}$	The nanoparticle concentration
ω	The blood perfusion rate per unit tissue volume

Subscripts

a	Arterial blood
b	Blood
f	Frozen tissue
m	Metabolism
p	P-norm
t	Tissue
u	Unfrozen tissue

Abbreviation

CFD	Computational Fluid Dynamics
DNS	Direct Numerical Simulation
FDM	Finite Difference Method
FEM	Finite Element Method
FVM	Finite Volume Method
IBM	Immersed Boundary Method
IIM	Immersed Interface Method
RHS	Right Hand Side
TC	Thermocouple

This page has been left blank intentionally.

Chapter 1

Introduction

This chapter introduces the necessity on the study of cryosurgery with large blood vessels using the immersed boundary method. The general ideas of the cryosurgical technique and immersed boundary method are briefly described. The objectives and the scope of the study are also given in Chapter 1.

Chapter 1 Introduction

1.1 Background: General Description of Cryosurgical Technique

Hepatocellular carcinoma (HCC) is the most common malignancy worldwide, with the survival rate of 25 %-30 % [1, 2], especially in East Asia. It is the second most frequent cause of cancer death in men, and sixth for women. Currently, the common cancer treatments include surgical resection, chemotherapy, radiofrequency ablation and cryosurgery. Compared with conventional therapies, cryosurgery can reduce pain, minimize bleeding, simplify surgical complications and thus decrease the post-surgical recovery time. Hence, cryosurgery has been applied to treat several types of cancer, which has provided positive results recently.

However, due to the heating effect between large blood vessels and cancerous tumor tissue, it has become a major challenge to completely freeze the target tumor. The local recurrences at the site of cryoablation proximate to large blood vessels have been reported at the rates from 5 % to 44 % or even higher [3, 4]. The major reason for this recurrence after cryoablation is the untreated tumor cells around large blood vessels. Furthermore, the possibility of unexpected complication rises if the adjacent blood vessels are correspondingly damaged. Consequently, various research studies have been devoted specifically to investigate the convective effects of large blood vessels near solid tumors.

To better understand the thermal effects of blood vessels, numerical investigations have been conducted. Kim *et al.* [5, 6] and Xue *et al.* [7] conducted

different finite element models (FEM) to analyze the temperature distribution and heat transfer with or without large blood vessels. Experimental validation of the model by Kim *et al.* was conducted with good agreement up to 99.2%. Besides the FEM, commercially available softwares (CFDRC, FLUENT etc.) have also been applied to investigate the influencing neighboring blood vessels, which affect the tissue temperature profiles during cryoablation. Such commercial softwares are more convenient to apply for heat transfer problems with the complex computational geometry. Nevertheless, the method usually suffers from the complexity involved in regenerating the mesh to conform to the boundary due to direct implementation of boundary condition.

The conventional body-fitted mesh generation method strongly couples the solution of governing equations with the implementation of boundary conditions. To address this issue, an immersed boundary method (IBM) was first proposed by Peskin [8] in 1972. This method employs Cartesian Eulerian grid points for the solution of governing equations and Lagrangian points to represent the boundary of immersed objects. This decoupling of Cartesian mesh points and Lagrangian mesh points enables IBM with the advantages of mathematical simplicity and easy implementation.

On the basis of the achievements of IBM in the area of computational fluid dynamics, trials have been made to extend the method to thermal flow problems. Reported studies have shown that incorporating a heating term to the energy equation to involve a heat source effect was feasible. However, similar to the conventional IBM, the introduced heat source term in the energy equation is

calculated explicitly, so the temperature condition on the boundary is not accurately satisfied. To solve this problem, Ren *et al.* [9] conducted extensive research on the application of the implicit IBM to convection problems, in order to implement the boundary conditions. The boundary heat source is evaluated implicitly so that the temperature at the boundary, interpolated from the corrected temperature field, satisfies the given temperature condition.

The purpose of present thesis is to develop an efficient numerical method which applies IBM to cryosurgical simulation by adding a heat source in the bioheat transfer equation. To the best of our knowledge, this is the first time for such an application to be developed. We also conduct in vitro experiments to analyze the influence of thermally significant blood vessels and injected nanoparticles.

The subsequent section provides an overview of the numerical analysis of cryosurgery using IBM with large blood vessels. A more detailed discussion of previous and on-going research on the numerical analysis will be presented in Chapter 2.

1.2 Objectives and Scope of the Study

The brief introduction and literature survey in Chapter 1 show that remarkable works have been done on the development of cryo-freezing analysis and the heat transfer problem using the immersed boundary method. However, there are still rooms for the improvement of the numerical method in cryo-freezing technology and these stimulate the studies in the present thesis.

In this study, a new model combining the Pennes bio-heat transfer model and the

IBM is proposed to study the cryo-freezing of the tumor embedded biological tissue with large blood vessels. By adding a heat source in the bio-heat transfer equation, the thermal effects of large blood vessels in cryosurgery can be considered separately. This is equivalent to making a correction to the temperature field. The temperature correction is considered as unknown and determined implicitly, which equalizes the corrected boundary temperature and the temperature condition. This new model is appropriate to analyze cryo-freezing process for two-dimensional (2D) and three-dimensional (3D) problems. To validate such models, we also conduct the in vitro experiments to analyze the influence of thermally significant blood vessels, including the diameter of blood vessels, the flow rate of blood and the injection of nanoparticles. Both the 2D and 3D validation studies are taken, and the blood vessel complexity and the ice ball irregularity are introduced to quantify the surgical efficiency.

Additionally, we also compare the three different bio-heat transfer models with experimental results. For the validation, to reduce the computational tediousness, a two-dimensional calculation will be taken in x-y plane and the mathematical formulation will be established based on the following assumptions:

(1) The phase transition of the biological tissue during freezing occurs between T_{ml} and T_{mu}, where T_{ml} and T_{mu} are the lower and upper phase transition temperatures of the tissue, respectively;

(2) The heat source due to perfusion and metabolism, when the tissue is unfrozen, is considered;

(3) The surrounded healthy tissue is assumed as homogenous during simulation;

(4) The thermal properties of the tissue and tumor are temperature-dependent.

1.3 Contributed Papers

[1] **MY Ge**, KJ Chua*, C Shu, WM Yang, Simulation of three-dimensional model for vascular system in a real clinical problem, *Journal of Thermal Biology (Under Review)*

[2] **MY Ge**, KJ Chua*, C Shu, WM Yang, Numerical analysis of a clinically-extracted vascular tissue during cryo-freezing using immersed boundary method, *International Journal of Thermal Sciences 110, 109-118, 2016.*

[3] **MY Ge**, KJ Chua*, C Shu, WM Yang, Analytical and numerical study of tissue cryofreezing via the immersed boundary method, *International Journal of Heat and Mass Transfer 83, 1-10, 2015.*

1.4 Thesis Overview

The thesis contains 8 chapters. The detailed context in each chapter is summarized as follows:

Chapter 1 introduces the necessity on the study of cryosurgery with large blood vessels using the immersed boundary method. The general ideas of the cryosurgical technique and immersed boundary method are briefly described. The objectives and the scope of the study are also given in Chapter 1.

Chapter 2 gives a detailed literature review based on the content mentioned in Chapter 1. Both the development of cryosurgery technology and the development of the immersed boundary method are introduced. The numerical methods in analyzing the cryo-freezing with large blood vessels are discussed in detail.

Chapter 3 describes the mathematical model to simulate the process of cryo-freezing. The Pennes bio-heat transfer model, the dual-phase-lag model and the porous model are introduced and discussed in this chapter. The governing equations and boundary conditions of such models are introduced. The predictor-corrector procedure of the boundary condition-enforced IBM, which is applied to satisfy the boundary condition of the blood vessels, is presented in detail. The computational sequence is summarized as a flow chart.

Chapter 4 mainly describes the major experimental facilities, measurements, operating procedures and uncertainties of the experiments. A series of experiments have been conducted with topics on the performance of a conventional cryosurgical system, effects of crucial parameters such as the blood vessel system, the blood vessel diameter, the blood flow rate and the injection of nanoparticles, during cryosurgery. The uncertainties of the measurements are also given. The experiments are designed to validate the feasibility and efficacy of the developed numerical method for cryosurgery.

Chapter 5 is about the model modification. This chapter presents our work on validating the finite difference numerical model of a biological liver tissue undergoing cryo-freezing using the immersed boundary method (IBM). The liver

tissue is treated as a non-ideal material having temperature-dependent thermophysical properties. The influence of heating effect due to blood flow has been investigated by applying the boundary condition-enforced IBM. The validation study shows that the model can successfully predict the temperature distribution during cryo-freezing. Further results have indicated that the heat source term due to the blood flow in the vessel embedded in the bio-heat transfer equation significantly impacts the tissue temperature profiles and thermal gradient histories.

Chapter 6 describes the numerical investigation on the effects of the blood vessel structure and injected nanoparticles during the cryo-freezing of a clinically-extracted vascular tissue. A hybrid two-dimensional finite difference analysis combined with immersed boundary method has been developed to accurately simulate the cryo-freezing process. Based on the measured experimental data, the numerical results agreed well with the experimental data. This improved cryo-freezing model is able to significantly simplify the mesh generation process at the boundary resulting in improved computational efficacy. For simulating the temperature profile of a tumor which is sited in a dominantly vascularized tissue, this model is able to capture with ease the thermal effect at junctions of the blood vessels.

Chapter 7 studies the clinically-extracted vascular tissue for 3D problems using the iterative immersed boundary method. The experimental validation with various configurations of blood vessels was conducted. The results show a satisfactory agreement with the numerical results. The vascular complexity and the ice-ball shape irregularity are analyzed and compared for both the 2D and 3D with different vessel configurations and developments.

Chapter 8 summarizes the conclusions and the contributions to the knowledge in this dissertation. Besides, the limitations associated with this study are discussed. Several recommendations are proposed for the future work.

This page has been left blank intentionally.

Chapter 2

Cryosurgical Technique and its Numerical Study: Literature Review

This chapter is devote to the literature review based on the content mentioned in Chapter 1. Both the development of cryosurgery technology, especially in numerical methods, and the development of the immersed boundary method are introduced. The numerical methods in analyzing the cryo-freezing with large blood vessels are discussed in detail.

Chapter 2 Cryosurgical Technique and its Numerical Study: Literature Review

2.1 Cryosurgical Technique

2.1.1 Cryosurgical Technique Development

Tumors are the malignant growth by abnormal and uncontrolled cells [10], which will be considered as to be benign when the growth is limited in one spot [11]. When a tumor spreads to other parts of the body, grows invading and destroys other healthy tissues, it is deemed to be malignant and the process is coined as metastasis [12]. To our knowledge, tumors can be broken down into solid tumors (organ tumors) and liquid tumors (blood cancers). This dissertation focuses on the treatments for solid tumors.

Different cancer treatments, which include chemotherapy, radiotherapy, hormonal therapy, biological therapy and surgical removal, are available and usually used in conjunction with one another. However, such treatments tend to have undesirable side-effects such like weakening immune system. Hence, an effective treatment named cryotherapy, which could kill tumors thoroughly while producing less side-effects, is therefore greatly desired.

The first publication of using extreme cold for the destruction of tissue refers back between 1819 and 1879 [13]. The physician in Brighton Infirmary used a mixture of salt and ice for palliating tumors. In 1899, Campbell White advocated liquid air for treatments, which is the first time employing refrigerants for the medical application [14]. Based on studies on the freezing media, eventually, the

liquid nitrogen becomes one of the most accepted freezing medium in cryosurgery [15] and amount of studies [16-19] in cryobiology have taken about the cooling effects of liquid nitrogen in the past decades.

Another important element in cryosurgery is the cryo-device because the low temperature should be delivered by it. Dates back to the early 1960's, the first generation of cryo-devices is proposed by Gondor *et. al.* [20], in which liquid nitrogen can be poured. However, due to the high rate of complications and poor accuracy, the designs were abandoned, and the applicable cryoprobes were merged. The mechanism of the cryoprobe which is based on Joule-Thomoson principle reduces the diameter to a range of 8 mm. Nowadays, owing to the development of manufacturing technology, the cryoprobe with small diameter facilities the invasive process during cryotherapy.

With its development, the latest technologies associated with cryosurgical systems provide two methods to deliver freezing media. One method is that the cryoablation can be generated by spraying the freezing medium directly on the targeted tissue [21, 22]. There are some available products spraying the freezing medium to treat benign skin lesions (i.e. CryoProbe™, H&O Equipments Inc., Belgium). However, due to the risk of gas embolism, the type of cryoablation has limited applications [23]. Another method is a non-contact gas expansion method, which is accomplished by most cryosurgeries nowadays. The method separates the freezing medium from cancer cells by a cryoprobe. The cryoprobe normally houses a coaxial inner tube [24, 25]. The downstream of the inner tube contains a small chamber enclosed within the tip of cryoprobe. The design has demonstrated

significant improvements on the controlling of the freezing process and it has avoided the risk of gas embolism.

Now therefore, in a typical cryosurgery process, the undesired tissue will undergo liquid-solid and reverse phase transformation in the freezing/thawing region. Successful cryosurgery means maximizing destruction of cancerous cells while minimizing cryoinjury to the surrounding healthy tissue.

However, even with the mentioned advantages of using cryosurgery for treating tumors and the significantly improved performance of cryo-devices, there are still several challenges to ensure a successful cryosurgery.

2.1.2 Challenges of Cryosurgery

Clinical data suggests that conventional cryosurgery is still not efficient in the treatment of complex tumors, with high recurrence rate taking place in the following checkups [26]. This mostly occurs when attempting to treat tumors with large volume or irregularly shaped tumors as shown in Figure 1. Current cryosurgery method has either inadequately over-strong freezing effects or the inability to produce a desirable ice-ball shape to totally enwrap the target tumor. In addition, it has been suggested that the cooling rate of cryosurgery is not sufficient enough to produce the intracellular ice crystals in tumor cells, especially at the tumor edge [27]. Such limitations mean that cryosurgery cannot guarantee total lethal damage to the target region.

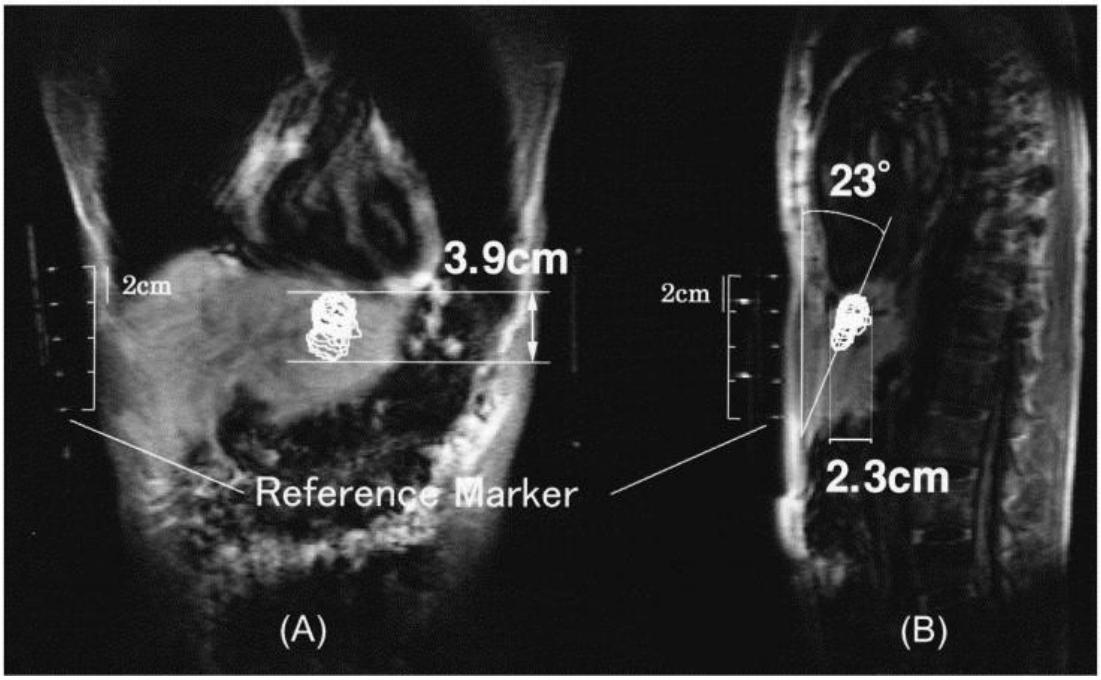

Figure 1 An irregular tumor in the liver with a maximum size of 3.9 cm. [28]

Another key issue that limits the widespread use of cryosurgery is the difficulty in eliminating the destruction volume of cancerous tissue while minimizing cryoinjury to its surrounding healthy tissue. Moreover, the depth of the ice-ball and the location of the critical isotherm (the one that marks total cell destruction) have to be empirically estimated and this significantly reduces the accuracy of the treatment process. Consequently, various experiments [29] and numerical simulations [1, 5-7, 29-34] have been conducted to investigate the thermal and kinetic behaviors of tissues during the ablation process.

Due to the heating effect between large blood vessels and cancerous tumor tissue, it has become another major challenge to completely freeze the target tumor. Insufficient freezing, which will lead to the untreated tumor cells around large blood

vessels, is the major reason for tumor survival which results in many local recurrences [6, 35, 36]. From the viewpoint of heat transfer, a large blood vessel (also termed a thermally significant vessel) denotes a vessel larger than 0.5 mm in diameter [6, 37, 38]. Anatomically, tumors are often situated close to or embedded with large blood vessels, since a tumor's quick growth ultimately depends on nutrients supplied by its blood vessel network. As is well known, the blood flowing through large blood vessels acts as a heat source or heat sink and plays an important role in affecting temperature profiles of the cooled or heated tissue [39, 40].

During cryosurgery, the blood flow inside a large vessel represents a heat source that heats the nearby frozen tissue and, thereby, limits freezing lesions during cryosurgery. Furthermore, the possibility of unexpected complication will arise if the adjacent blood vessels are correspondingly damaged. Under this condition, a part of the vital tumor cells may remain in the cryolesion and lead to recurrence of tumors after cryosurgical treatment. More specifically, tumor cell survival in the vicinity of large blood vessels is often correlated with tumor recurrence after treatment [41].

Consequently, it is difficult to implement an effective cryosurgery when a tumor is contiguous to a large blood vessel. In fact, the heating effects of large blood vessels on the surrounding tumor tissue during cryosurgery can be eliminated by vascular exclusion [36, 42] in which vascular inflow occlusion is performed by clamping the entrance of the large vessels. However, the vascular occlusion requires a major surgical procedure, which will exclude one of the main merits of minimally invasive percutaneous cryosurgery.

In view of this, it is necessary to understand the effects of branched blood network on the temperature responses of tissue subjected to control freezing. Various research works have been devoted specifically to investigate the convective effects of large blood vessels, particularly the vessels with diameter above 0.5mm.

To perform a cryosurgical procedure successfully, it is important to monitor the in vivo growth of the ice-ball with high accuracy to avoid insufficient or excessive freezing. Currently, several imaging techniques such as ultrasound, MRI and CT have been adopted in clinics to monitor a cryosurgical procedure [43]. However, none of the imaging modalities could allow the surgeon to visualize the internal thermal field of the ice-ball and locate exactly the critical isotherm [44]. Hence, numerical simulation technique is often used to obtain transient thermal field inside the target tissues as long as the boundary conditions, initial conditions and the thermal properties of the target are accurately set. This aids the surgeon in controlling and optimizing the protocol of cryosurgery.

Among the research studies, many numerical models have been formulated to simulate the heat transfer in bio-tissue [6, 7, 45-47]. However, a major limitation of these models is that they did not consider complex structures of blood vessels and their thermal impacts, especially with large vessels.

2.1.3 Numerical Studies on Cryosurgery

This section introduces the numerical studies on heat transfer problem in tumor embedded tissue during the ablation process. Most of the studies consider the influence of the large blood vessels.

Kim *et al.* [6] developed a finite element model to solve the cryosurgical problem with or without large blood vessels. Experimental validation of the model was conducted with a good agreement within 99.2%. Rattanadecho and Keangin [30] carried out the microwave ablation of porous liver samples using single slot microwave coaxial antenna. The coupled model of electromagnetic wave propagation and heat transfer analysis were solved via FEM. Xue *et al.* [7] conducted a three-dimensional FEM analysis on the behavior of knee joint's temperature distribution and heat flux from large blood vessels. Neufeld *et al.* [48] proposed a new conformal technique to reduce the staircase effects brought by the finite difference time domain (FDTD) method. The three-dimensional method has the advantage of solving heat transfer problems with complex geometry and the potential of similar applications. Considering the heat balance between the arterial blood vessel and the ambient tissue, Dombrovsky *et al*. [49] developed an advanced thermal model, which coupled both energy equations of the arterial blood temperature and the tissue temperature.

Nevertheless, the computing speed, scale and accuracy of the model, even the success of calculation are highly related to the mesh segmentation. The coupling of two energy equations will increase the complexity of the mesh construction, which will significantly affect the computational efficiency. The method usually suffers from the level of complexity involved in regenerating the mesh to conform to the boundary due to direct implementation of the boundary conditions, especially for very complex or moving boundary surface.

Besides the finite element method, other commercially available softwares, such as CFDRC and FLUENT, have been adopted to investigate the influence of neighboring blood vessels on tissue temperature profiles development during heat therapies. Solovchuk *et al.* [1] investigated the influence of blood vessels on temperature distributions during high-intensity focused ultrasound ablation of liver tumors. Zhao and Chua [31] developed a cryoablation model with clinically-extracted vascular system using FLUENT. Sun *et al.* [29] conducted both in vivo experiments and numerical investigations on nanocryosurgery of tissue with large blood vessels. He *et al*. [50] proposed a novel method which combines the ADI-FDM and the local adaptive mesh generation method. Effective simulation of thermal flows with complex geometry of vascular network presents a phenomenological challenge with the need to accurately model the bio-heat transfer problem with multiple heat-source effects. Conventional body-fitted numerical methods, which are used in the above studies strongly couple the solution of governing equations with the implementation of boundary conditions, and require tedious grid generation based on the solid boundary. Table 1 highlights the different key points between our study and several recent studies about numerical analysis of thermal effects with large blood vessels.

Table 1 Comparison among recent studies on numerical analysis of thermal effects with large blood vessels during cryo-freezing.

Literature	Simulation method	Experimental validation	Key features	Error
Kim *et al.* [6]	2D\ FEM	YES	Modified a FEM to simulate the freezing process with large blood vessels; Constructed a perfusion model with a bovine liver; Predict the maximum allowable distance between the cryoprobe and the large blood vessel	0.80% (1st trial) 0.57% and 0.83% (2nd trial)
Zhao and Chua [31]	2D\ FLUENT	YES	Developed a cryo-freezing model dedicated to tumors with a complex blood vessel network	3.4%
Sun *et al.* [29]	3D\ FLUENT	NO	Presented the first in vivo animal experiments of using nanocryosurgical modality with large blood vessels; Performed a 3-dimensional simulations on the complex freezing problems by considering large vessels	N.A.

Literature	Simulation method	Experimental validation	Key features	Error
Solovchuk *et al.* [1]	3D\ CFDRC	YES	Proposed a 3-dimensional model considering the convective cooling in large blood vessel and the perfusion due to capillary flows	N.A.
Xue *et al.* [7]	3D\ FEM	NO	Developed a 3-dimensional FEM using the anatomical CAD model of human knee joint; Focused on the thermal effects of large blood vessels; Compared some influencing factors	N.A.
He *et al.* [50]	3D\ ADI-FDM	NO	Proposed a ADI-FDM with a new irregular boundary condition algorithm to solve the Pennes bio-heat transfer equation; Introduced a local adaptive mesh approach to capture the complex boundary and reduce the staircase effects	N.A.

Literature	Simulation method	Experimental validation	Key features	Error
Jin *et al.* [51, 52]	3D\ FEM	NO	Developed a three-dimensional FEM strategy based on a MRI-reconstructed model; Provided a better understanding on the thermal lesions of RFA within thyroid domain	N.A.
Present work	2D, 3D\ IBM	YES	Analyzed the effects of blood vessel complexity and nanoparticles on ice-ball deformation based on a complex vascular network	3.04%

2.2 Immersed Boundary Method

2.2.1 Traditional Body-fitted Method

Computational fluid dynamics [54, 55], known as CFD, is a branch of fluid dynamics. It uses numerical methods to predict problems including fluid flows, heat transfers and other related phenomena. Presently, the great strides in computers have driven CFD as an important alternative to expensive experiments and bewildering theoretical fluid dynamics. The general procedure for CFD includes mesh or grid

generation, discretization of governing equations, implementation of boundary conditions and the solution of resultant equations. We can see clearly that the numerical solution strongly depends on the grid generation process and the discretization method for the governing equations.

Traditionally, when in conjunction with the classical finite difference method (FDM) and the finite volume method (FVM), the body-fitted mesh generation is often applied, which performs well and enjoys certain popularity in lots of scientific research and engineering analysis area.

Nevertheless, despite the good performance and popularity of the conventional body-fitted methods, their applications have been limited due to the geometrical complexities frequently encountered in flow problems. Many scientific and engineering practices involve bodies with complex geometries, or objects under moving and/or deformation, which would present considerable computational difficulties for the body-fitted method. That is because the mesh generation has significant impact on convergence rate, solution accuracy and CPU time. To overcome the difficulties associated with the geometrical complexity, structured curvilinear mesh [56, 57] for FDM and FVM and unstructured mesh [58-61] for FVM and FEM have been introduced.

Structured curvilinear mesh allows boundaries to be aligned with constant coordinate lines. It is capable of providing a good representation of boundaries, simplifying the boundary condition treatment and reducing the numerical "false-diffusion" errors, etc. However, during the projection process, a highly accurate

method is required to calculate the transformation Jacobian Matrix. Otherwise, additional geometrical errors will be introduced and the accuracy of the domain is thus degraded. Furthermore, the coordinate transformation is problem-dependent and tedious. Even for simple geometries, generating a good-quality body-fitted structured mesh can always be an iterative process with a substantial amount of time.

The unstructured mesh for FV and FE methods makes use of arbitrarily shaped polygons (such as triangles, quadrilaterals in two-dimension, or tetrahedral, pyramids, prisms in three-dimension) and thus offers greater flexibility to fit the complex shape of the physical domain. In addition, the grid quality and robustness can be aggravated with increasing complexity in the geometry.

On the other hand, moving boundary problems provide us an even greater challenge to grid generation, especially when they are involved with complex geometries. With the movement of bodies, the physical fluid domain changes continuously. In the view of the body-fitted concept, the grid/mesh should be moving correspondingly to conform to the configurations. However, in most cases, the computation will break down as the mesh deforms to an excessive distortion. To avoid this, successive re-meshing of the domain is required. The solution variables need to be projected from the old mesh to the new one after re-meshing. This interpolation process not only brings heavy computational burden, but also leads to undesirable degradations of solution accuracy, robustness and stability.

2.2.2 Non-body-conforming Method

To overcome the weakness of the body-fitted mesh generation method, a group of non-body-conforming Cartesian grid methods have been proposed. One of the key advantages of non-body-conforming Cartesian grid method is that it saves time and human labor on the mesh construction. For the complex boundaries, the grid complexity is relieved since the Cartesian grid is utilized, and for the moving objects, grid re-generation is not required at each time step. At the same time, most favorable properties of the structured grids are remained in the method, such as easy application of the line/block iterative method and the geometric multi-grid method.

In this way, the non-body-conforming method has attracted lots of attention in recent years, due to its ability to simulate flows involved with complex geometries or moving boundaries, and to improve the method and extend its applications, various research groups focus their studies on the non-body-conforming Cartesian grid method.

Generally, considering a regular region as its computational domain, the non-body-conforming method regards the complex geometries and/or the moving objects as interfaces or immersed boundaries in the domain. Therefore, the implementation of the boundary conditions of such method is not as straightforward as the traditional body-fitted method. As a result, based on whether the immersed boundary is treated as an interface with a finite thickness or not, the existing non-body-conforming Cartesian grid methods can be broadly classified into two categories: the sharp interface method and the diffuse interface method.

In the sharp interface method, the boundary is treated as a zero-thickness sharp interface. It includes the ghost cell method [62-64], the cut-cell method [65, 66], and the immersed interface method (IIM) [67-71]. The sharp interface methods are capable of accurately capturing the solid interfaces and enforcing the boundary conditions on them, while applying the complicated algorithms for accurate implementation of boundary conditions.

In the diffuse interface method, the effect of boundary is spread out across the interface to a thickness of the order of the mesh width. The diffuse interface method includes the fictitious domain method [72-74] and the immersed boundary method (IBM) [8, 75, 76]. Compared to the sharp interface method, the diffuse interface method is easier to acquire the irregular structure near the immersed boundaries for derivative approximation or data reconstruction scheme. This makes the diffuse interface method relatively easy to implement. The immersed boundary method is among this category and will be discussed in detail in the following section.

The early introduction of non-body-conforming Cartesian grid method is the immersed boundary method (IBM), which is a very popular and attractive diffuse interface method in the last decades. It was firstly proposed by Peskin [8] in 1972, when studying flow pattern problems in heart valves. In this study, the human heart was modeled as an elastic membrane in a rectangular flow domain. The blood flow was described by a fixed Eulerian Cartesian mesh while a set of elastic fibers was represented by Lagrangian points for the heart motion. This enables the fibers to move and to deform freely through the Eulerian mesh. To calculate the interaction between the heart and blood flow, Peskin introduced the Dirac delta function. By

solving the incompressible Navier-Stokes equations with the additional body forces on the entire domain, the velocity on the Eulerian gird is calculated. Then the heart is updated to its new shape and location according to the no-slip condition. In this way, the solution of the whole system, which includes the blood flow and the heart motion, is easily yielded. A summary of the mathematical formulation and the applications of the IBM are given by Peskin [76]. The most recent review can be found in [77] by Mittal and Iaccarino.

From the above illustration, it can be observed that this method employs Cartesian Eulerian grid points for the solution of governing equations and Lagrangian points to represent the boundary of the immersed objects. Navier-Stokes equations are solved over the entire domain as a unified system, in which both sides of the physical boundary is considered. As a result, the flexible boundaries treatment undergoing a complicated movement or shape variation is avoided by imposing a regular Cartesian grid system on the entire computational domain. The simplicity and ease of implementation through the IBM have propelled it to become an intensive academic pursuit among researchers.

Although some studies [78-85] have claimed that the momentum forces have been introduced into the governing equations to represent the influence of the immersed boundary, the immersed boundary was still treated as a sharp interface. This is quite different from Peskin's original idea. As a result, these "so-called immersed boundary methods" are not real immersed boundary methods and fall out of the scope of the present thesis.

The calculation of the body force depends on the characteristics of the immersed boundaries, which can be classified as the elastic boundaries and the rigid boundaries. The elastic boundaries [86-90] can be handled perfectly using the constitutive law which was proposed by Peskin in his original study [76]. Almost all IBM dealing with the elastic boundaries (or using a stiff spring to mimic the rigid boundaries) use a discrete delta function to spread the force to the Eulerian points.

However, for the rigid boundaries, the constitutive law is not fully applicable any more [77]. As a result, tremendous efforts have been spent to tackle the issue of how to properly calculate the force density on the solid boundaries. Based on the original idea, the IBM was then extended to simulate problems with rigid boundaries by making the spring very stiff [75] or by applying the concept of feedback control [91, 92].

Here we only focus on the direct forcing IBM for rigid boundaries. Among the IBM of this category, some researchers eliminate the use of the discrete delta function while others still use the discrete delta function to evaluate and distribute the force. The former variants of IBM usually resort to a local reconstruction of the velocity field, such as Fadlun *et al*. [93], Kim *et al.* [94], Tseng and Ferziger [62], Balaras [95], Yang and Balaras [96], etc., although the exact positions of forcing are slightly different among these works. In the other variants of IBM, the force is first evaluated at the Lagrangian points and then spread to its surrounding Eulerian grid points using a discrete delta function (Uhlmann [97], Su *et al*. [98] and Taira and Colonius [99]).

In 2000, to calculate the singular Lagrangian force density, Lai and Peskin [75] proposed a force scheme, which is assumed that the boundary points of the immersed objects were being attached to their equilibrium positions by springs with high stiffness. A restoring force will be generated according to the Hooke's law so that the boundary points will stay close to the target boundary position, when the boundary deviates from the equilibrium location. Goldstein *et al*. [22] provided a two-mode feedback forcing scheme for controlling velocity condition at the immersed boundary. This forcing term reflects the velocity difference between the desired boundary condition and the interpolated one. The approach has been employed for the simulation of low Reynolds number turbulent flows over a surface [73] and self-propelled fish-like swimming [100].

Stringent restriction on the Courant-Friedrichs-Lewy (CFL) number and the introduction of ad hoc parameters are the major drawbacks of these types of IBM. The direct forcing method was then proposed to overcome these drawbacks. In this type of IBM, the constitutive law was abandoned and the volume force is determined by a direct imposition of the velocity boundary condition.

Mohd-Yusof [101] suggested a forcing evaluation approach in which the body force was directly derived from the transformed momentum equation. Fadlun *et al*. [93] successfully applied the approach to large-eddy simulation of turbulent flow. Uhlmann [97] has successfully generalized this idea into Peskin's immersed boundary method, by incorporating the regularized delta function into the force calculation and spreading process.

Shu *et al*. [102] discovered that most of the aforementioned methods cannot accurately satisfy the no-slip boundary condition, which will lead the happening of streamlines' penetration on the solid boundary. The penetration may degrade the accuracy of the method and also the boundary force calculation. To overcome the drawbacks of the method, a velocity correction approach was proposed, where the velocity correction is made in the vicinity of the boundary points so that the no-slip boundary condition is directly enforced. Following the idea of Shu *et al*. [102], Wu and Shu [103] proposed an implicit velocity correction-based immersed boundary solver, in which the velocity correction is determined implicitly in a way that the velocity at the boundary interpolated from the corrected velocity field through the discrete delta function accurately satisfies the no-slip boundary conditions.

The popularity of IBM has been increased for flow problems with complex or/and moving boundaries. Abundant modifications and refinements have subsequently been proposed following Peskin's work in the area of computational fluid dynamics. Following the original purpose of IBM, it has been applied to study the fluid dynamics of cardiovascular physiology such as flow in heart valves [104], flow in arterioles [105], deformation of red blood cells in a shear flow [106], etc.. Besides, the method has also been applied to various biological flows including wave propagation in the cochlea of the inner ear [107], thrust generation of swimming fish [108] and lift production of flying insects [109]. A variety of applications concerning fluid-structure interaction [110], turbulent flow [111], multiphase flow [112] and multi-component flow [113] have also been reported.

In addition, there are some other studies of IBM relevant to heat transfer

problems. However, most of the thermal problems are suffering from complex or moving configuration, such like convection in buildings, solar energy systems, electronic cooling equipment, crystal growth processes and nuclear reactor. Since the basic idea of IBM is that the effect of the immersed boundary on its surrounding fluid is realized through introducing forcing terms in the momentum equations, it has a difficulty to be directly applied to heat transfer problems since they also involve the energy equation. In fact, there is relatively little work on applying IBM to heat transfer problems compared to its application for fluid dynamic problems. Nevertheless, efforts are still done to extend IBM to study the thermal flow problems with Dirichlet-type boundary conditions.

Among the most notable studies, Zhang *et al*. [114] extended the IBM for fluid flows [80] to investigate several heat transfer problems. In the similar vein of introducing a force term to the momentum equation, they incorporated a heating term to the energy equation to evolve a virtual heat source effect. Wang *et al*. [115] investigated both natural convection and forced convection problems around a stationary cylinder using a multi-direct heat source scheme, which is similar to the multi-direct forcing method [116] proposed previously for isothermal flows. To simulate the moving boundary problems with the heat transfer effect, Young *et al.* [117] combined the direct-forcing approach with moving-grid process. Feng *et al*. [118] combined direct numerical simulation (DNS) with IBM to simulate the natural convection in particulate flows. Kim *et al*. [119] studied the natural convection induced by a temperature difference between a cold outer square enclosure and a hot inner circular cylinder at different vertical locations using IBM. Later, Lee *et al*. [120]

extended the work of Kim *et al*. [119] by considering various locations of inner cylinder along horizontal and diagonal directions.

The common feature in the above work is that a heat source term is introduced in the energy equation. However, similar to the conventional IBM, the heat source term is treated explicitly and pre-calculated. As a result, the temperature condition on the boundary cannot be accurately satisfied, which would affect the accuracy of numerical results. To mitigate this problem, Ren *et al.* [9] extended the work done by Wu and Shu [103] and their previous study of boundary condition-enforced IBM for flow problems, and conducted research on applying the implicit IBM to solve thermal problems. The boundary heat source is evaluated implicitly so that the temperature at boundary, interpolated from the corrected temperature field, satisfies the given temperature condition.

Chapter 3

Mathematical Model Development

This chapter introduces the mathematical model to simulate the process of cryo-freezing. The Pennes bio-heat transfer model, the dual-phase-lag model and the porous model are introduced and discussed in detail in this chapter. The governing equations and boundary conditions of such models are introduced. To satisfy the boundary condition, the predictor-corrector procedure of the boundary condition-enforced immersed boundary method is presented in detail. The computational sequence is summarized as a flow chart.

Chapter 3 Mathematical Model Development

3.1 Bio-heat Transfer Models

Table 2 Thermophysical properties of biological tissue and blood for simulation [121]

Symbol	Definition	Unit	Value
q_m'''	Metabolic heat rate	W m^{-3}	4200
q_l	Latent heat	kJ kg^{-3}	2500
τ_q	Phase-lags arising due to thermal	s	0.001
τ_θ	Phase-lags arising due to micro-structural interaction	s	0.001
ε	Porosity	_	0.5
T_{ml}	Upper limit of phase transition	K	272
T_{mu}	Lower limit of phase transition	K	265
k_f	Thermal conductivity of frozen tissue	W $m^{-1}K^{-1}$	2.0
k_u	Thermal conductivity of unfrozen tissue	W $m^{-1}K^{-1}$	0.5
k_b	Thermal conductivity of blood	W $m^{-1}K^{-1}$	0.64
c_f	Specific heat of frozen tissue	J $kg^{-1}K^{-1}$	1800
c_u	Specific heat of unfrozen tissue	J $kg^{-1}K^{-1}$	3600
c_b	Specific heat of blood	J $kg^{-1}K^{-1}$	3850
ρ	Density of tissue	kg m^{-3}	1000
ρ_b	Density of blood	kg m^{-3}	1050
ω_b	Blood perfusion rate per unit tissue volume	kg $m^{-3}s^{-1}$	0.29
T_a	Arterial temperature	K	310
ν	Viscosity of blood	kg $m^{-1}s^{-1}$	0.001003

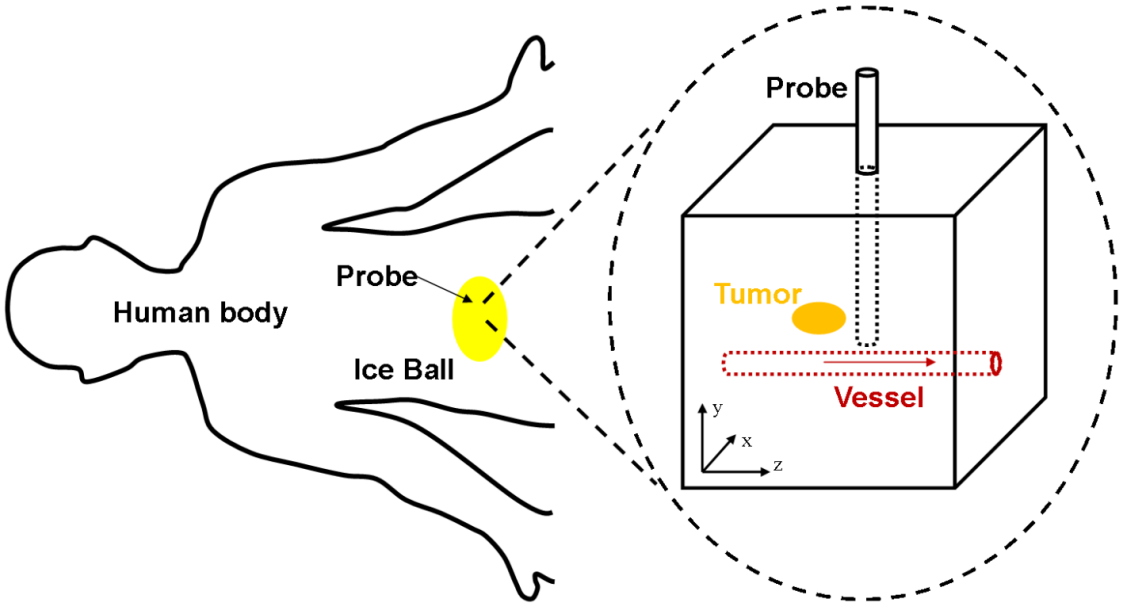

Figure 2 Schematic of the computational domain embedded with a large blood vessel

In this dissertation, the main problem we need to solve is how to efficiently freeze the liver tumor without damaging the ambient healthy tissue. A brief schematic of the computational domain is shown in Figure 2. The computational domain is embedded with a large blood vessel with the cryoprobe employed as the cooling boundary condition.

To study the heat transfer problem of bio-tissue shown in Figure 2, we first consider the classical Pennes bio-heat equation [122]. The Pennes bio-heat equation is a modified form of the transient heat conduction equation and it includes the effects of blood flow and metabolic heat generation. The equation can be described as

$$\rho_t c_t \left(\frac{\partial T_t}{\partial t} \right) = \nabla \cdot \left(k_t \nabla T_t \right) + \left(1 - k' \right) \omega_b c_b \left[T_a - T_t \right] + q_m''' \tag{1}$$

where t is the time; T is the temperature; and the subscripts t, b, a and m stand for tissue, blood, arterial blood and metabolism, respectively; ρ is the density; c is the specific heat; k is the thermal conductivity; ω is the blood perfusion rate per unit tissue volume; k' is the thermal equilibration parameter which is either 0 or 1 and q_m''' is the volumetric heat generation rate due to metabolism.

Another model, labeled as the dual-phase-lag model [123], is based on the non-Fourier's conduction law. It is known that the Fourier's law of heat conduction produces erroneous results when non-homogenous inner structure is introduced such as in the case of complex biological tissue. In other words, there exists a time lag between the cause and effect phenomena when the tissue experiences a thermal disturbance. The generalized form of the Fourier's law of heat conduction equation in a tissue is given as

$$q_t(r,t) = -k_t \nabla T_t(r,t) \tag{2}$$

The thermal lag behavior in its mathematical form can be presented either by (1) C–V constitutive equation named after Cattaneo and Vernotte [124, 125] or (2) dual-phase-lag hyperbolic conduction equation, which is presented as

$$q_t(r,t+\tau_q) = -k_t \nabla T_t(r,t+\tau_\theta) \tag{3}$$

where τ_q and τ_θ are phase-lags arising due to the thermal inertia and the micro-structural interaction, respectively. It is worth noting that both τ_q and τ_θ are material dependent parameters.

By using the first-order Taylor series expansion, the non-Fourier dual-phase-lag conduction equation can be written as,

$$q_t(r,t)+\tau_q\frac{\partial q_t(r,t)}{\partial t}=-k_t\left[\nabla T_t(r,t)+\tau_\theta\frac{\partial}{\partial t}\nabla T_t(r,t)\right] \tag{4}$$

As a result, the final resulting dual-phase-lag bio-heat model is re-produced as the following,

$$\tau_q\rho_t c_t\left(\frac{\partial^2 T_t}{\partial t^2}\right)=k_t\nabla^2 T_t+\tau_\theta k_t\nabla^2\left(\frac{\partial T_t}{\partial t}\right)-\omega_b\rho_b c_b T_t-\left(\rho_t c_t+\omega_b\rho_b c_b\tau_q\right)\frac{\partial T_t}{\partial t}+\omega_b\rho_b c_b T_a$$
$$+q_m'''+\tau_q\frac{\partial q_m'''}{\partial t} \tag{5}$$

Both the Pennes bio-heat model and the dual-phase-lag bio-heat model assume the tissue as a continuous medium. However, in 1998, Roeztel and Xuan [126] developed a two-equation bio-heat model which considered the effect of heat transfer in the porous media. They modeled the vascular region and the extravascular region (tissue and interstitial blood) separately, neglecting the local thermal equilibrium between the two media. The model introduced the interfacial convective heat transfer term instead of the perfusion term. In a similar vein, the mathematical formulations for the blood and tissue terms are

$$\varepsilon\rho_b c_b\left(\frac{\partial T_b}{\partial t}+\vec{v}_b\cdot\nabla T_b\right)=\nabla\cdot\left(k_{eff}^b\nabla T_b\right)+h_{bt}\left(T_t-T_b\right) \tag{6}$$

$$\left(1-\varepsilon\right)\rho_t c_t\left(\frac{\partial T_t}{\partial t}\right)=\nabla\cdot\left(k_{eff}^t\nabla T_t\right)+h_{tb}\left(T_t-T_b\right)+\left(1-\varepsilon\right)q_m''' \tag{7}$$

where ε is the porosity; $\vec{v}$ is the blood velocity; T is the volume averaged temperature; k_{eff} is the effective thermal conductivity tensor; h is the local volumetric/interfacial convective heat transfer coefficient.

For the isotropic conduction, k_{eff}^{b} and k_{eff}^{t} are related as

$$k_{eff}^{b} = \varepsilon k_{b} \tag{8}$$

$$k_{eff}^{t} = (1-\varepsilon)k_{t} \tag{9}$$

3.2 Mathematical Model

A dimensional schematic depicting the computational domain embedded with a large blood vessel is depicted in Figure 2. In this section, to reduce the computational tediousness, a two-dimensional calculation is taken in x-y plane and the mathematical formulation is established based on the following assumptions:

(1) The phase transition of the biological tissue during freezing occurs between T_{ml} and T_{mu}, where T_{ml} and T_{mu} are the lower and upper phase transition temperature of the tissue, respectively;

(2) The heat source due to perfusion and metabolism is considered when the tissue is unfrozen.

The parameters used in the bio-heat equations are defined as follows

$$c_b(T)=\begin{cases} c_f & T<T_{ml} \\ \dfrac{q_l}{T_{mu}-T_{ml}}+\dfrac{c_f+c_u}{2}, & T_{ml}\le T\le T_{mu} \\ c_u & T>T_{mu} \end{cases} \tag{10}$$

$$k_t(T)=\begin{cases} k_f, & T<T_{ml} \\ \dfrac{k_f+k_u}{2}, & T_{ml}\le T\le T_{mu} \\ k_u & T>T_{mu} \end{cases} \tag{11}$$

$$q_m'''(T)=\begin{cases} 0, & T<T_{ml} \\ q_m'''+q_l, & T_{ml}\le T\le T_{mu} \\ q_m''' & T>T_{mu} \end{cases} \tag{12}$$

$$\omega_b(T)=\begin{cases} 0, & T\le T_{mu} \\ \omega_b, & T>T_{mu} \end{cases} \tag{13}$$

where subscripts f and u represent the frozen and unfrozen tissue; k_f and k_u are the effective thermal conductivities of the frozen and unfrozen tissue; c_f and c_u are the effective thermal capacities of the frozen and unfrozen tissue; q_l is the latent heat when the phase change occurs.

When applying the model to solve a physical problem, the cell freezing mechanism is an important impact on the cell survival and the tumor damage. Such mechanism was originally analyzed by Mazur [28]. Following Mazur' work, Dombrovsky *et al*. [127] conducted a numerical study about modeling of repeating freezing of biological tissue. Nevertheless, our study focuses on the thermal effects of large blood vessels, and the tissue is assumed as homogenous. Therefore, the cell

freezing mechanism is out of the thesis' scope. The thermophysical properties employed in the simulations are listed in Table 2 [121].

3.3 Immersed Boundary Method

3.3.1 IBM and the Bio-heat Equation

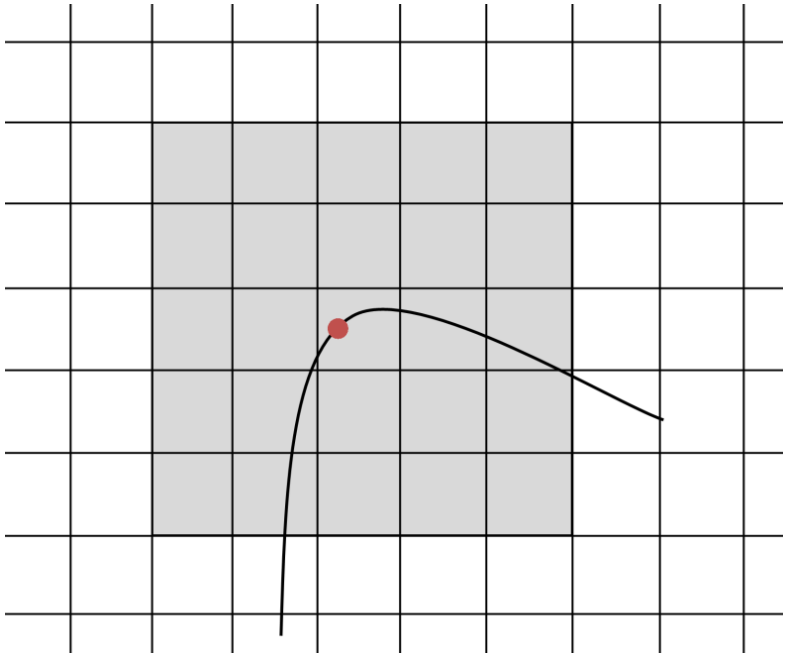

Figure 3 A two-dimensional domain containing an immersed boundary.

Firstly, we consider the Pennes bio-heat transfer equation in a two-dimensional domain Ω containing an immersed boundary Γ, as shown in Figure 3. By introducing a heat source term to the bio-heat equation, the governing equation employing IBM can be expressed as

$$\rho_t c_t \left(\frac{\partial T_t}{\partial t} \right) = \nabla \cdot \left(k_t \nabla T_t \right) + \left(1 - k' \right) \omega_b c_b \left[T_a - T_t \right] + q''' + q \tag{14}$$

The heat source term q in the equation is the heat density at the Eulerian mesh points distributed from the heat flux at the Lagrangian (boundary) points, which can be expressed as

$$q(\mathbf{x},t) = \int_{\Gamma} Q(\mathbf{X}(s),t) D(\mathbf{x} - \mathbf{X}(s,t)) ds \tag{15}$$

where $\mathbf{x}$, $\mathbf{X}$ and Q are the Eulerian coordinate, the Lagrangian coordinate and the virtual boundary heat flux, respectively.

Eq. (15) is the spreading operation which means that the summation of all heat flux along the boundary results in the total Eulerian heat source on the computational domain. Discretizing Eq. (15) is not straightforward as it involves the presence of delta function. Discrete delta functions for 2D and 3D problems are defined to effectively discretize Eq. (15).

$$D_{ij} = D\left(\mathbf{x}_j - \mathbf{X}_B^i\right) = \frac{1}{\Delta h^2} \delta\left(\frac{x_j - X_B^i}{h}\right) \delta\left(\frac{y_j - Y_B^i}{h}\right) \tag{16}$$

$$D_{ij} = D\left(\mathbf{x}_j - \mathbf{X}_B^i\right) = \frac{1}{\Delta h^3} \delta\left(\frac{x_j - X_B^i}{h}\right) \delta\left(\frac{y_j - Y_B^i}{h}\right) \delta\left(\frac{z_j - Z_B^i}{h}\right) \tag{17}$$

where Δh is the mesh size of the Eulerian coordinate, and $\delta(r)$ is defined with these following properties,

$\delta(r)$ is continuous $\quad \forall r \in R$,

$$\delta(r) = 0 \quad \forall |r| \geq 3 \tag{18}$$

$$\sum_{jeven} \delta(r-j) = \sum_{jodd} \delta(r-j) = \frac{1}{2} \quad \forall r \in R \tag{19}$$

$$\sum_{j} (r-j)^m \, \delta(r-j) = 0 \quad \forall m = 1,2,3 \text{ and } \forall r \in R \tag{20}$$

Among various functions [75], by considering the balance between the accuracy and the computational stability, one 4-point regularized delta function with the second order of accuracy proposed by Lai and Peskin [75] is chosen for our study. Adopting the scheme, we have

$$\delta(r) = \begin{cases} \frac{1}{8}(3-2|r|+\sqrt{1+4|r|-4r^2}) & |r| \le 1 \\ \frac{1}{8}(5-2|r|+\sqrt{-7+12|r|-4r^2}) & 1 < |r| \le 2 \\ 0 & |r| > 2 \end{cases} \tag{21}$$

3.3.2 Temperature Correction Procedure

Using the fractional step method, the solution can be obtained by the Predictor-Corrector steps. The detailed procedure of the Predictor-Corrector step obtaining the temperature correction is shown as the following.

(1) Predictor step:

The Predictor step solves the Pennes equation without introducing the heat source term q.

$$\rho_t c_t \left(\frac{\partial T_t}{\partial t} \right) = \nabla \cdot \left(k_t \nabla T_t \right) + \left(1 - k' \right) \omega_b c_b \left[T_a - T_t \right] + q_m''' \tag{22}$$

As a result, the predicted temperature $T^*(\mathbf{x},t)$ is obtained by solving the following equation derived from the numerical discretization method proposed under the Crank-Nicolson scheme,

$$\rho_t c_t\left(\frac{T^*-T^n}{\delta t}\right)=\frac{k_t}{2}\left(\nabla^2 T^*+\nabla^2 T^n\right)+\left(1-k'\right)\omega_b c_b\left[T_a-\frac{T^*+T^n}{2}\right]+q_m''' \tag{23}$$

(2) Corrector step:

The corrected temperature is obtained by solving the following equation,

$$\rho_t c_t\frac{\partial T}{\partial t}=q \tag{24}$$

To ensure that the temperature at the Lagrangian points interpolated from the corrected temperature T satisfies the boundary condition, (i.e. the temperature is continuous between tissue and blood vessel), we apply the implicit immersed boundary method.

By defining

$$T=T^*+\Delta T \tag{25}$$

Equation (24) becomes

$$\rho_t c_t\frac{\Delta T}{\Delta t}=q \tag{26}$$

where Δt is the time step size, T is the corrected temperature, T^* is the predicted temperature, ΔT is the temperature correction.

The discrete form of the heat source q at the Eulerian points is

$$q\left(\mathbf{x}_j,t\right)=\sum_i Q\left(\mathbf{X}_B^i,t\right)D\left(\mathbf{x}_j-\mathbf{X}_B^i\right)\Delta s_i \text{ for } (i=1,2,...,M;\ j=1,2,...,N) \tag{27}$$

Substituting Eq. (27) into Eq. (26) leads to

$$\Delta T\left(\mathbf{x}_j,t\right)=\sum_i \frac{Q\left(\mathbf{X}_B^i,t\right)}{\rho_t c_t}D\left(\mathbf{x}_j-\mathbf{X}_B^i\right)\Delta s_i \text{ for } (i=1,2,...,M;\ j=1,2,...,N) \tag{28}$$

To satisfy the physical boundary condition (which is Dirichlet boundary condition in this work), we need to ensure the temperature at the Lagrangian (boundary) points interpolated from the corrected temperature field by the delta function being equal to the specified temperature $T_B\left(\mathbf{X}_B^i,t\right)$, which is

$$T_B\left(\mathbf{X}_B^i,t\right)=\sum_j T(\mathbf{x}_j,t)D\left(\mathbf{x}_j-\mathbf{X}_B^i\right)h^2 \text{ for } (i=1,2,...,M;\ j=1,2,...N) \tag{29}$$

Substituting Eqs. (25) and (28) into Eq. (29) leads to

$$T_B\left(\mathbf{X}_B^i,t\right)=\sum_j T^*(\mathbf{x}_j,t)D\left(\mathbf{x}_j-\mathbf{X}_B^i\right)h^2+\sum_j\sum_k \frac{Q\left(\mathbf{X}_B^k,t\right)}{\rho_t c_t}D\left(\mathbf{x}_j-\mathbf{X}_B^k\right)\Delta s_k D\left(\mathbf{x}_j-\mathbf{X}_B^i\right)h^2$$
$$\text{for } (i=1,2,...,M;\ j=1,2,...N) \tag{30}$$

Eq. (30) can be summarized to the following matrix form,

$$\mathbf{AX}=\mathbf{B} \tag{31}$$

Here

$$\mathbf{A} = \frac{\Delta t}{\rho_t c_t} h^2 \begin{pmatrix} D_{11} & D_{12} & \cdots & D_{1N} \\ D_{21} & D_{22} & \cdots & D_{2N} \\ \vdots & \vdots & \ddots & \vdots \\ D_{M1} & D_{M2} & \cdots & D_{MN} \end{pmatrix} \begin{pmatrix} D_{11}\Delta s_1 & D_{21}\Delta s_2 & \cdots & D_{M1}\Delta s_M \\ D_{12}\Delta s_1 & D_{22}\Delta s_2 & \cdots & D_{M2}\Delta s_M \\ \vdots & \vdots & \ddots & \vdots \\ D_{1N}\Delta s_1 & D_{2N}\Delta s_2 & \cdots & D_{MN}\Delta s_M \end{pmatrix} \tag{32}$$

$$\mathbf{B} = \begin{pmatrix} T_B^1 \\ T_B^2 \\ \vdots \\ T_B^M \end{pmatrix} - h^2 \begin{pmatrix} D_{11} & D_{12} & \cdots & D_{1N} \\ D_{21} & D_{22} & \cdots & D_{2N} \\ \vdots & \vdots & \ddots & \vdots \\ D_{M1} & D_{M2} & \cdots & D_{MN} \end{pmatrix} \begin{pmatrix} T_1^* \\ T_2^* \\ \vdots \\ T_N^* \end{pmatrix} \tag{33}$$

$$\mathbf{X} = \begin{pmatrix} Q_B^1 \\ Q_B^2 \\ \vdots \\ Q_B^M \end{pmatrix} \tag{34}$$

After Q_B^i at all boundary points are obtained, the temperature correction δT can be calculated by substituting Q_B^i into Eq. (28).

3.3.3 Computational Sequence

The basic solution procedure of the Predictor-Corrector step can be outlined below:

1) Solve Eq. (23) to get the predicted temperature T^*.
2) Solve equation system (31) to obtain the boundary heat source $Q_B^i (i = 1, 2...M)$ at Lagrangian points and then use Eq. (28) to get the temperature correction ΔT.
3) Correct the temperature at Eulerian points using Eq. (25). Until now, the temperature field has been updated from the time level n to the time level n+1.

4) Use the corrected temperature field as the initial condition, and repeat steps (1) to step (3) for the computation of the next time level. The process continues until a converged solution is achieved (steady case) or the given time is reached (unsteady case).

Based on the solution procedure, Figure 4 shows the complete flow chart of solving the bioheat equation.

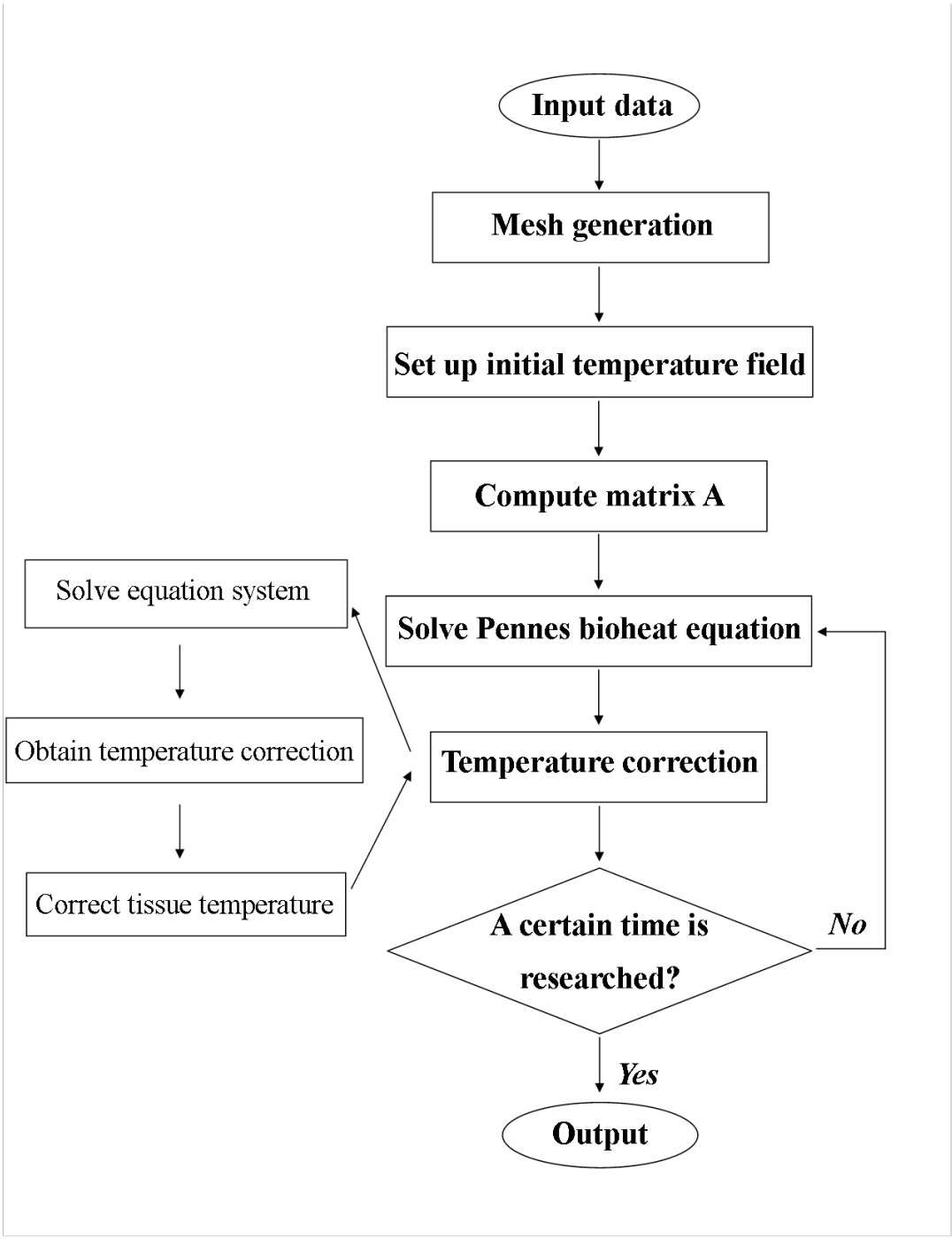

Figure 4 Flow chart of computational sequence.

This page has been left blank intentionally.

Chapter 4

Experimental Method

This chapter mainly describes the major experimental facilities, measurements, operating procedures and uncertainties of the experiments. A series of experiments have been conducted with topics on the performance of a conventional cryosurgical system, and effects of crucial parameters such as the blood vessel system, the blood vessel diameter, the blood flow rate and the injection of nanoparticles, during cryosurgery. The uncertainties of the measurements are also given. The experiments are designed to validate the feasibility and efficacy of the developed numerical method for cryosurgery.

Chapter 4 Experimental Method

4.1 Experimental Setup and Measurements

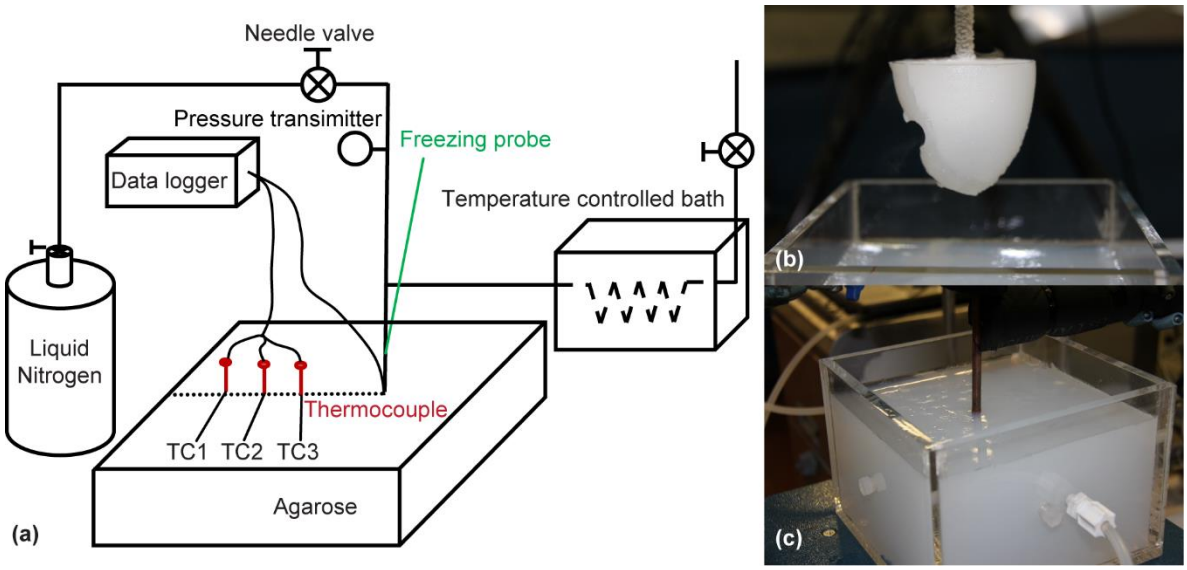

Figure 5 The experimental set-up and the layout of thermocouples.

In our experiments, the Teflon tube (2.0 mm ID, 4.5 mm ID and 10.0 mm ID with the thermal conductivity of 0.21 W/m.K) is used to simulate the blood vessel. The Liquid nitrogen (Singapore Oxygen Air Liquide Pte Ltd (SOXAL)) is used as the cryogen for all experiments. During the experiments, water from an isothermal water bath is used to simulate the blood flow. The water temperature is maintained at about 37 °C ± 1.5 °C, same as human body's temperature.

Type T (SCPSS-040U-6, OMEGA Engineering Inc., Stamford, Ct) thermocouples are used to measure the transient temperature inside the agarose. The diameter of the thermocouple is 1.6 mm. The measuring range for the thermocouple is from -200 ℃ to +350 ℃. Figure 5 illustrates the layout of thermocouples with

positions marked as TC1, TC2 and TC3. In addition, a contact thermocouple is attached to the cooling tip of the cryoprobe. Conductive adhesive transfer tapes (8805, 3M Inc., St. Paul, Mn) provide high thermal conductivity by focusing on the bulk conductivity and interface conductivity. As a result, such tapes are used to attach the contact thermocouple wire to the cooling tip of the cryoprobe. During the experiments, temperature read by different thermocouples are recorded by the data logger (34970A, Agilent Inc., Santa Clara, Ca) at every regular 10-second intervals. The temperature data is then transferred to an external computer for the post-processing

The schematic diagram of the cryoprobe and the surrounding biological tissue structure is shown in Figure 6. The cryoprobe usually contains a coaxial inner tube and an outer tube. The downstream of the inner tube is a small chamber enclosed within the cryoprobe, preventing the direct interaction between freezing medium and tissue. When the pressurized liquid freezing medium passes through the inner tube, the medium vaporizes at the small chamber. The gas-liquid flow streams back through an interlayer between the inner tube and the wall of insulation.

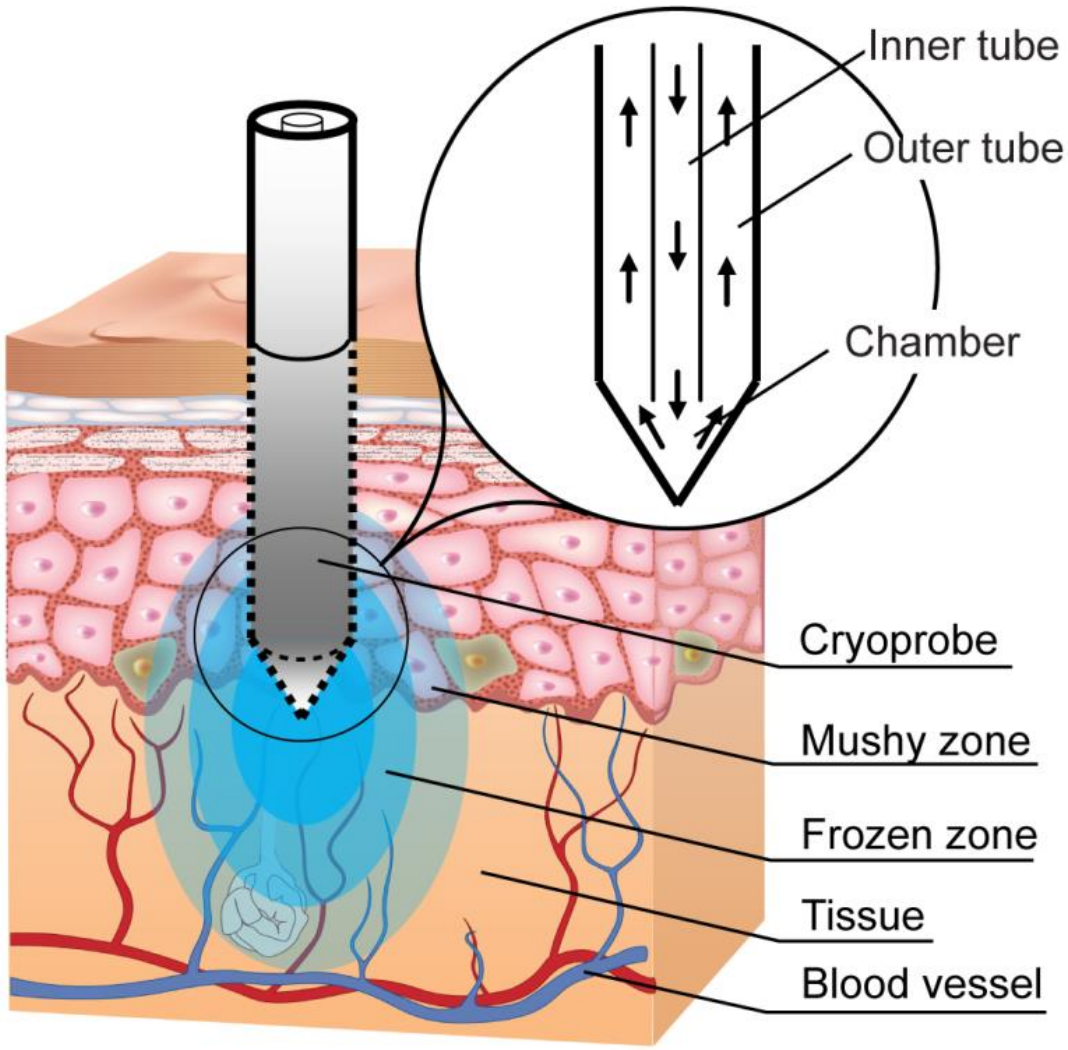

Figure 6 The schematic of tissue structure with cryoprobe.

The infrared thermography system has been employed to assist monitoring the temperatures during cryosurgery. A VarioCAM® high resolution thermographic camera (by InfraTec GmbH, Germany) (as shown in Figure 7) is occupied to map the transient temperature distribution at the agarose surface. It equips with a digital color video camera for the photographic documentation of the prevailing measuring condition. It is a thermographic system for the long wave infrared spectral range of

7.5 μm to 14 μm. The lens images the object scene onto a microbolometer array at a maximum resolution of 640×480 pixels. This camera can detect a temperature range between 233 K and 1473 K, with the temperature resolution better than 0.08 K at 303 K.

The working principle of the thermographic camera is based on the concept of emissivity. An object at a temperature higher than absolute zero emits electromagnetic radiation. The thermographic camera detects radiation in the infrared range of the electromagnetic spectrum. The auto-focusing lens embedded within the camera helps to deliver bright and rich contrast thermal images. While doing experiments, the thermographic camera should be placed at an angle above the experimental samples. Images can be acquired every 10 s and analyzed with the software of IRBIS ® Remote 3 Professional.

Figure 7 VarioCAM® high resolution thermographic camera

In our experiment, the infrared camera is placed 20 cm away above the experimental sample. Images are acquired every 60 seconds and analyzed with

IRBIS3 Professional software. Similar experiments are performed on agarose and in vitro tissue (pork liver) to demonstrate the significantly thermal effects of blood vessels on temperature distribution and ice ball profile. The different cases include cases with no large blood vessels, with a single large blood vessel and with a parallel counter-current vessel pair.

4.2 Experimental Procedure

4.2.1 Large Blood Vessel

Blood contains a large amount of water, which is shown in the study [128] that about 55% of blood is an aqueous solution containing 92% water. Therefore, blood has an average density of approximately 1060 kg/m^3, very close to water's density of 1000 kg/m^3 [129]. Due to the similar thermal properties between blood and water, there are several existing papers using water to simulate the blood flow during cryosurgery [121, 130].

In this experiment, distilled water is used to simulate the blood flow. The water temperature is controlled by a water temperature bath maintained at 37 ℃ ± 1.5 ℃. The circuit pressure driving the water flow is achieved by a peristaltic pump. The flow of water is controlled as 80 ml/min, 100 ml/min and 120 ml/min, respectively for comparison. The water flow is circulated to the Teflon tube for 10 min ahead of the commencement of freezing.

4.2.2 Agarose Platform

The study on gelatin study employs the agarose with similar thermal properties to the biological tissue and allows observation of ice front by naked eyes. The agarose platform (composed of 1% agarose (25 g) and 99% water (2475 ml) by weight) is used to simulate the biological tissue. The thermal conductivity and heat capacity of such material are shown in Table 2. Then heat up and stir the distilled water to accelerate the dissolving process. After thorough mixing and solidifying, the agarose platform samples are naturally cooled down and allowed to solidify in a clear acrylic container with dimensions of 160 mm × 160 mm × 85 mm.

4.2.3 In-vitro Tissue Study

Liver cancer in men is the second most frequent cause of cancer deaths, while in women, it is the sixth leading cause of cancer deaths [2]. As a result, the experiments are also conducted with in-vitro pork livers. Experiments tested in porcine livers have been proofed to be reliable and they have been used in many experimental studies [131-133].

4.2.4 Liquid Nitrogen

As shown in Figure 5, the liquid nitrogen flow is controlled by a high-sensitive needle valve (S8-1HM4, Swagelok Inc., Solon, Oh) and the pressure is monitored by a pressure transmitter (0-16 bar, control type 500, Huba Control Inc., Switzerland) located downstream of the needle valve. The liquid freezing medium passes into a freezing cryoprobe through a homocentric inner steel tube within the cryoprobe. When the liquid nitrogen is released at the tip of the cryoprobe, cryo-freezing is

initiated due to the fluid evaporation when its pressure drops. Then the flow is piped into a water temperature controlled bath (SAHARA S49, Thermo Fisher Inc., Waltham, Ma). The water temperature controlled bath raises the temperature of nitrogen flow and avoids unintended cryoinjury at the outlet. The pressure and the flow rate of the exhausted outlet gas are measured by a pressure transmitter (0-8 bar, control Type 500, Huba Control Inc., Switzerland) and a gas flow meter (MTF4130-D-01, Malema Sensor Inc., Boca Raton, Fl), respectively. The flow of liquid nitrogen is controlled using a needle valve to regulate flow between 150 L/min and 250 L/min.

4.3 Experimental Results and Discussions

4.3.1 Influence of Blood Flow on Freezing

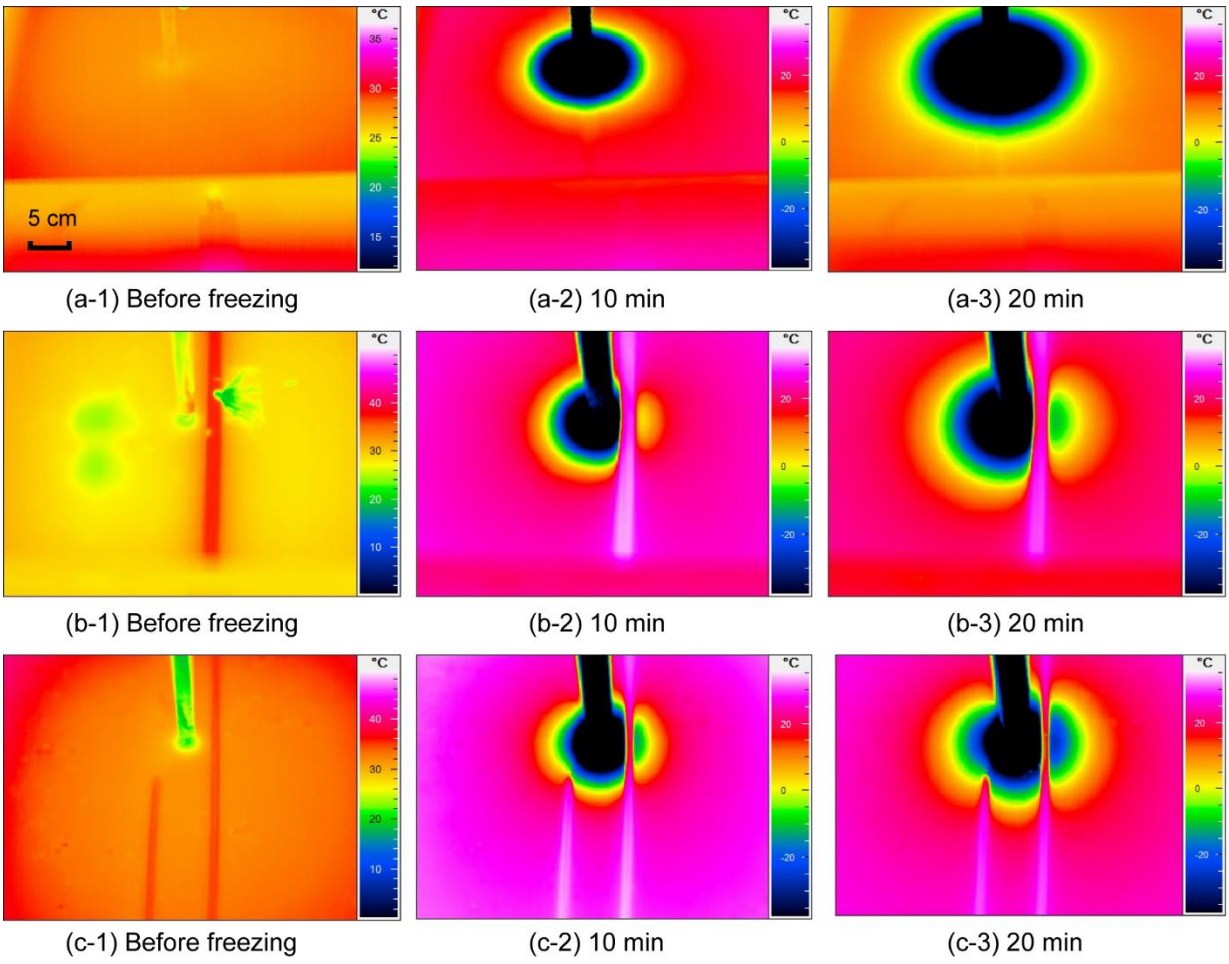

Figure 8 Infrared thermographs for agarose experiments with (a) no blood vessel, (b) a single blood vessel and (c) a parallel counter-current vessel pair. The flow rate is 80 ml/min and the diameter of blood vessel is 4.5 mm.

Experiments are conducted to analyze the influence of the blood vessels by applying different vessel structures such as no blood vessel, a single large blood vessel and a parallel counter-current vessel pair. Shown in Figure 8 are the infrared thermographs for the agarose experiments. These graphs indicate that large blood vessels have thermally significant effects on the temperature distribution and ice ball

profile. Figure 9 shows the position between thermocouples and blood vessels. All the experiments taken in the following section (Chapter 4.3.2 and Chapter 4.3.3) are based on such layout of thermocouples, blood vessels and cryoprobe in Figure 9.

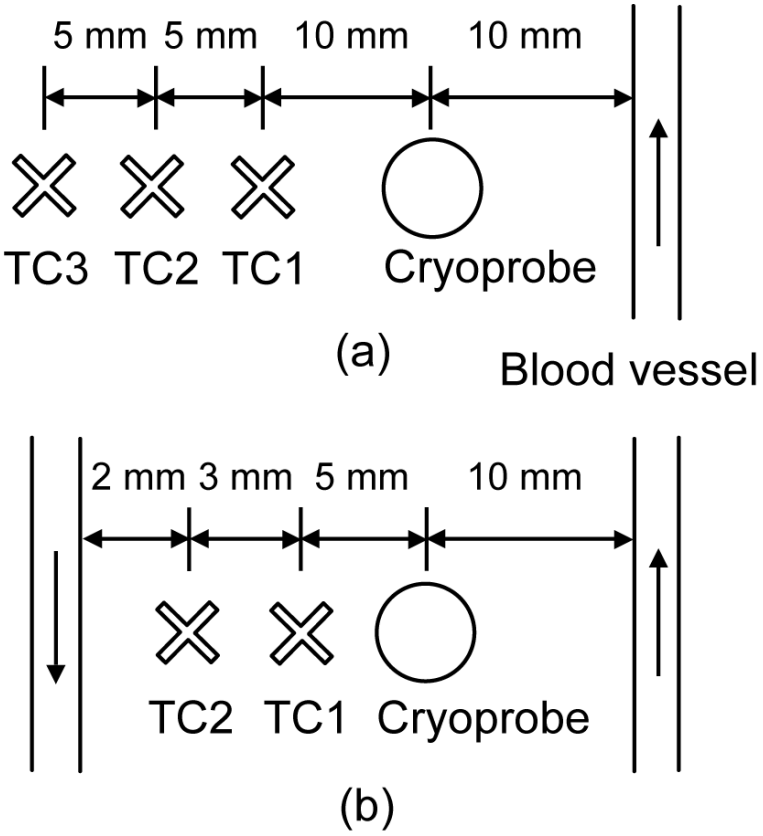

Figure 9 The layout of thermocouples, blood vessels and cryoprobe for (a) a single blood vessel and (b) a parallel counter-current vessel pair

As can be seen in Figure 8, for the case without blood vessels (Figure 8(a)), the temperature distribution appears relatively symmetrical. The isotherms observed at the surface changes stably during freezing. After 20 minutes of freezing, the maximum diameter of the ice ball measured is about 7.0 cm. For the case with a single large blood vessel in Figure 8(b), higher temperature is observed at the region closer to the blood vessel. Hence, the ice ball formation becomes irregular, appearing as a concave shape near the blood vessel. Meanwhile, the contours for 0 ℃ and -

40 ℃ are also marked in the graphs, which can clearly show us the completely freezing region and mushy region.

Anatomically, large blood vessels often appear as a counter-current pair of artery and vein. In the view of this, the thermal effects of parallel counter-current vessel pairs are investigated. The arrangement of the Teflon tubes, in this case, plays the roles of the artery and the vein. Water entering agarose container represents the arterial blood while water leaving the container can be regarded as the venous blood. The infrared thermographs for this case are shown in Figure 8(c). The temperature distribution differs notably from the case with a single blood vessel. The temperature at the downstream is significantly lower than that at the upstream.

The single blood vessel and parallel counter-current vessel pair experiments are studied to understand how the freezing process may be attenuated by blood flow as well. The ice front positions of the 0 ℃ and -40 ℃ isotherms for the two cases are given in Figure 8(b,c). It is observed that the propagation of the two isotherms (0 ℃ and -40 ℃) is relatively unaffected by the number of large blood vessels. At the end of the 20 minutes freezing cycle, the maximum radius of the lethally frozen tissue, as described by the -40 ℃ isotherm, is around 1.7 cm while the maximum freezing radius, as described by the 0 ℃ isotherm, is around 2.6 cm. Hence, it takes approximately 20 minutes to achieve the complete destruction of a tumor with 3 cm diameter. Isotherm gap, defined by the distance between two isotherms, is directly related to the cell survival of healthy tissue within the periphery region. The calculated value of isotherm gap is 0.9 cm according to the experimental results.

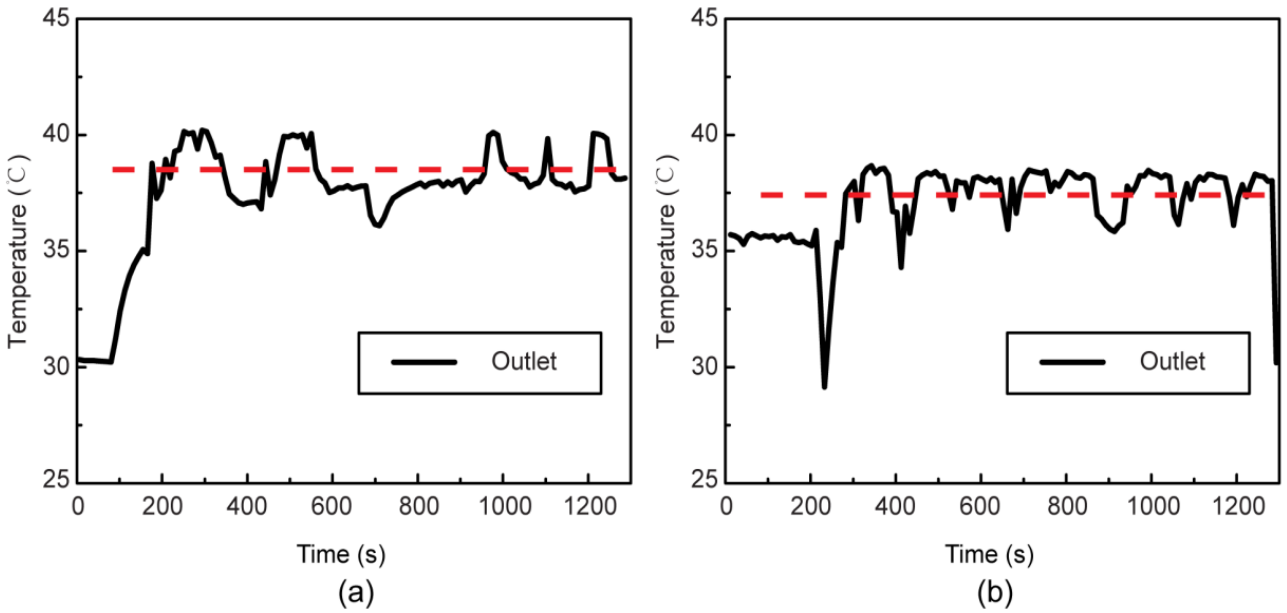

Figure 10 The outlet temperature of the blood flow during the agarose experiments with (a) a single blood vessel and (b) a parallel counter-current vessel pair. The flow rate of the blood flow is 80 ml/min and the diameter of blood vessel is 4.5 mm.

Figure 10 shows the outlet temperature of the blood flow during the experiments. As shown in Figure 10, the outlet water temperature from the experimentally-simulated blood vessel is readily observed as a relatively constant value from 200 s to 1200 s, with the inlet temperature of the blood flow is controlled as 37 ℃ ± 1.5 ℃ (calibrated mean thermocouple probes' accuracy). The average outlet temperature for the case with a single blood vessel is 38.1 ℃, while the average outlet temperature of the case with a parallel counter-current vessel pair is 37.5 ℃. This phenomenon can be adequately explained by the fact that the heat flux brought by the blood flow is much larger than the heat transferred from the blood to the ambient tissue.

Based on the results from the experiments, when the flow rate of the blood flow is 80 ml/min, our assumption pertaining to the Dirichlet boundary condition in the proposed model is met, then proving the effectiveness of the numerical method.

4.3.2 Influence of Diameter of Blood Vessels

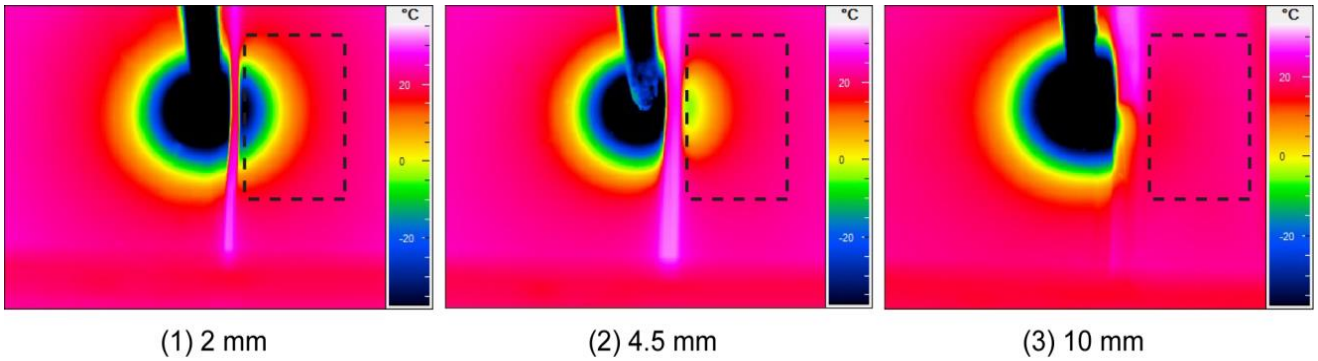

Figure 11 Infrared thermographs for agarose experiments with blood vessel diameter of (1) 2 mm, (2) 4.5 mm and (3) 10 mm, freezing for 10 mins. The flow rate of the blood is 80 ml/min.

Figure 11 shows the infrared thermographs for the agarose experiments for different blood vessel diameters after freezing for 10 mins. The diameters of the large blood vessels are set as 2.0 mm, 4.5mm and 10.0 mm, respectively, with the flow rate of 80 ml/min. With the increasing of the blood vessel diameter, the ice ball shape changes significantly, especially on the right hand side of the cryoprobe. The area is shown in the dashed rectangle. It is worth noting that the temperature in the dashed box of the case with blood vessel diameter of 10.0 mm (see in Figure 11(3)), seems barely touched by the freezing, due to the thermal effect of blood flow.

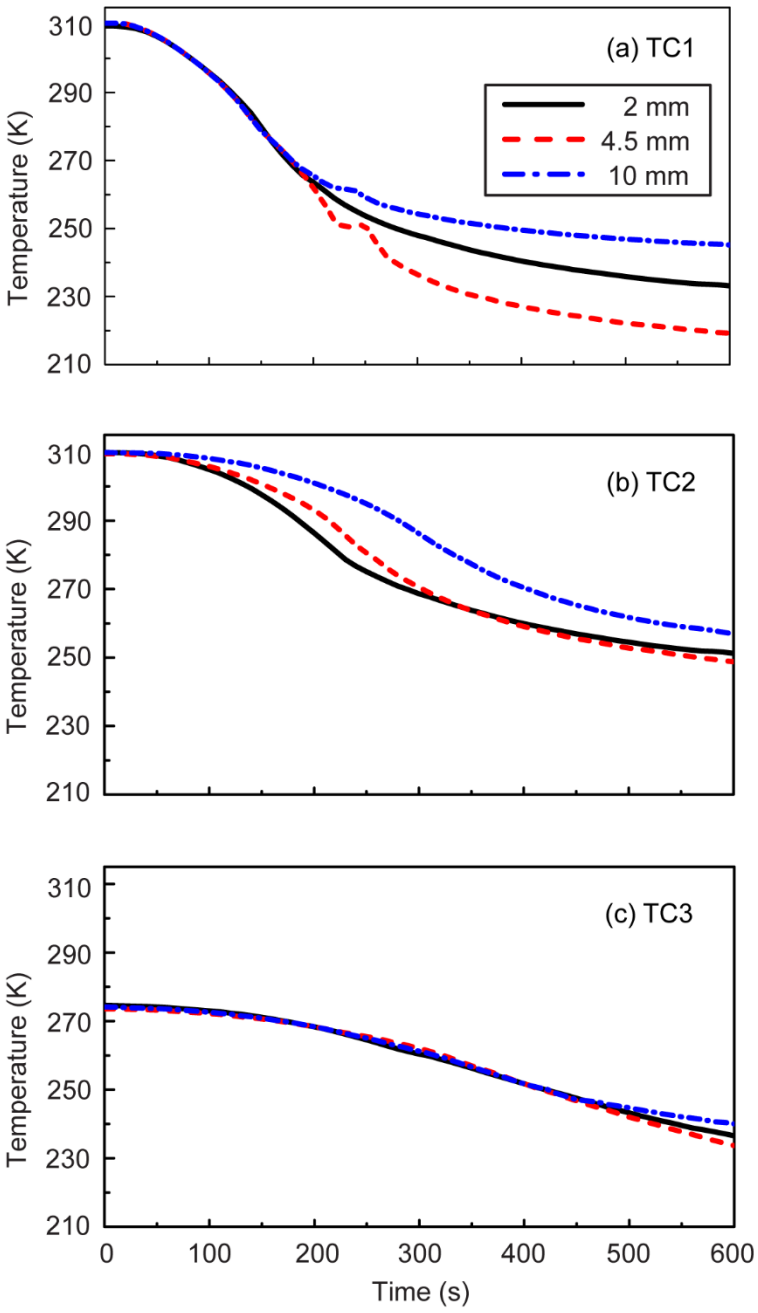

Figure 12 The temperature response measured by thermocouples for agarose experiments with a single blood vessel at (a) TC1, (b) TC2, and (c) TC3. The flow rate of the blood is 80 ml/min.

However, according to the temperature measured by thermocouples, as presented in Figure 12, it is noted that the temperature changes among cases with various blood vessel diameters are quite different. For the case with the

thermocouple closer to the blood vessel wall (see in Figure 12(a)), the temperature difference is relatively higher than the others. A possible explanation is that the temperature will be significantly affected by the thermal effect brought by the blood flow. Nevertheless, the influence can be neglected when distance between the thermocouple and the blood vessel wall is larger than 30 mm (see in Figure 12(c)).

4.3.3 Influence of Blood Flow Rate

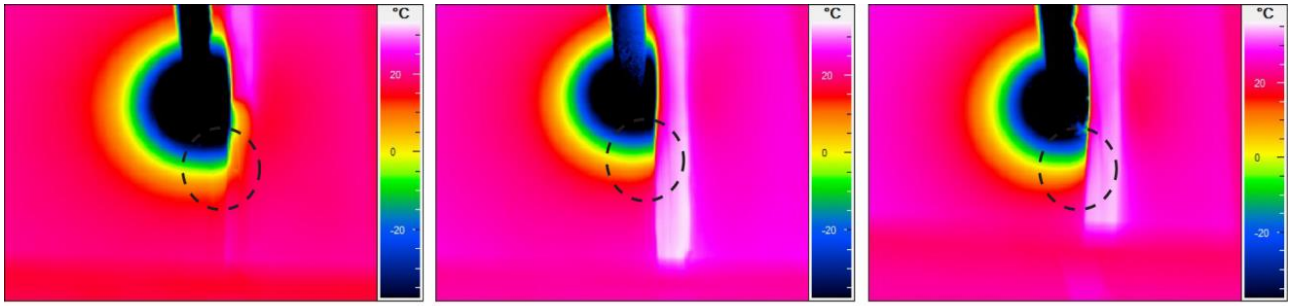

Figure 13 Infrared thermographs for agarose experiments with flow rate of (1) 80 ml/min, (2) 100 ml/min and (3) 120 ml/min, after freezing for 10 mins. The diameter of blood vessel is 10 mm.

Figure 13 shows the infrared thermographs for the agarose experiments for different blood flow rates after freezing for 10 mins. The flow rates of the blood are set as 80 ml/min, 100 ml/min and 120 ml/min, with the diameter of 10 mm. With the increasing of blood flow rate, the ice ball shape changes significantly on the right hand side. The temperature of the case in Figure 13 in the dashed circle seems obviously affected by the thermal effect of blood flow, especially in Figure 13(3). The average temperature is relatively higher for the case of 120 ml/min flow rate than the other two cases. The similar phenomenon is observed that the temperature

difference for the thermocouple closer to the blood vessel wall is relatively higher than the others.

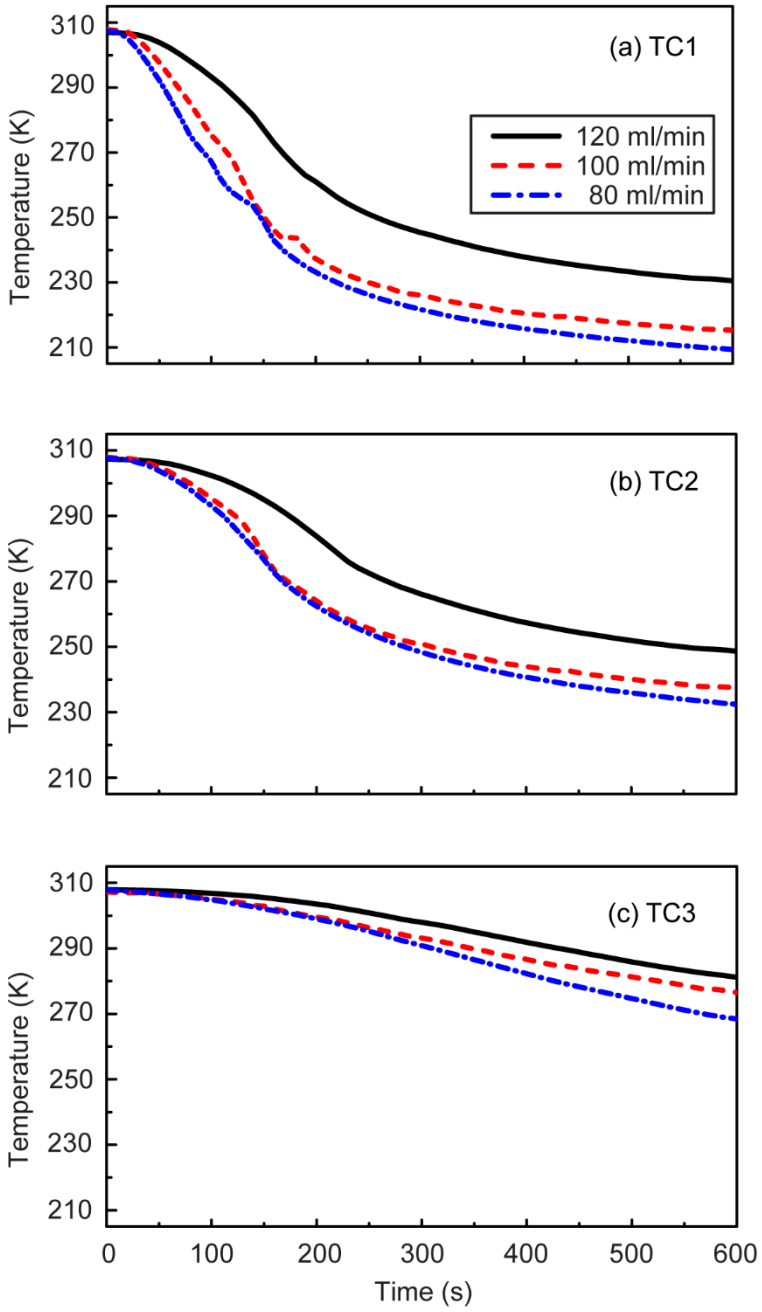

Figure 14 The temperature response measured by thermocouples for agarose experiments with a single blood vessel at (a) TC1, (b) TC2, and (c) TC3. The diameter of blood vessel is 10.0 mm.

According to the temperature response measured by thermocouples, which is shown in Figure 14, the same conclusions are drawn that the different flow rates can highly affect the temperature, especially the temperature near the blood vessel wall. It can be explained that the temperature is significantly affected by the thermal effect brought by the blood flow. Figure 14 shows clearly that larger blood flow rate can bring more heat source. However, the extent of the influence of different blood flow rates is different. The temperature responses of 80 ml/min and 100 ml/min are almost the same for three thermocouples.

4.3.4 Influence of the Injected Nanoparticles

Studies [26, 134] about cryosurgery by applying nanoparticles, found that injecting certain high thermal conductivity nanoparticle solution into localized tissue could significantly improve the freezing rate, change the formation of ice-ball, and affect the growing direction of ice-ball there. In order to better understand the thermal behaviors in tissue during a nanocryosurgical treatment, the temperature responses are measured during experiments with Fe_3O_4 and diamond nanoparticles. The results are presented in Figure 15.

In general, the injection of nanoparticles improves the freezing rate to a certain extent, as demonstrated in Figure 15. Significantly different from the influence of vessel diameter and the blood flow rate, the temperature is highly affected at the thermocouple far from the cryoprobe. The freezing rate is obviously higher when the temperature is above -30 ^{o}C than the case with temperature below -30 ^{o}C. This is due

to the fact that extremely low temperature will change the thermal properties of the nanofluid.

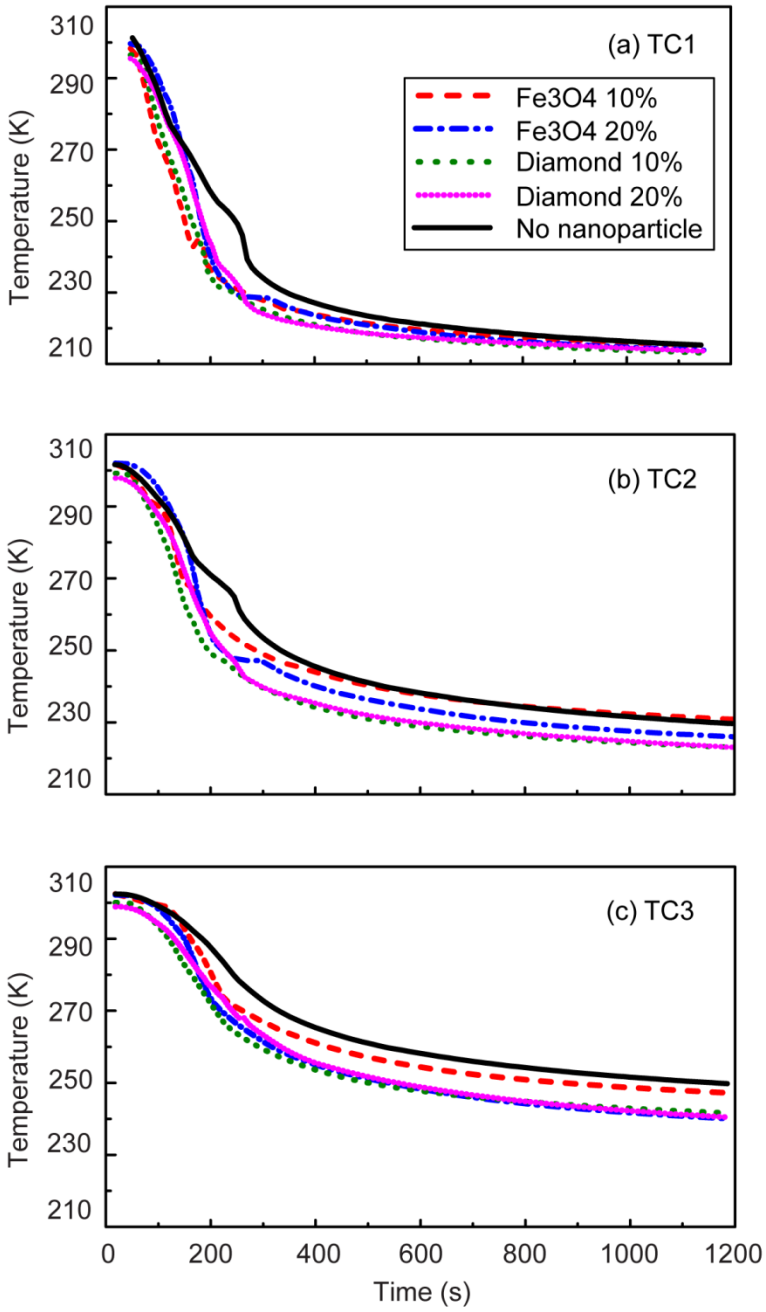

Figure 15 The temperature response measured by thermocouples for agarose experiments with injected nanoparticles for (a) TC1, (b) TC2 and (c) TC3. The flow rate is 80 ml/min and the diameter of blood vessel is 4.5 mm. 10 % and 20 % are the concentration of the nanoparticles in the nanofluid.

4.4 Summary

In this chapter, the influence of large blood vessels, the blood vessel diameter, the blood flow rate and the injected nanoparticles are analyzed via various experiments. Results demonstrated that all these parameters will significantly impact the freezing process. The large vessel diameter and the high flow rate will decrease the surgical efficiency while the injected nanoparticles can improve the cryosurgery.

The experiments are also conducted to prove the assumptions of the numerical method and validate the proposed model. Detailed validation studies will be illustrated in the following chapters.

This page has been left blank intentionally.

Chapter 5

Validation of Model

This chapter presents our work on validating the finite difference numerical model of a biological liver tissue undergoing cryo-freezing using the immersed boundary method (IBM). The liver tissue is treated as a non-ideal material having temperature-dependent thermophysical properties. The influence of heating effect due to blood flow has been investigated by applying the boundary condition-enforced IBM. The validation study shows that the model can successfully predict the temperature distribution during cryo-freezing. Further results have indicated that the heat source term due to the blood flow in the vessel embedded in the bio-heat transfer equation significantly impacts the tissue temperature profiles and thermal gradient histories.

Chapter 5 Validation of Model

5.1 Mesh Independence Analysis

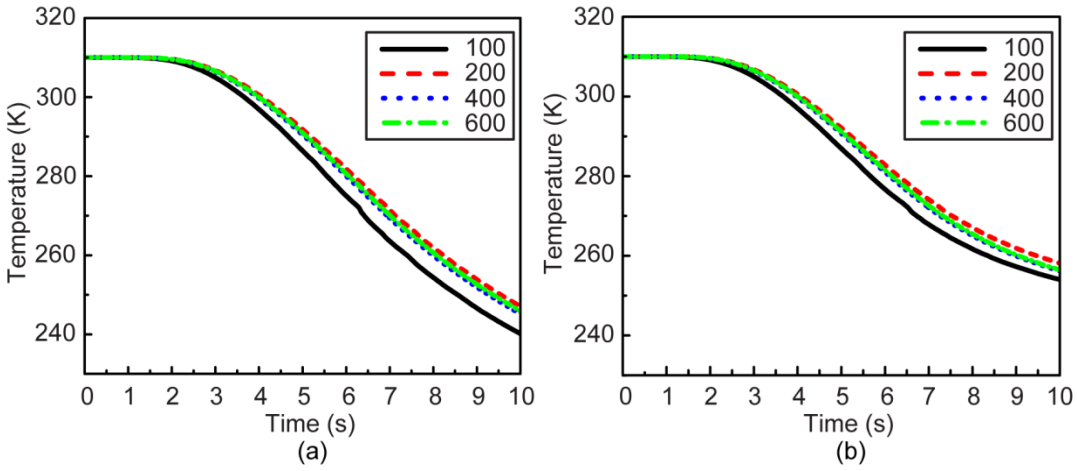

Figure 16 The temperature response during time with the increasing mesh size

To demonstrate the mesh independence of the numerical method, a simplified case study for different mesh sizes is carried out. Table 3 lists the different mesh sizes we chose for the mesh independence analysis. The computational domain is chosen as 20 mm × 20 mm and the blood vessel is located 5 mm away from the cryoprobe with the diameter of 1.0 mm. The results in Figure 16 show that the difference in temperature response becomes smaller with the increasing mesh size, especially when the mesh size is larger than 200 × 200.

More detailed information is shown in Table 3. T_x is the minimum temperature on the horizontal mid-plane of the right side, while T_y is the minimum temperature on the vertical mid-plane. After considering the balance among accuracy, computational time and computational storage, the mesh size is chosen as 400 × 400 for further analysis.

Table 3 Comparison of minimum temperature for different mesh sizes

Eulerian mesh size	100 × 100		200 × 200		400 × 400	600 × 600	800 × 800
No. of Lagrangian points	80	120	160	240	320	480	640
T_x (K)	133.12	133.40	122.67	122.72	107.36	108.41	108.68
T_y (K)	308.32	308.32	308.36	308.36	308.11	308.43	308.36

5.2 Different Bio-heat Models

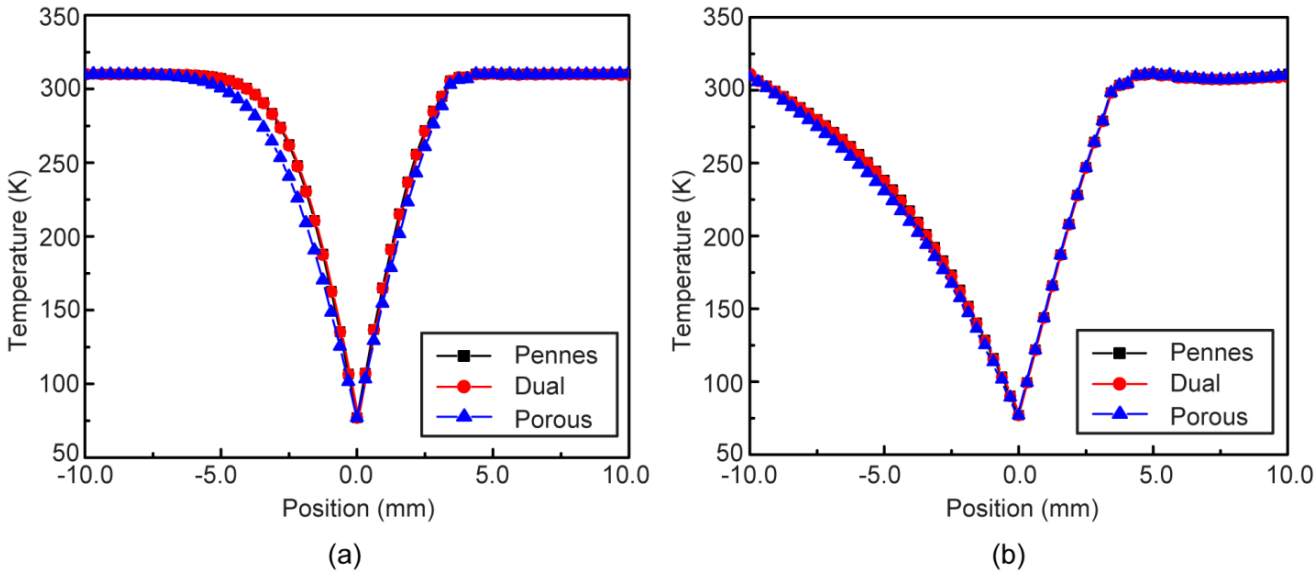

Figure 17 The temperature distributions of three models at (a) t=10 s and (b) t=100 s

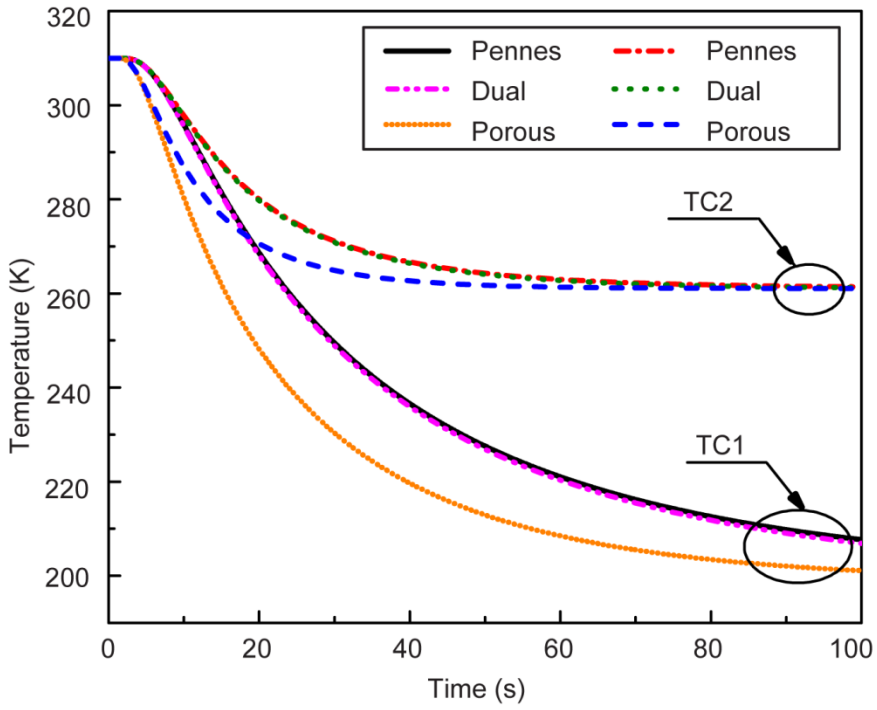

Figure 18 Temperature responses of three models at two selected thermocouples (shown as TC1 and TC2 in the figure)

Three different bio-heat models, Pennes model, dual-phase-lag model and the porous model, are selected to model the heat transfer in tissue. The governing equations and the boundary conditions are introduced in Chapter 3. Simulated results generated from each bio-heat model are compared. Figure 17 and Figure 18 depict the temperature distribution for different time duration and the temperature response at two selected positions.

As shown in Figure 17 and Figure 18, the tissue temperature profiles obtained by the porous model, which considers the heat transfer effect in a porous medium, are relatively lower than the other two models. This can be attributed to the introduction of the porous parts (filled with blood), which will increase the thermal conductivity of the tissue, thus positively influencing the freezing process. However,

as time elapsed, the temperature difference reduces, which lead to the eventual development of smaller size ice balls as the other two models. Taking the sources related to computing time, data storage space and the computational accuracy into account, the classical Pennes bio-heat model is judiciously selected for the rest of our study.

5.3 Model Validation

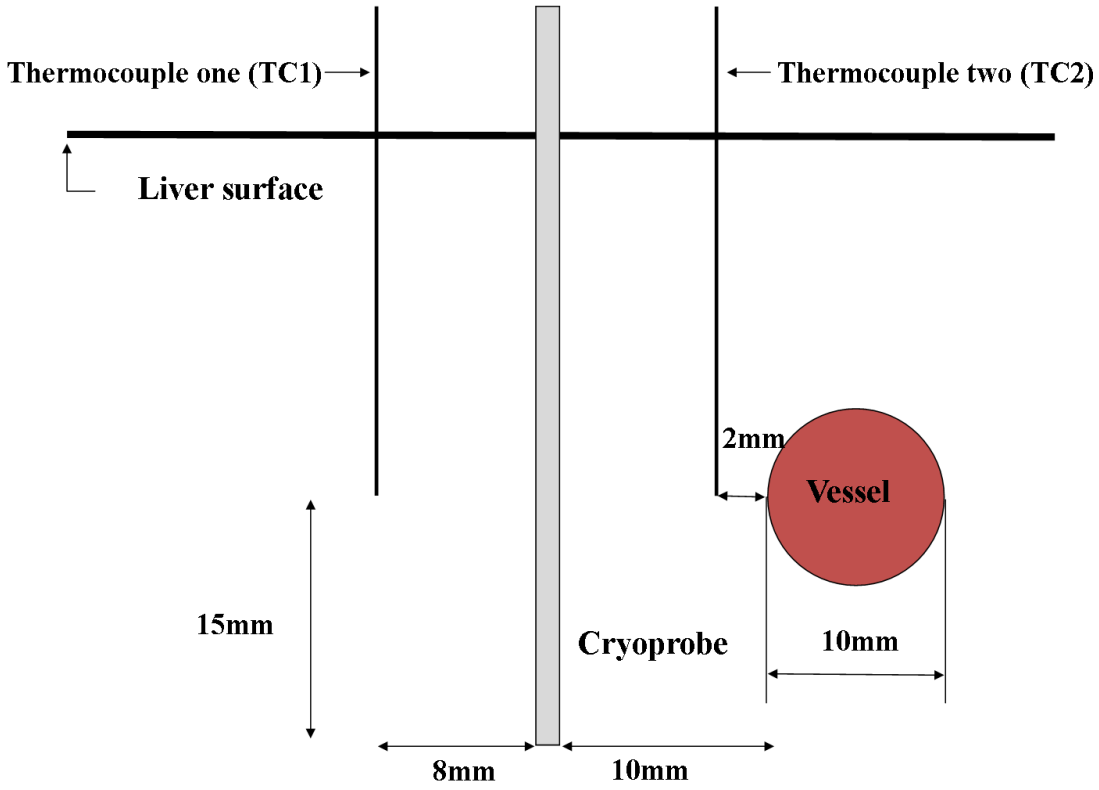

Figure 19 Schematic of the placement of a single cryoprobe with a circular blood vessel and two inserted thermocouples.

In this section, the application of the boundary condition-enforced IBM to the bio-heat transfer problem for studying tissue cryo-freezing will be validated by comparing the model with both experimental and numerical results. These results are

taken from an earlier published article by Kim *et al*. [6]. In this study, the blood perfusion term will be neglected for in vitro simulations but included for subsequent in vivo simulations.

Based on the in vitro cryosurgical experiments conducted by Kim *et al*. [6], a 2D rectangular geometry with dimensions of 80 mm × 70 mm is selected as the computational domain for this study. The cryoprobe is represented as an elongated cube which is 30 mm long and 3.4 mm in diameter. Temperature is measured at a location 2 mm away from the vessel wall. The distance between the cryoprobe and the blood vessel wall is 10 mm and the blood vessel diameter is 10 mm. Two thermocouples, used to measure real-time tissue temperatures, are strategically placed 8mm away from the cryoprobe. They are abbreviated as TC1 and TC2 in Figure 19. Based on vivo experiments conducted, the computed standard deviations involved in calculating the final temperatures spanned 1.5 K to 2.1 K [6]. A schematic illustrating the experimental details is shown in Figure 19. Boundary conditions are installed as thermal insulation on all surfaces except the one adjacent to the body core which is prescribed as 310 K.

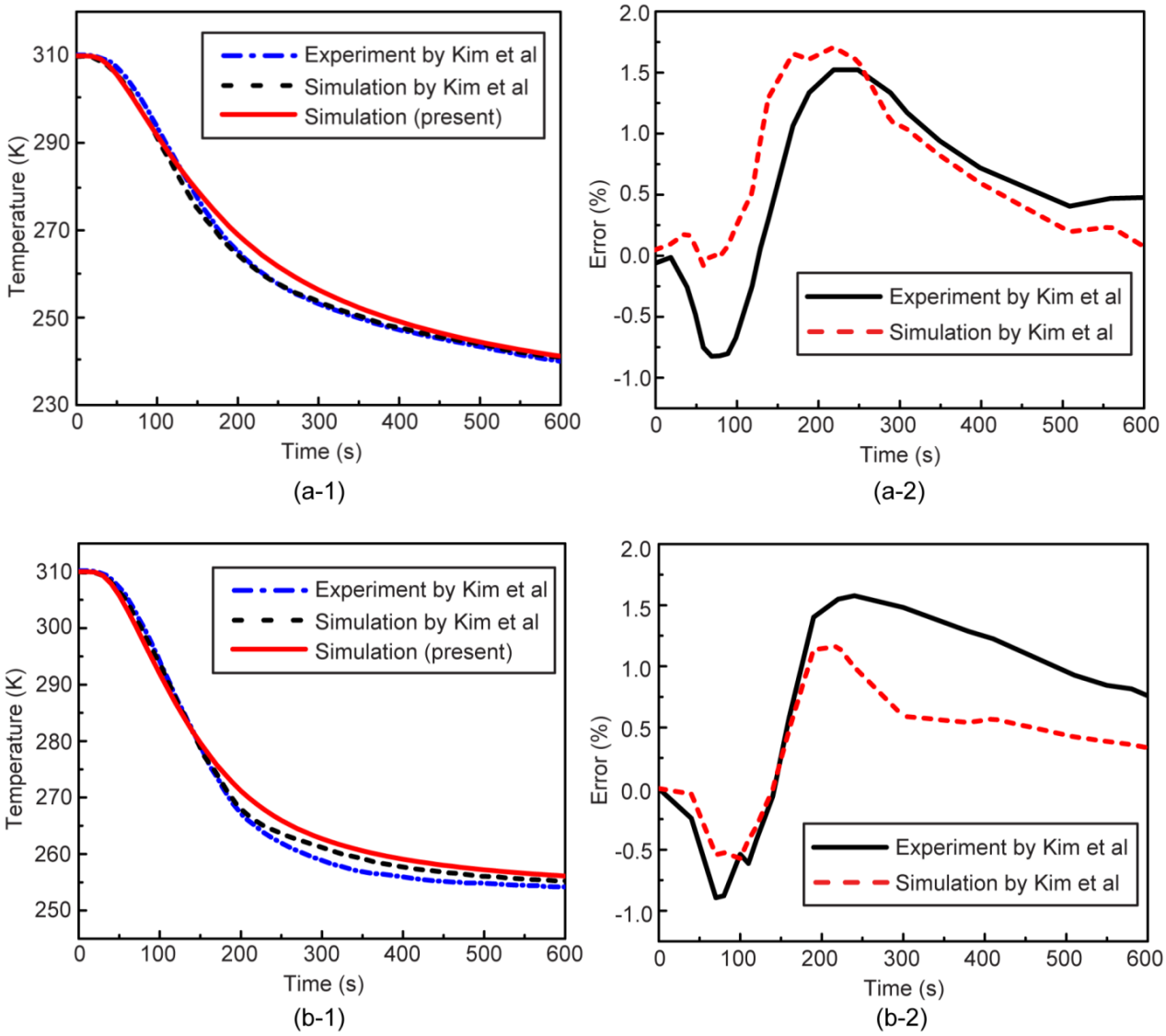

Figure 20 Comparison between numerical and experimental temperature response (a-1) is the temperature response at TC1 and (a-2) is the relative error; (b-1) is the temperature response at TC2 and (b-2) is the relative error.

Figure 20 compares simulation results and experimental average temperature data measured by the two thermocouples. For TC1 at the end of 10 min cryo-freezing, the difference is 0.2 K while the maximum difference in temperature is obtained to be 1.9 K over the entire freezing time. At the end of 10 min cryo-freezing, TC2 registers a temperature difference of 2.0 K while the maximum difference in temperature is observed to be 2.4 K over the entire freezing duration. As we would

have expected, the additional heat from the blood vessel markedly influenced the ice-ball progression and formation.

As can be seen, the temperature response is in great agreement with the data from Kim *et al.* [6]. Computed maximum percentage deviations for TC1 are 1.5 % and 1.7 % for experiments and simulations, respectively. For TC2, the computed percentage deviations are 1.5 % and 1.2 % for experiments and simulations, respectively. This can be explained by the understanding that the heat source brought by large blood vessels will highly affect the temperature distribution near the vessel wall.

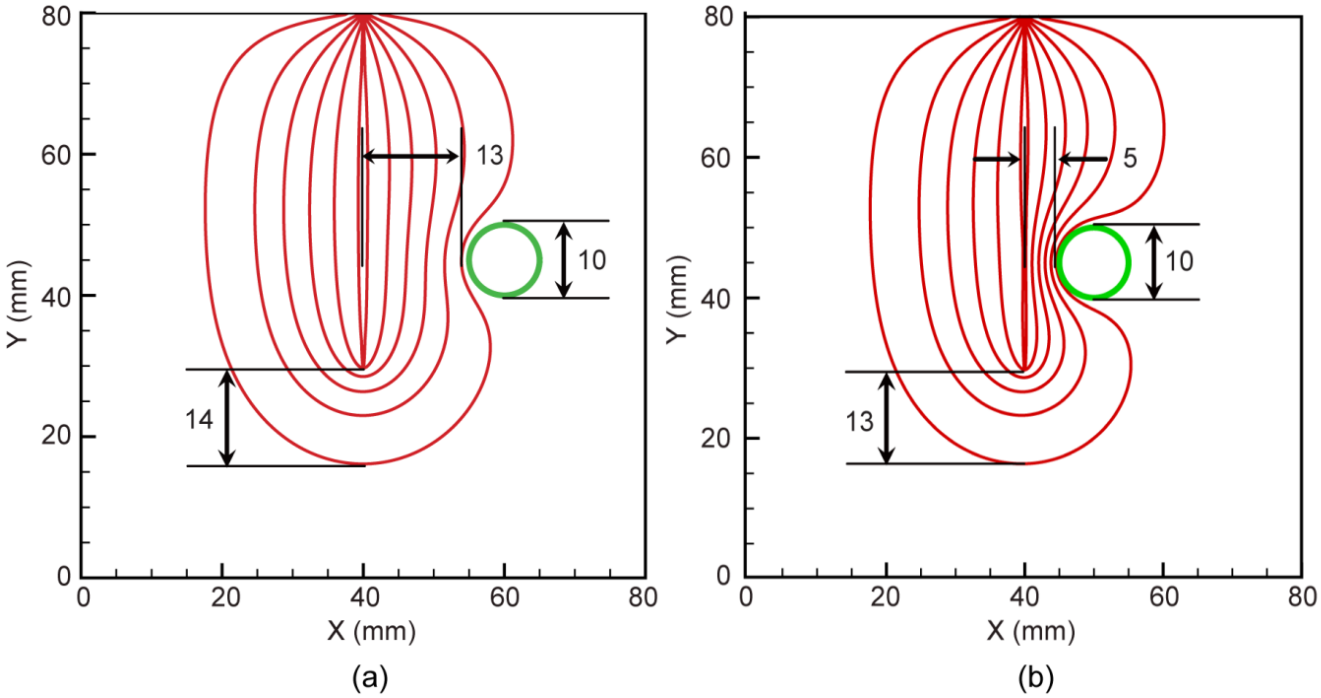

Figure 21 Ice-ball from the simulation after 10 mins freezing (a) the distance between cryoprobe and the blood vessel center is 20 mm and (b) the distance is 5 mm.

To better understand the influence of blood vessels, isothermal graphs of ice-ball formation after freezing for 10 mins are presented. Figure 21 shows the specific data. The distance between the cryoprobe and the vessel wall is 20 mm and 10 mm,

respectively. The freezing fronts of 0 ^{o}C in Figure 21 show that with the increasing of distance, the influence of blood vessel decreases, especially in the x-direction.

It is apparent that the cryoprobe extracts much more heat from the tissue in its radial direction rather than in its axial direction. The other side of the freezing tissue is not affected by the presence of a large blood vessel. If the cryoprobe is installed at a large distance away from the blood vessel and excessive coldness at extreme probe temperature is applied to ablate the target tissue, it is possible that a substantial amount of good tissue on the other side of the probe without the presence of any blood vessels will be over-freezed and sacrificed.

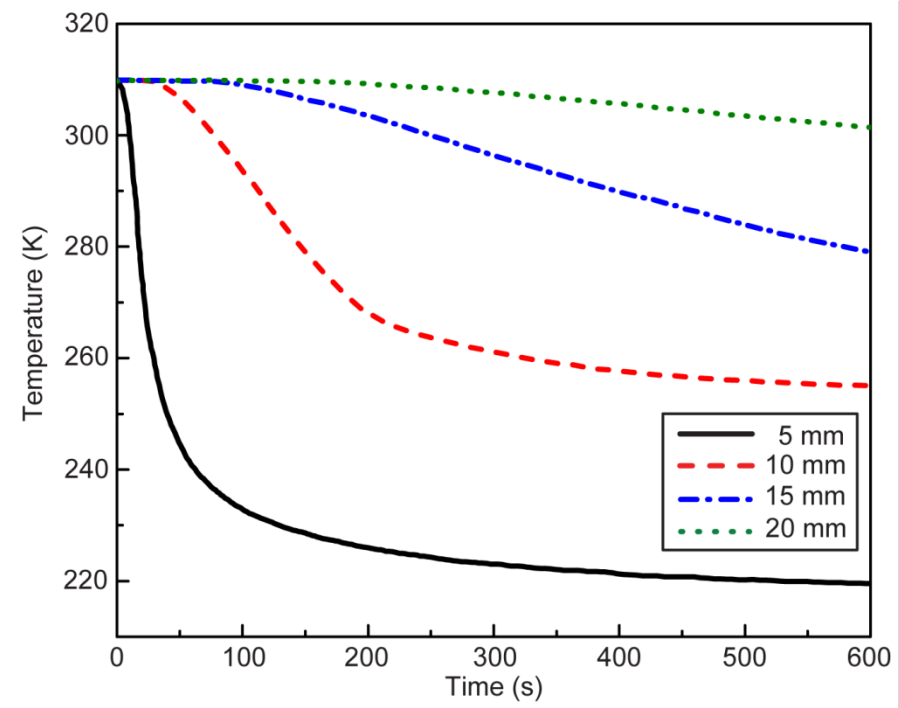

Figure 22 Temperature response for 4 different configurations. The distances between the cryoprobe and the blood vessel wall are set as 5 mm, 10 mm, 15 mm and 20 mm.

Trying to determine the optimal distance to place the cryoprobe from a major blood vessel to achieve best cryo-freezing outcome via a trail-and-error approach can

be a daunting task. In this section, we varied the distance between the cryoprobe and the vessel wall from 5 mm to 20 mm by 5 mm intervals in order to determine the optimal distance between the probe and the blood vessel to yield the best cryo-freezing of the target tissue near the blood vessel.

Figure 22 depicts the simulation results for four varying distances between the cryoprobe and the blood vessel. When the distance between cryoprobe and vessel wall is 15 mm, the tissue temperature is unable to attain even a phase-change temperature of 0 ^{o}C (273.15 K) towards the end of the process time at 600 s. Evidently, the maximum distance between the cryoprobe and the vessel wall has to be smaller than 15 mm. Tumors are known to be more resistive to freezing than normal tissue often possess highly vascularized structures. For this specific case study, it is, therefore, recommended that the distance between the probe and the blood vessel be close to 10 mm in order to realize effective tissue cryoablation.

Successful cryosurgery means maximizing destruction of cancerous cells while minimizing cryoinjury to the surrounding healthy tissue. A 'critical isothermal protocol', which assumes that complete necrosis occurs only in regions defined by a certain isothermal surface, is often regarded as a standard clinical procedure [44]. Although there is no definitive temperature reported where complete coagulation necrosis manifests as the critical temperature is tissue dependent, the -40 ℃ isotherm is often considered as the "lethal" temperature to most tumor cells [135]. The freezing front position is therefore essential information to determine if cancerous cells have been completely destroyed. To maximize the tumor destruction, the ice

ball diameter is typically extended 10 mm beyond the tumor edge, mimicked the surgical margins used in conventional tumor resection [136].

As a result, the freezing fronts, namely 0 ^{o}C and -40 ^{o}C, of the four configurations are also recorded in Figure 23 and Figure 24. The ice front (0 ^{o}C) at 300 s and 500 s near the blood vessel wall are shown in Figure 23 while the lethal front (-40 ^{o}C) at 500 s and 1000 s are shown in Figure 24. The lethal front is the isotherm of -40 ^{o}C, below which, the low temperature can cause nearly 100% lethal injuries to the tumor cells, while the ice front is the isotherm of 0 ^{o}C with which temperature the phase change will occur.

The degree and extent of the inflicted freezing damage on the targeted tissue very much depends on the spatial distance between the two critical freezing fronts (0 ^{o}C and -40 ^{o}C). Consequently, though the ice ball grows with increasing of distance between the cryoprobe and the blood vessel, the freezing efficacy depreciates instead. Comparing the graphs shown in Figure 23, the asymptotic points (marked as circles in figures) for the freezing front curves illustrate that the time remaining static of the ice front (0 ^{o}C) is earlier than that of the lethal front (-40 ^{o}C). Expectedly, the lethal front (-40 ^{o}C) stops progressing at distance nearer to the probe when compared to the ice front (0 ^{o}C).

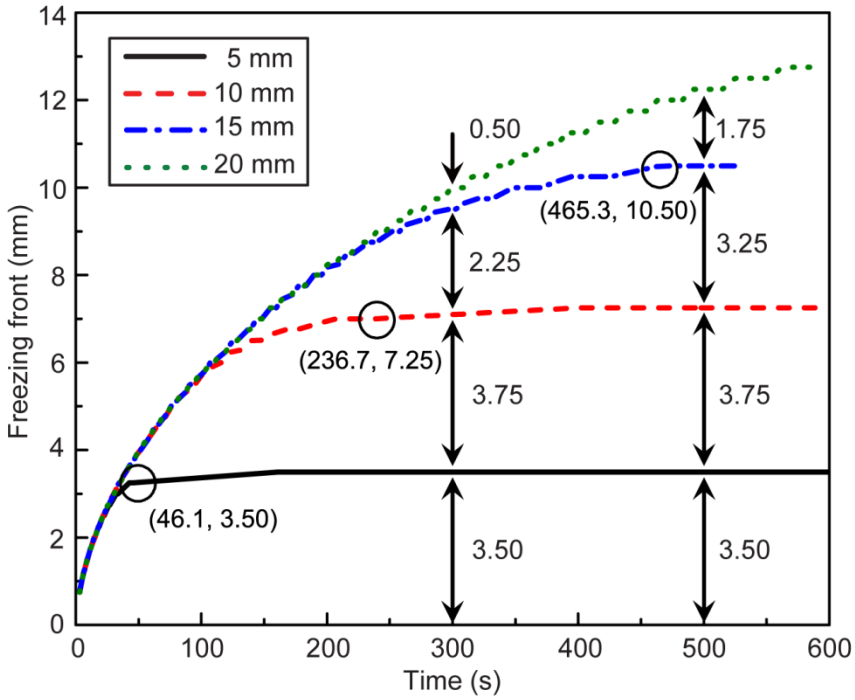

Figure 23 The freezing front for 0 ºC.

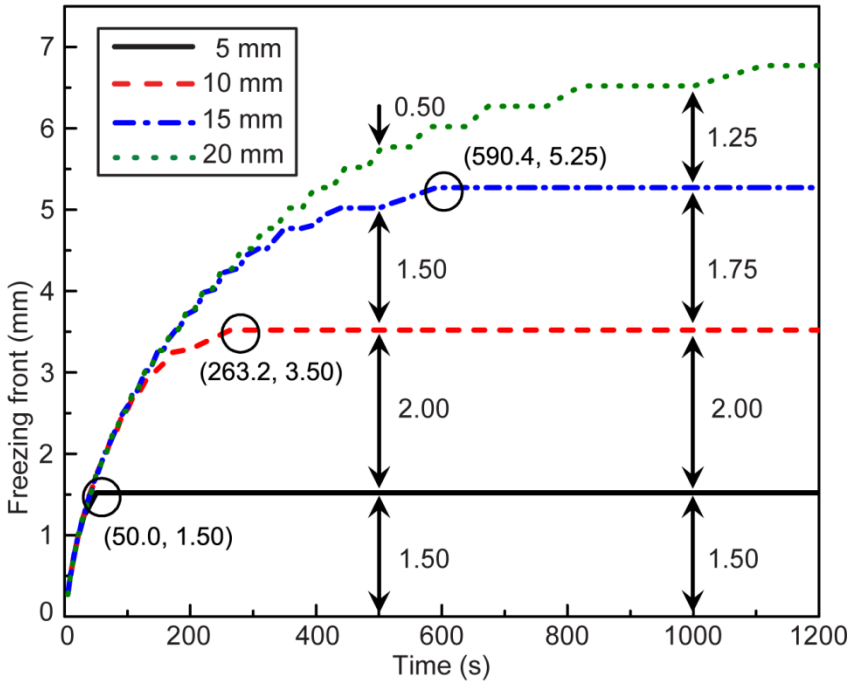

Figure 24 The freezing front for -40 ºC.

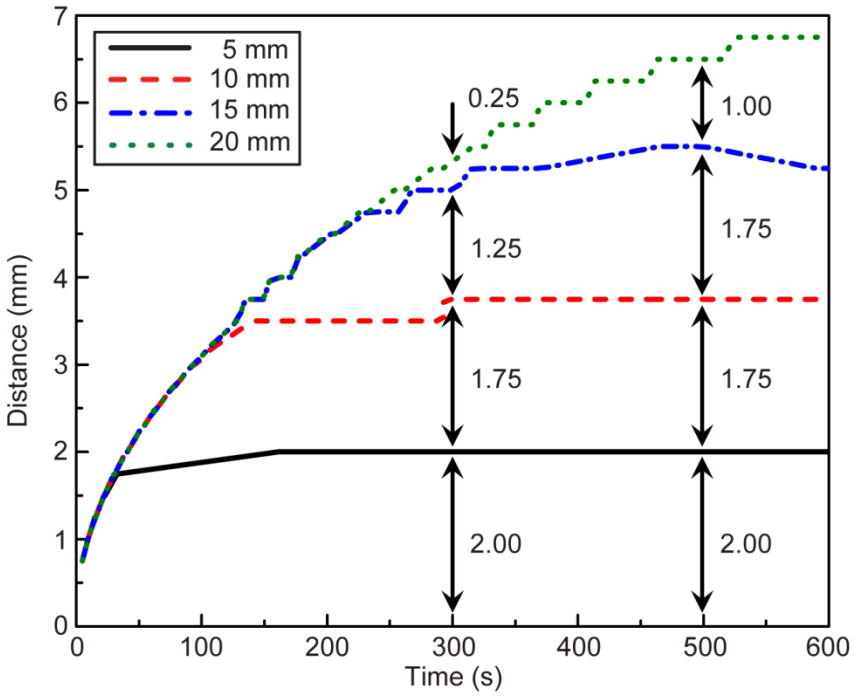

Figure 25 The spatial distance between the two ice-fronts (0 ºC and -40 ºC)

Figure 25 illustrates clearly the propagation of the gap between the lethal front (-40 ºC) and ice front (0 ºC) with time. When the freezing starts in the tissue, the ice front (0 ºC), owing to a higher velocity than the lethal front, moves at a faster rate and reaches a certain distance. As time progresses, these fronts have nearly the same velocity. Later on, at the end of the ablation period, the lethal front (-40 ºC) moves faster than the ice front (0 ºC). The degree and extent of the inflicted freezing damage on the targeted tissue very much depend on the spatial distance between the two critical freezing fronts (0 ºC and -40 ºC). Simulated results clearly show that the differences in freezing front spacing are 2.00 mm, 3.75 mm, 5.50 mm and 6.50 mm for the respective distances between cryoprobe and blood vessel of 5 mm, 10 mm, 15 mm and 20 mm after freezing for 500 s.

5.4 Summary

The study in this chapter explores the homogeneous finite difference modelling with large blood vessels for clinical cryosurgery application. A combination model of the Pennes bio-heat transfer model and the boundary condition-enforced immersed boundary method is validated, by comparing with the numerical results and the in-vitro experiments for pork liver from literature.

The temperature response predicted by the model is in great agreement with the previous study after freezing for 600 s. The maximum error of the validation is 1.7 % and 1.5 % for different thermocouple locations, respectively. The comparison between the numerical results and the experimental results shows that the model can be successfully applied to simulate the cryo-freezing process with one large blood vessel. This is the first successful attempt to combine the Pennes bio-heat transfer equation with IBM. Another important feature of the new model is that it can be generally applicable to many other bio-heat transfer applications where complex object modelling is required.

Chapter 6

Two Dimensional Analysis of Vascular Tissue Cryo-freezing

This chapter describes the numerical investigation on the effects of the blood vessel structure and injected nanoparticles during the cryo-freezing of a clinically-extracted vascular tissue. A hybrid two-dimensional finite difference analysis combined with immersed boundary method has been developed to accurately simulate the cryo-freezing process. Based on the measured experimental data, the numerical results agreed well with the experimental data. This improved cryo-freezing model is able to significantly simplify the mesh generation process at the boundary resulting in improved computational efficacy. For simulating the temperature profile of a tumor that is sited in a dominantly vascularized tissue, this model is able to capture with ease the thermal effect at junctions of the blood vessels.

Chapter 6 Two Dimensional Analysis of Vascular Tissue Cryo-freezing

6.1 Experimental Validation

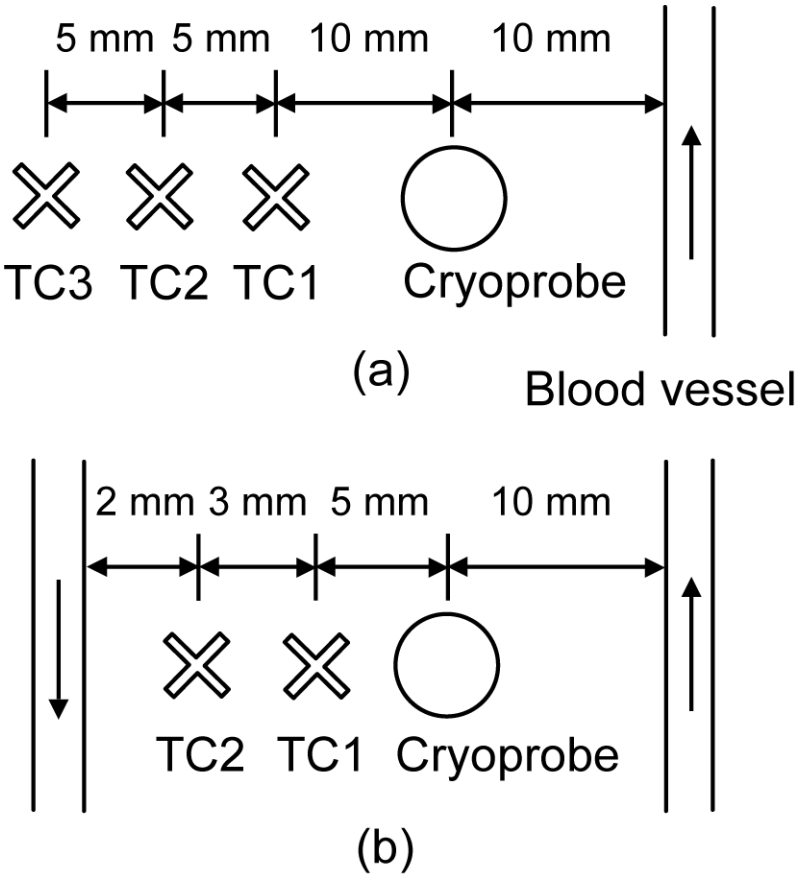

Figure 26 The layout of thermocouples, blood vessels and cryoprobe for (a) a single blood vessel and (b) a parallel counter-current vessel pair

Following the experimental procedure in Chapter 4, we analyze the experimental results by considering two situations with one large blood vessel and a parallel counter-current vessel pair. The layout of thermocouples, blood vessels and cryoprobe is shown in Figure 26. The temperature distribution and temperature response after freezing for 20 min are measured at different thermocouples.

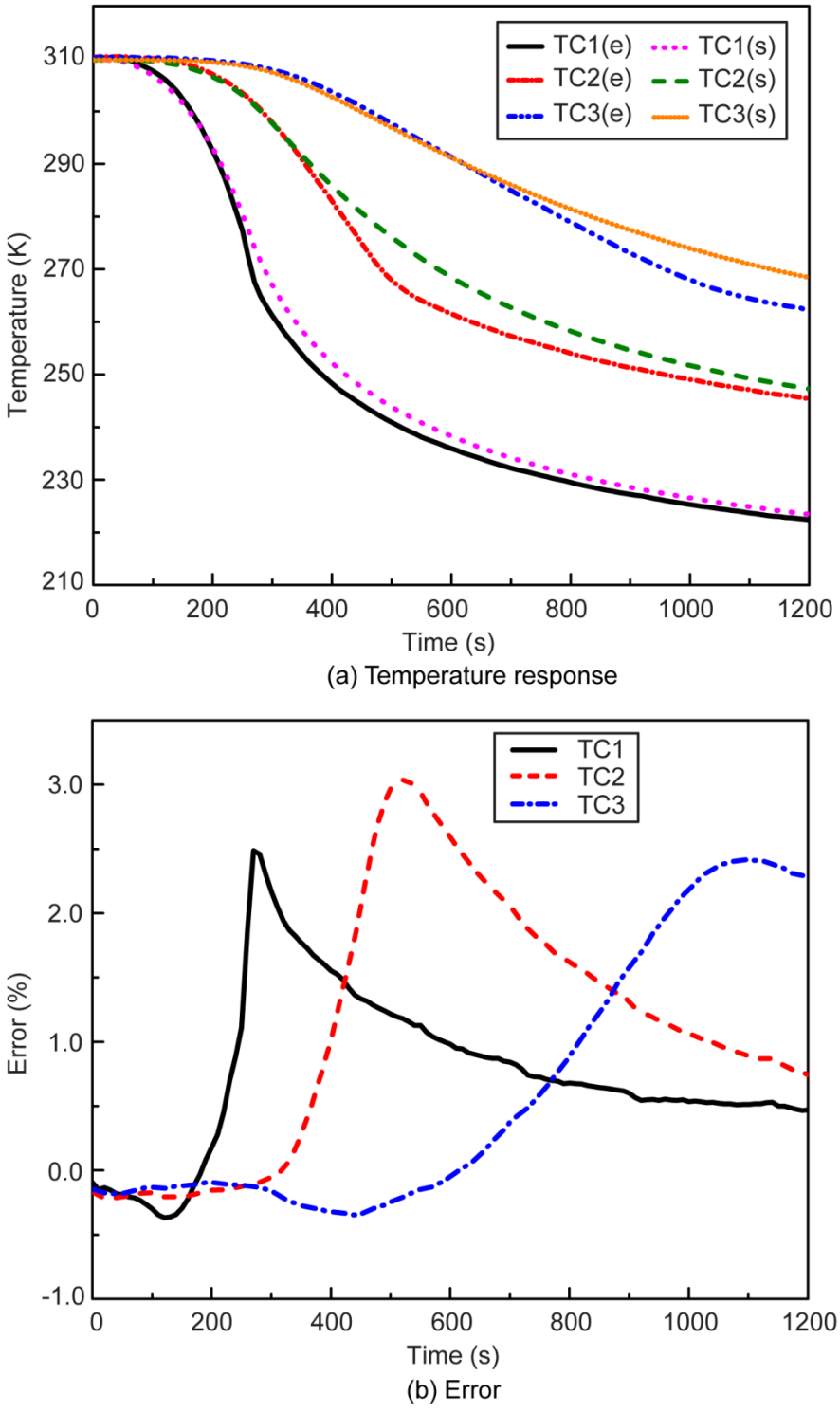

Figure 27 The numerical comparison of (a) temperature response and (b) error for a single blood vessel case at three specific locations. The blood vessel diameter is 4.5 mm and the flow rate is 80ml/min. (e stands for experiment and s stands for simulation)

Figure 27(a) shows the temperature response changing with time for three thermocouples while Figure 27(b) displays the relative errors between experimental and numerical results. Three thermocouples, marked as TC1, TC2 and TC3, are used to measure the transient temperature at 10-second intervals. It is apparent from Figure 27 that the agreement between experimental and numerical results is satisfactory in general, and the maximum relative errors for TC1, TC2, and TC3 are 2.49 %, 3.04 % and 2.42 %, respectively (shown in Figure 27(b)). Therefore, the conclusion can be preliminarily obtained that the immersed boundary model is appropriate to analyze freezing process with the complicated vessel network within small relative errors, at least for the one single blood vessel case in this study.

Figure 26(b) presents the schematic diagram of the case with a parallel counter-current vessel pair. This model is compared with one having two branches' blood vessel network. The numerical prediction of the temperature response is plotted against the two vessels model at two selected positions.

A comparison between the temperature responses for the two vessels model and the simulated results is shown in Figure 28. The maximum discrepancies for these two positions TC1 and TC2 are 12.9 % and 5.6 %, respectively. It is apparent that the discrepancy for the thermocouple point closer to the cryoprobe is relatively higher than the other one. It is attributed to the fact that the temperature at TC1 can potentially be affected by the ability of the cryoprobe to sustain a constant surface temperature.

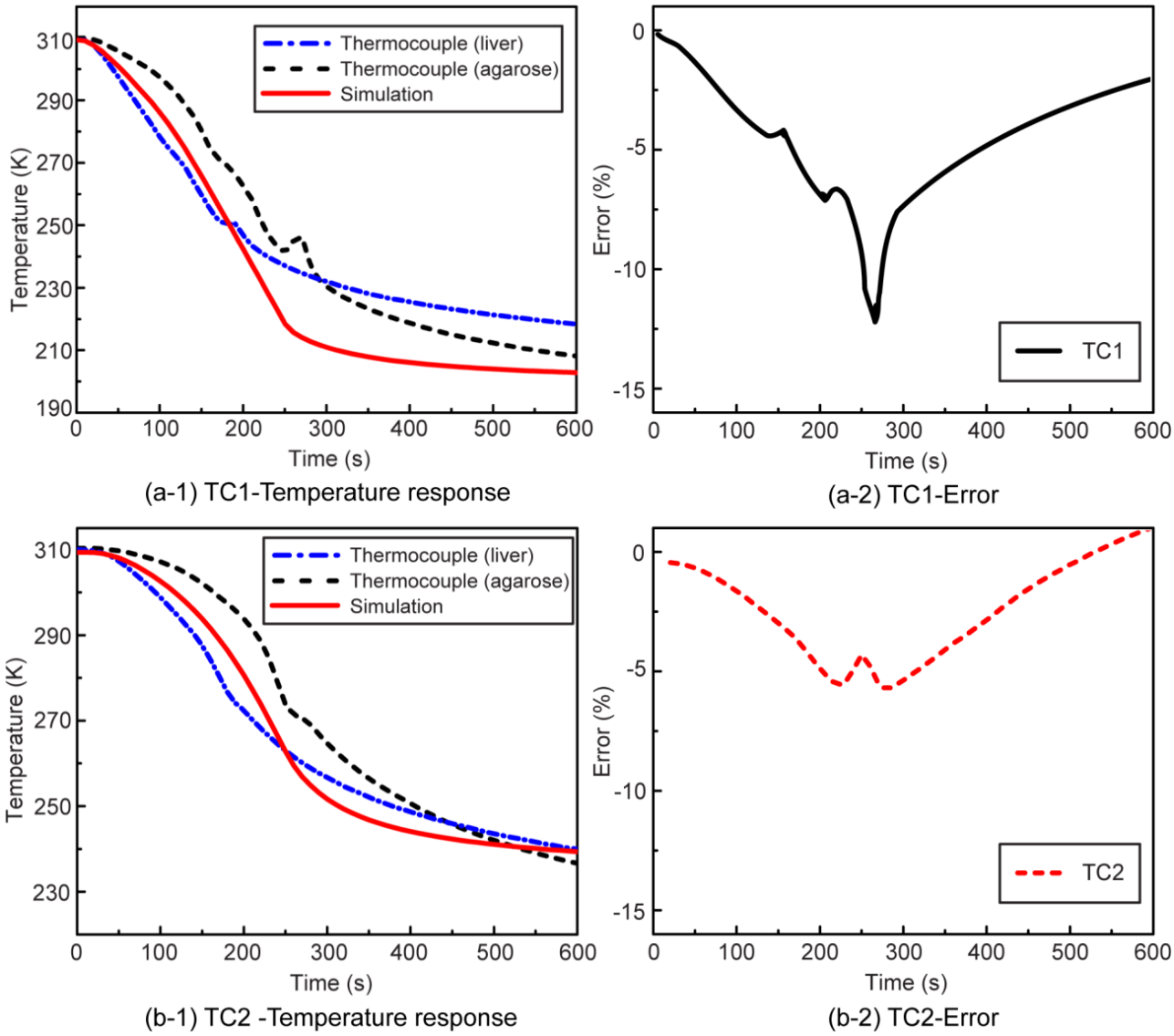

Figure 28 The numerical comparison of temperature response for a parallel counter-current vessel pair case at two specific locations. The blood vessel diameter is 2.0 mm and the flow rate is 80ml/min.

The preceding discussion demonstrated, for the first time, the use of the new method to represent complicated blood vessel network with reasonable accuracy.

6.2 Vessel Complexity and Ice-ball Irregularity

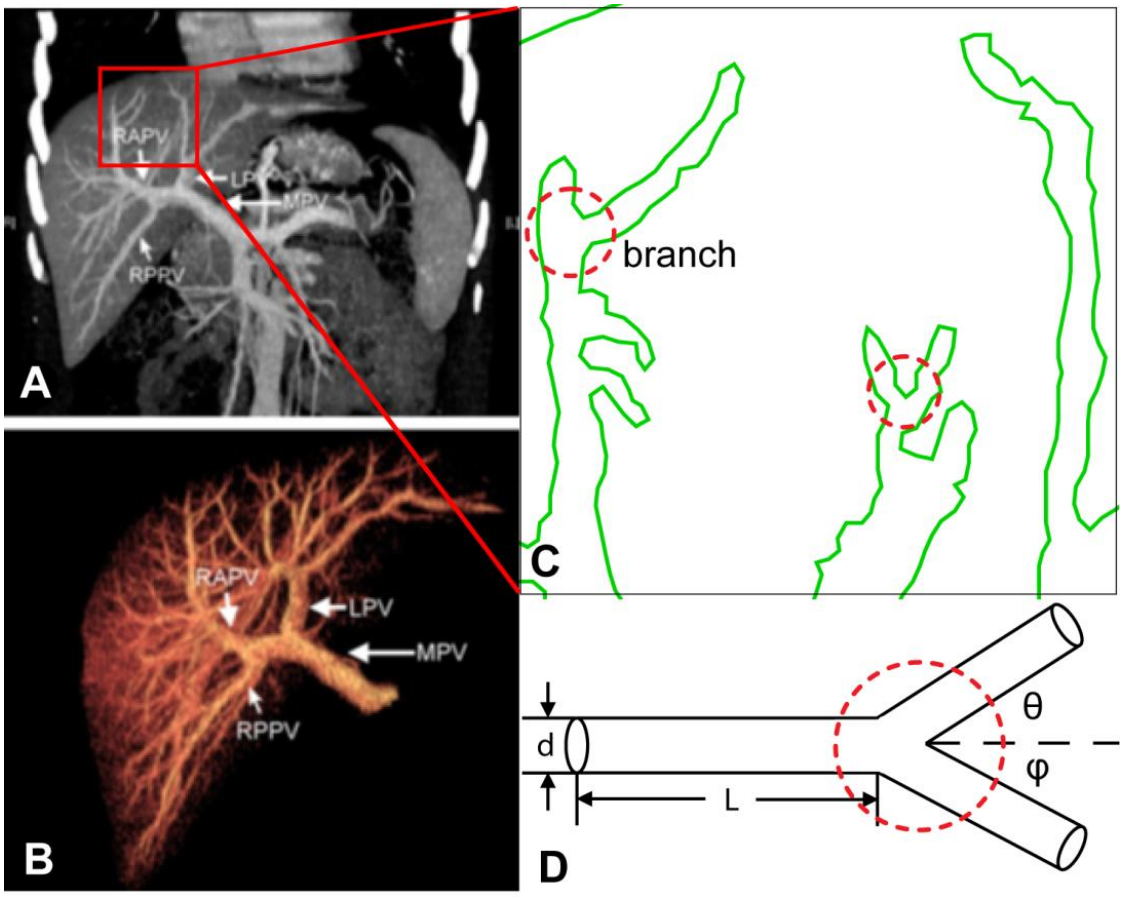

Figure 29 The blood vessel structure of a 31-year-old male potential liver donor with a type 1 main portal vein. [137]

The blood vessel complexity is an important parameter that describes the environment around the tumor. To better qualify the environmental complexity near the tumor, we introduce a new parameter β, which defines the complexity of the blood vessel. From Figure 29, it is apparent that by just considering the selected freezing area, each branch of the blood vessels can be easily described using d_n, l_n, d_{n+1}, l_{n+1}, θ and φ. By analyzing the freezing area, we can obtain the complexity of the blood vessel as follows,

$$\beta = \frac{P}{P_{total}} \times N \times \sum_{n=1}^{N} \frac{d_n}{l_n} \tag{35}$$

where P is the perimeter of the selected blood vessel, N is the number of the branches, l_n is the length of the n^{th} branch and d_n is the diameter of the n^{th} branch.

The definition of the irregularity of the ice ball shape is from our previous work with Zhao [150]. To identify the degree of irregularity, a shape factor known as "iceball irregularity" is introduced. The term here characterizes the dynamics of rigid bodies and is capable of evaluating the overall shape of profiles.

For the analysis of the physical vascular system in human body, the blood vessel of a 31-year-old male potential liver donor with a type 1 main portal vein is chosen for the next study. The structure of the vessel is shown in Figure 29.

Five different locations on the liver tumor are chosen for this study. Figure 31 shows the thermal isotherms after freezing for 100 s. The coordinates of the cryoprobes are (0.045, 0.13), (0.10, 0.19), (0.14, 0.20), (0.05, 0.09) and (0.19, 0.18), respectively. Following the computational method in Eq. (35), the ice ball shape irregularity change with the increasing the blood vessel complexity is shown in Figure 30. It is apparent that with the increasing of blood vessel complexity, the ice ball becomes more and more irregular. That is because the thermal effects brought by the large blood vessel will impact the temperature change of the surrounding tumor, thus affecting the shape of the growing ice ball.

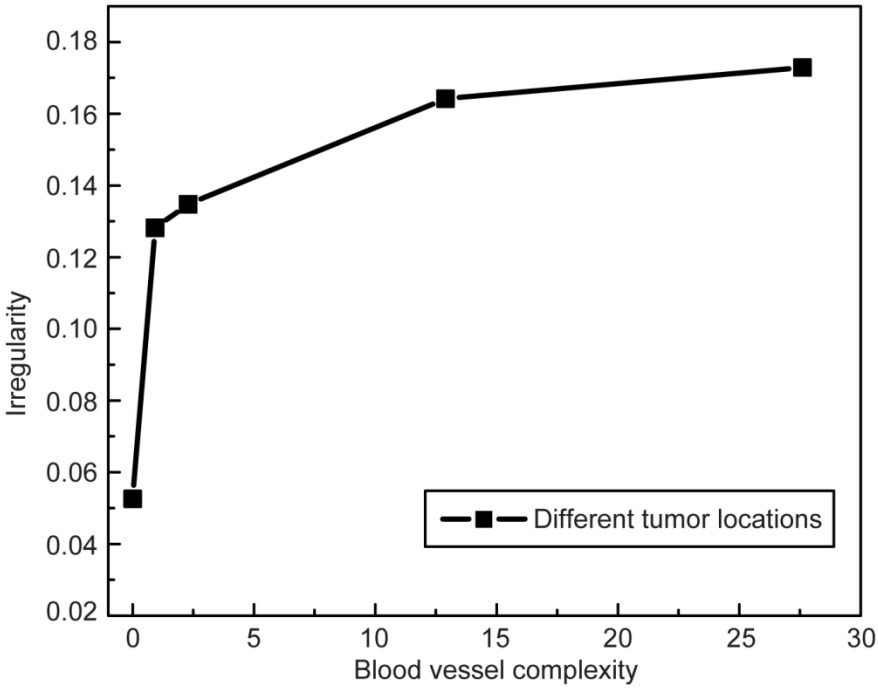

Figure 30 The changing of ice-ball shape irregularity with different blood vessel complexities.

To better understand the ice ball growing process with time, both the lethal front (-40 ^{o}C) and the ice front (0 ^{o}C) are measured for three selected tumor locations. The coordinates of the cryoprobes are (0.045, 0.13), (0.10, 0.19), and (0.14, 0.20). Figure 34 shows the simulation results by applying our proposed method.

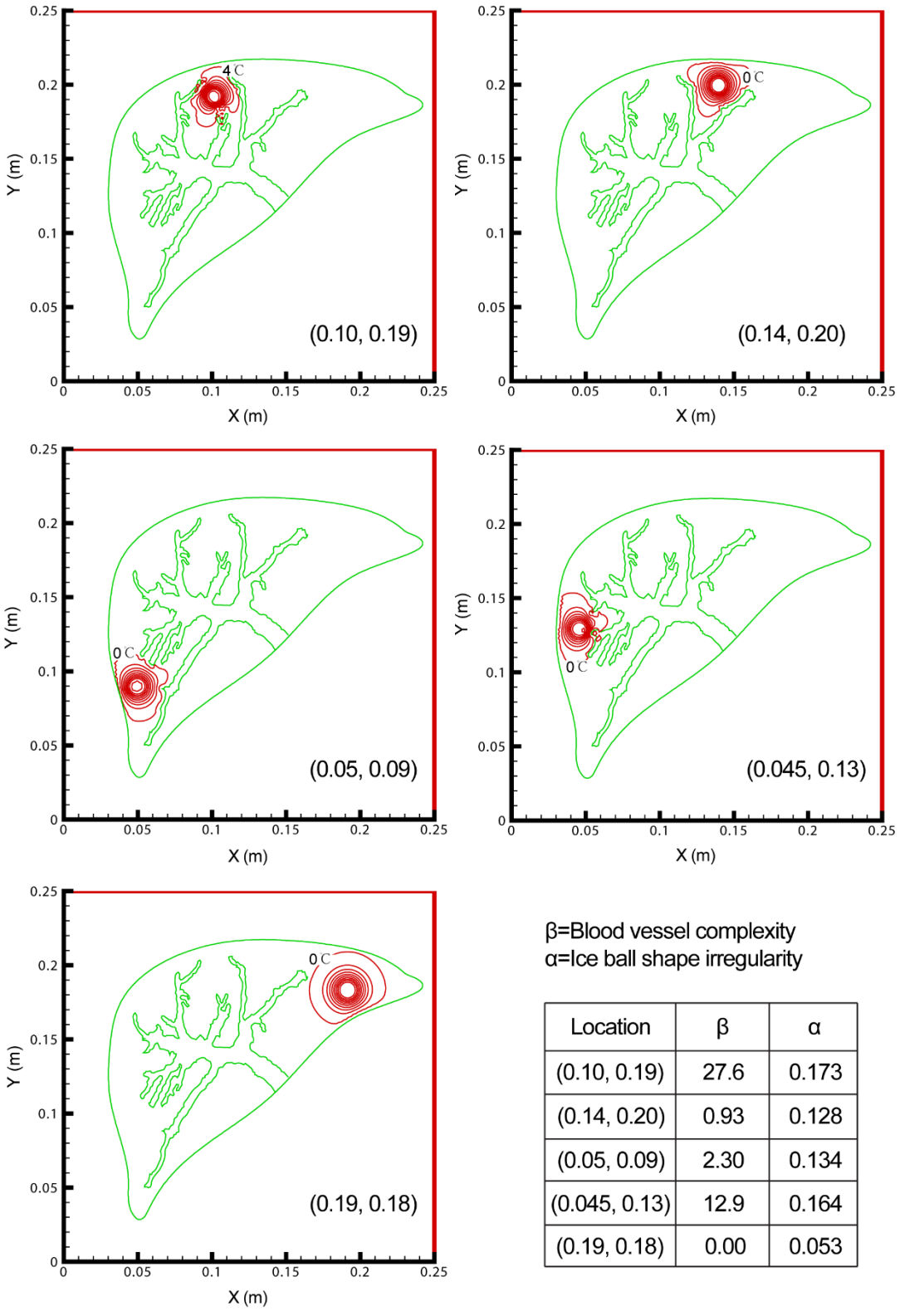

β=Blood vessel complexity
α=Ice ball shape irregularity

Location	β	α
(0.10, 0.19)	27.6	0.173
(0.14, 0.20)	0.93	0.128
(0.05, 0.09)	2.30	0.134
(0.045, 0.13)	12.9	0.164
(0.19, 0.18)	0.00	0.053

Figure 31 The temperature isotherms after freezing for 100 s.

6.3 The Nanoparticle Model

In this section, we develop a modified nanoparticle model, which was earlier proposed by Leong *et al.* [138] and Murshed *et al.* [139]. Compared with the conventional Hamilton-Crosser model [140], this model can better present the thermal conductivity with low nanoparticle concentration and small nanoparticle size when they are incorporated to the bio-tissue to promote freezing. That is because the modified model takes into account the effects of fluid molecules in the interface and the surface chemistry of the nanoparticles. The formulas of thermal conductivity, density and heat capacity are shown as,

$$k_f = k_t \frac{\delta\Phi(k_p - \delta k_t)[2\gamma_2^3 - \gamma_1^3 + 1] + (k_p + 2\delta k_t)\gamma_2^3[\Phi\gamma_1^3(\delta - 1) + 1]}{\gamma_2^3(k_p + 2\delta k_t) - (k_p - 2\delta k_t)\Phi(\gamma_2^3 + \gamma_1^3 - 1)} \tag{36}$$

$$\rho_f = (1-\Phi)\rho_t + \Phi\rho_p \tag{37}$$

$$c_f = (1-\Phi)c_t + \Phi c_p \tag{38}$$

$$\gamma_1 = 1 + 2(\bar{h}/d_p) \tag{39}$$

$$\gamma_2 = 1 + (\bar{h}/d_p) \tag{40}$$

where $\bar{h} = \sqrt{2\pi}\sigma$ is the interfacial layer thickness at the surface, Φ is the concentration of the nanofluid and δ is an empirical parameter depending upon the distribution of fluid molecules in the interface and the surface chemistry of nanoparticles.

Table 4 The physical parameters of different nanoparticles [141]

Nanoparticle	Thermal conductivity ($W\ m^{-1}K^{-1}$)	Heat capacity ($J\ kg^{-1}K^{-1}$)	Density ($kg\ m^{-3}$)
Au	297.7	2.21×10^3	19320
Al_2O_3	39.7	2.82×10^3	3970
Fe_3O_4	7.1	3.2×10^3	4800

For the three different property types of nanoparticles Au, Al_2O_3 and Fe_3O_4, the thermal conductivity and thermal capacity are shown in Table 4. By applying the Hamilton-Crosser model and the modified model proposed by Leong *et al.* [138] and Murshed *et al.* [139, 142], the effective thermal conductivities of nanoparticles can be obtained.

The respective effective thermal conductivity change from the two models with the increasing thermal conductivity levels of nanoparticle is shown in Figure 32. As the modified model considers the effects of distribution of fluid molecules in the interface and the surface chemistry of nanoparticles, it can better applied to the situation of low nanoparticle concentration and small nanoparticle size.

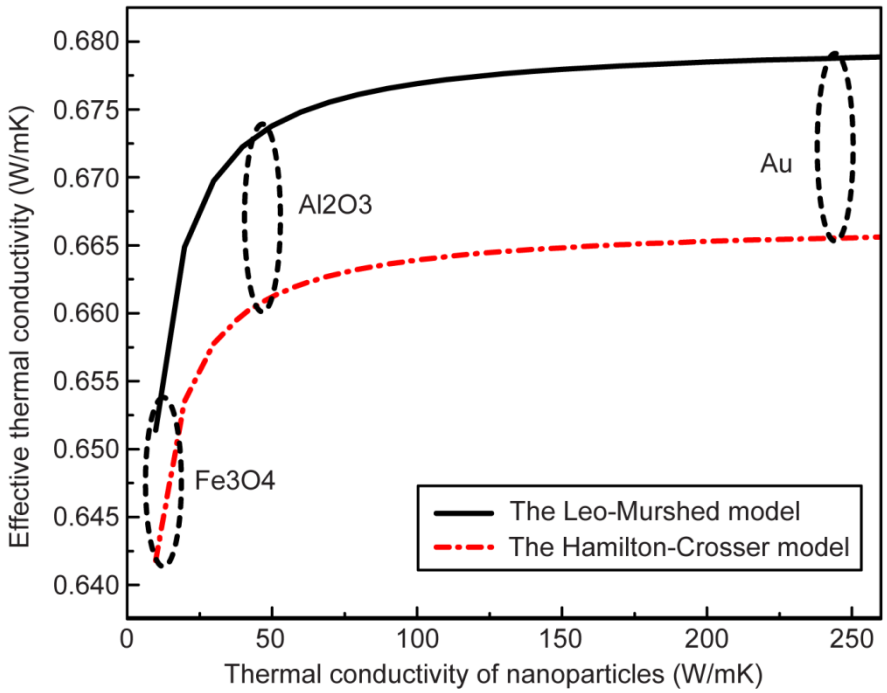

Figure 32 The change of effective thermal conductivity with the increasing thermal conductivity of nanoparticles, the nanoparticle size d_p =20 nm, δ =1.0 and the volume fraction Φ =0.1.

By applying different nanoparticle models, the calculated effective thermal conductivity can vary. Such approximate data may potentially lead to uncertainty in the numerical results to a certain extent. Nevertheless, it can be seen in Figure 32 that albeit the absolute value of the effective thermal conductivity being different between these two models, the relative value is almost the same. This leads to the results showing marginal temperature differences between these two models during cryo-freezing incorporating different nanoparticles. Moreover, the change in effective thermal conductivity is confined to a relatively small range, resulting in indiscernible differences when comparing models with and without nanoparticles.

Temperature distributions are measured after 20 mins of the cryo-freezing. It could be easily observed that while maintaining almost the same temperature for three nanoparticles at the temperature below -150 ^{o}C, utilization of nanoparticles can reduce the temperature significantly between the temperature of 0 ^{o}C and -150 ^{o}C. In addition, the injection of nanoparticles enhances the freezing speed during the period of cryo-freezing. For the physical problem, as the experiments in Chapter 4.3.4, the lowest temperature near the cryoprobe is about -85 ^{o}C, which is between 0 ^{o}C and -150 ^{o}C. These provide the evidence that utilization of nanoparticles can enhance the freezing rate, thus reducing the temperature significantly in the surgery process.

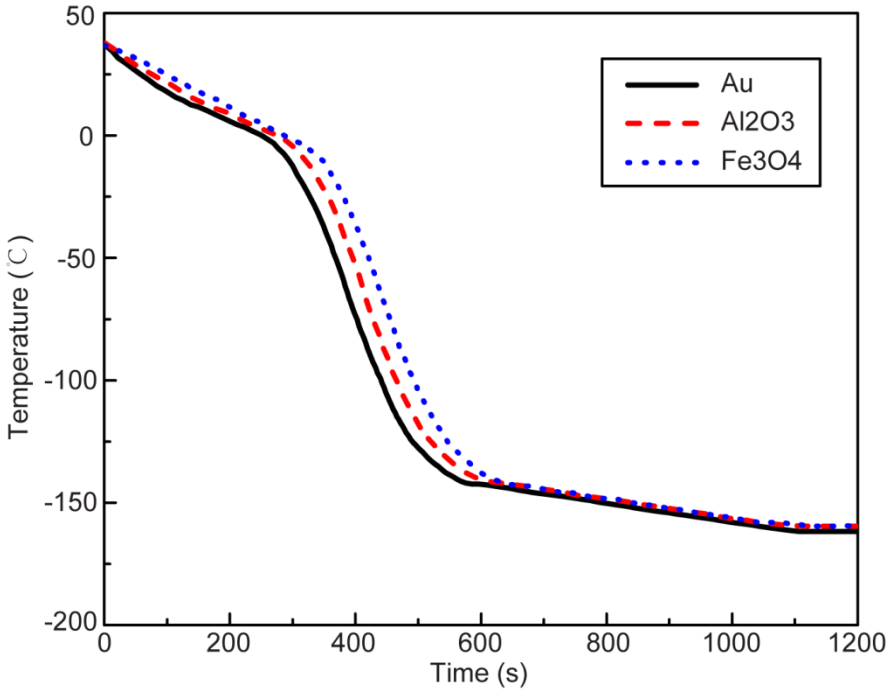

Figure 33 Temperature response at the center of tumor during 20 mins of cooling for different nanoparticles (Au, Al_2O3, Fe_3O_4), the nanoparticle size d_p =20 nm, δ =1.0 and the volume fraction Φ =0.1.

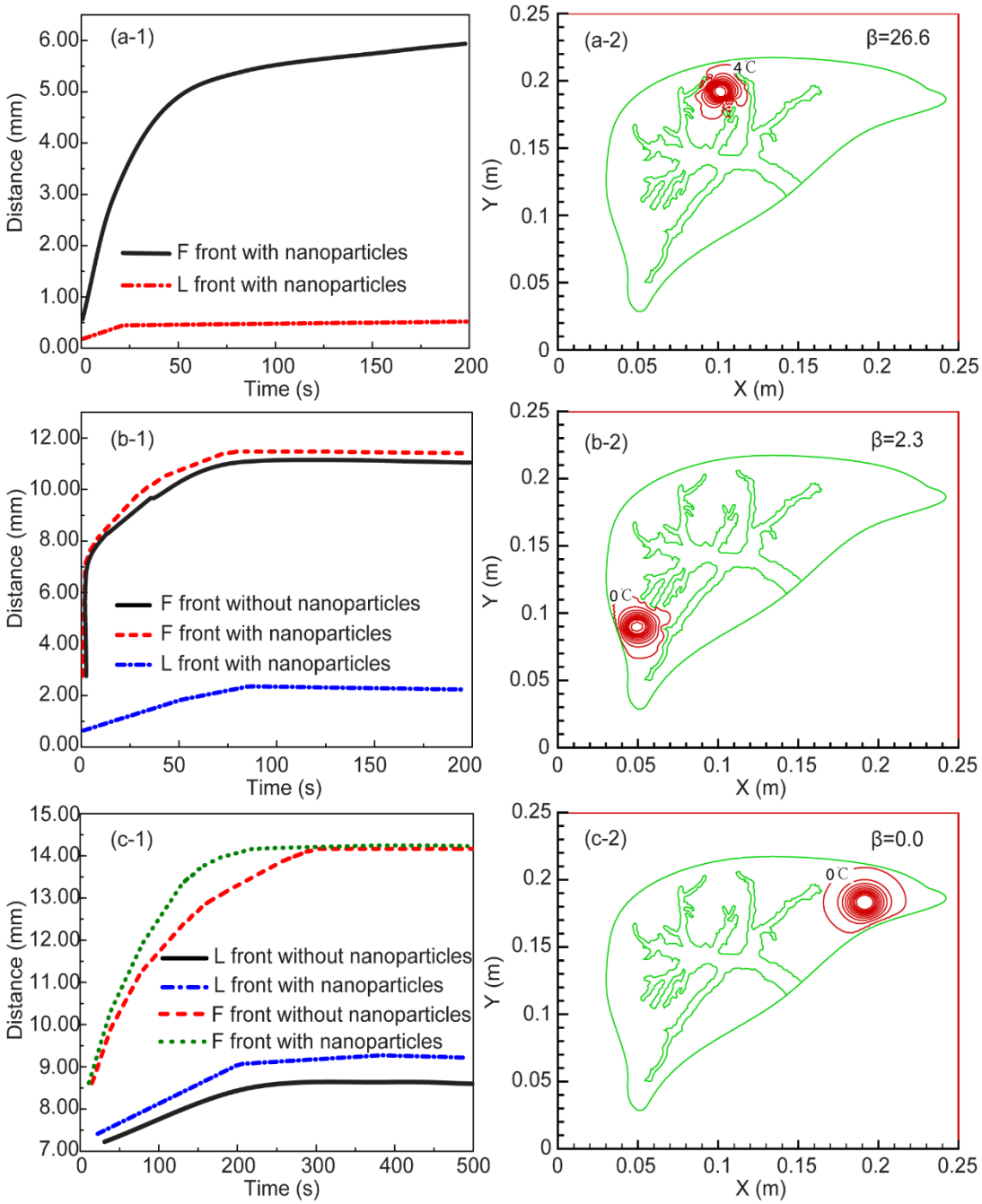

Figure 34 The lethal front and freezing front for locations of (a) (x=0.10, y=0.19), (b) (x=0.05, y=0.09), and (c) (x=0.19, y=0.18). (1) shows the freezing fronts during time from 0 s to 200 s and (2) shows the isotherm after freezing for 200 s. (F front stands for the freezing front and L front stands for the lethal front).

In the following example, we adopt Au nanoparticle for our case study. The thermal conductivity of Au nanoparticles k_p =297.7 W $m^{-1}K^{-1}$, and thermal

conductivity of tissue k_t =0.5 W $m^{-1}K^{-1}$. The nanoparticle size d_p =20 nm, δ =1.0 and the volume fraction Φ =0.1. We choose three locations for further analyzing the progress of both freezing front and lethal front. The freezing front and lethal front are measured along the X-direction. Figure 34 shows the ice front, the lethal front and the isotherm for different situations of blood vessel complexity

Results from Figure 34 show that, nanoparticles can significantly increase the freezing area as nanoparticles promote the effective thermal conductivity and the effective thermal capacity of the tissue. For the case with blood vessel complexity β =0, the freezing front grows from 14.1 mm to 14.2 mm; for the case with blood vessel complexity β =2.3, the freezing front increases from 11.1 mm to 11.4 mm; for the case with blood vessel complexity β =26.6, the freezing front increases from 0 mm to 0.6 mm.

Analyzing the results of the lethal fronts with and without nanoparticles, we reach the conclusion that the distance difference of the ice fronts between the case with and without nanoparticles increases with the increasing blood vessel complexity. That is because the blood vessel tree with a more complex structure will bring larger heat flux. This will cause a relatively higher surrounding temperature compared with the situation with lower vessel complexity. According to the results presented in Figure 33, nanoparticles reduce the temperature more significantly between the temperature of 0 ^oC and -150 ^oC than the temperature below -150 ^oC. As a result, the nanoparticles can more effectively enlarge the lethal damage area with the case of a larger blood vessel complexity.

6.4 Summary

By integrating a 2D finite difference model with the IBM, this chapter investigates the effects of parameters on the mechanisms underlying the cryo-freezing of a liver tumor. The model includes an accurately designed platform with complex blood vessel network taken from CT-scanned images.

Key results that emerged from this work include: (1) The accuracy of the IBM has been validated with in-vitro laboratory experiments, demonstrated a great agreement with a maximum error of 3.04 %; (2) The structure and complexity of the vascular network affect the ice ball deformation, with increasing ice-ball irregularity for greater blood vessel complexity; and (3) introducing nanoparticles can significantly increase the freezing area by enhancing the rate of freezing, especially for the problem embedded with large blood vessels.

Chapter 7

Three Dimensional Analysis of Vascular Tissue Cryo-freezing

Chapter 7 studies the clinically-extracted vascular tissue for 3D problems using the iterative immersed boundary method. The experimental validation with various configurations of blood vessels was conducted. The results show a satisfactory agreement with the numerical results. The vascular complexity and the ice-ball shape irregularity are analyzed and compared for both the 2D and 3D simulations with different vessel configurations and developments.

Chapter 7 Three Dimensional Analysis of Vascular Tissue Cryo-freezing

7.1 Numerical Method

For the three-dimensional numerical simulation, a n-furcated liver vessels model from a 3D segmented volume using hole making and subdivision methods [143] is applied for our study. Overcoming the influence of the tiny size, noise and n-furcations of vessels [144-147], this method can build an accurate and smooth liver vessel model. In this model, holes are made on a coarse mesh, and a final fine mesh is generated using a subdivision method. The hole-making approach with the subdivision method provides good efficiency in mesh construction as well as good flexibilities in mesh editing. Experiments show that this method can automatically construct smooth mesh models for n-furcated vessels with mean absolute error of 0.92 voxel and mean relative error of 0.17. It is promising to be used in diagnosis, analysis, and surgery simulation of liver diseases, and is able to model tubular structures with tree topology.

To capture the detailed information of the complex blood vessels, the mesh size of boundary points according to the 3D models is very large. This will require lots of data memory space while calculating,

$$\mathbf{AX} = \mathbf{B} \tag{31}$$

As the size of matrix A will be as large as the mesh size's square, if following the matrix method we applied before, huge memory requirement becomes a problem.

$$\mathbf{A}=\frac{\Delta t}{\rho_t c_t}h^2\begin{pmatrix} D_{11} & D_{12} & \cdots & D_{1N} \\ D_{21} & D_{22} & \cdots & D_{2N} \\ \vdots & \vdots & \ddots & \vdots \\ D_{M1} & D_{M2} & \cdots & D_{MN} \end{pmatrix}\begin{pmatrix} D_{11}\Delta s_1 & D_{21}\Delta s_2 & \cdots & D_{M1}\Delta s_M \\ D_{12}\Delta s_1 & D_{22}\Delta s_2 & \cdots & D_{M2}\Delta s_M \\ \vdots & \vdots & \ddots & \vdots \\ D_{1N}\Delta s_1 & D_{2N}\Delta s_2 & \cdots & D_{MN}\Delta s_M \end{pmatrix} \tag{32}$$

Hence, we use the iterative method instead of the matrix method for the calculation of the 3D model. Compared with the matrix method, the iterative method has such advantages that it is able to calculate the complex geometry with larger mesh size, and it is easier to understand and repeat. The detailed procedure of the Predictor-Corrector step obtaining the temperature correction is shown as the following.

(1) Predictor step:

The predictor step is the same as the previous method. Following the step in Chapter 3.3.2, we can obtain the predicted temperature $T^*(\mathbf{x},t)$.

(2) Corrector step:

As the boundary temperature T_B at the Lagrangian points can be calculated following such formula,

$$T_B\left(\mathbf{X}_B^i,t\right)=\sum_j T(\mathbf{x}_j,t)D\left(\mathbf{x}_j-\mathbf{X}_B^i\right)h^2 \text{ for } (i=1,2,...,M;\ j=1,2,...N) \tag{29}$$

Using the predicted temperature $T^*(\mathbf{x},t)$, we can obtain a predicted boundary temperature,

$$T_B{}^*\left(\mathbf{X}_B^i,t\right)=\sum_j T^*(\mathbf{x}_j,t)D\left(\mathbf{x}_j-\mathbf{X}_B^i\right)h^2 \text{ for } (i=1,2,...,M;\ j=1,2,...N) \tag{41}$$

Then the temperature difference at the Lagrangian points can be calculated as the following,

$$\Delta T_B^{\,*}\left(\mathbf{X}_B^i,t\right)=T_B\left(\mathbf{X}_B^i,t\right)-T_B^{\,*}\left(\mathbf{X}_B^i,t\right) \tag{42}$$

So the temperature difference at the Eulerian points can be obtained,

$$\Delta T^*\left(\mathbf{x}_j,t\right)=\sum_{i=1}^{M}\delta T_B^{\,*}\left(\mathbf{X}_B^i,t\right)D\left(\mathbf{x}_j-\mathbf{X}_B^i\right)\Delta s_i \text{ for } (i=1,2,...,M;\ j=1,2,...,N) \tag{43}$$

As a result, the corrected temperature for one iterative step is obtained,

$$T_1=T^*+\Delta T^* \tag{44}$$

Then repeat the procedure (41), (42), (43) and (44), until the convergence condition $\left|\Delta T_B^{\,*}\left(\mathbf{X}_B^i,t\right)=T_B\left(\mathbf{X}_B^i,t\right)-T_B^{\,*}\left(\mathbf{X}_B^i,t\right)\right|\le\delta$ is satisfied.

7.2 Experimental Validation

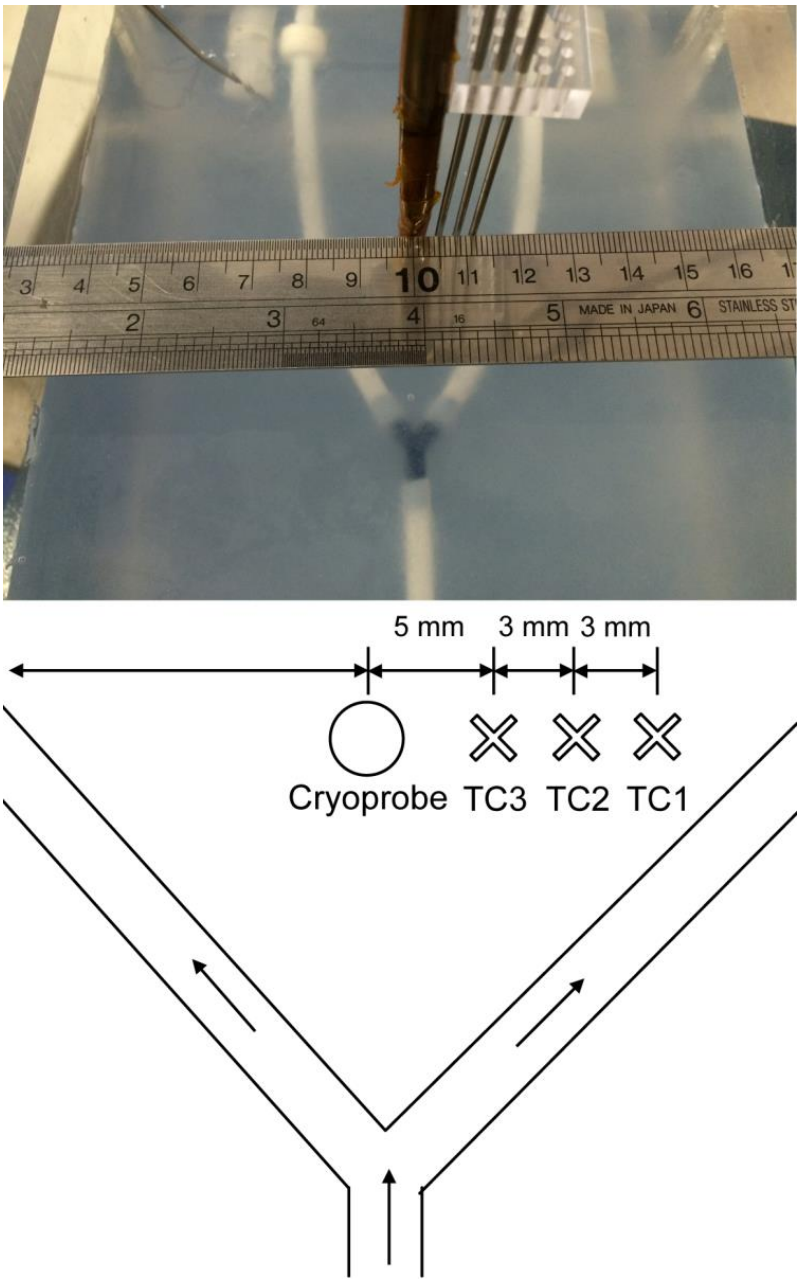

Figure 35 The layout of thermocouples, blood vessels and cryoprobe for the Y shape vessel structure.

To validate the 3D iterative method, the experiments with various configurations of blood vessels are conducted. Figure 35 shows the experimental setup and the schematic diagram of the layout of the blood vessel, thermocouples and the

cryoprobe for the Y shape vessel structure. The distance between the cryoprobe and the thermocouple is 5 mm and the distance between each thermocouple is 3 mm. The angle of the two branches is measured as 30 degrees.

Figure 36 shows the experimental validation for the Y shape vessel structure. (a) is for experimental results of blood vessel with 4 mm diameter while (b) is for the experimental results of blood vessel with 6 mm diameter. (1) is the outlet temperature of the blood flow from the freezing area; (2) is the experimental data of temperature response for thermocouples and cryoprobe; (3) is the validation between experimental data and the numerical results for TC3 and (4) is the validation between experimental data and the numerical results for TC1.

The outlet water temperature from the experimentally-simulated blood vessel is shown in Figure 36(a-1) and Figure 36(b-1), with the inlet temperature of the blood flow is controlled as 37 °C ± 1.5 °C (calibrated mean thermocouple probes' accuracy). It is readily observed as a relatively constant value from 200 s to 1200 s. The average outlet temperature for the case (a-1) is 38.1 ℃, while the average outlet temperature of the case (b-1) is 37.5 ℃.

The experimental validation for the three dimensional model in TC1 is shown in Figure 36(a-4) and Figure 36(b-4). As shown in Figure 36(a-4), for the case with blood vessel diameter of 4 mm, at the end of 20 min cryo-freezing, the temperature difference is 0.5 ℃ while the maximum difference is obtained to be 1.8 ℃ during the entire freezing time. For the case with blood vessel diameter of 6 mm in Figure 36(b-4), TC1 registers a temperature difference of 0.1 ℃ at the end of 20 mins cryo-

freezing while the maximum difference in temperature is observed to be 2.9 ℃ over the whole freezing duration. Similar phenomenon can be observed in Figure 36(a-3) and Figure 36(b-3), which present the temperature response in TC3.

As we would have expected, our simulation results agree well with the experimental results in the in-vitro platform. Based on these comparisons, we can infer that the 3D model, when applied to study tissue cryo-freezing, is appropriate to analyze the bioheat transfer problem involving tissue and blood vessels.

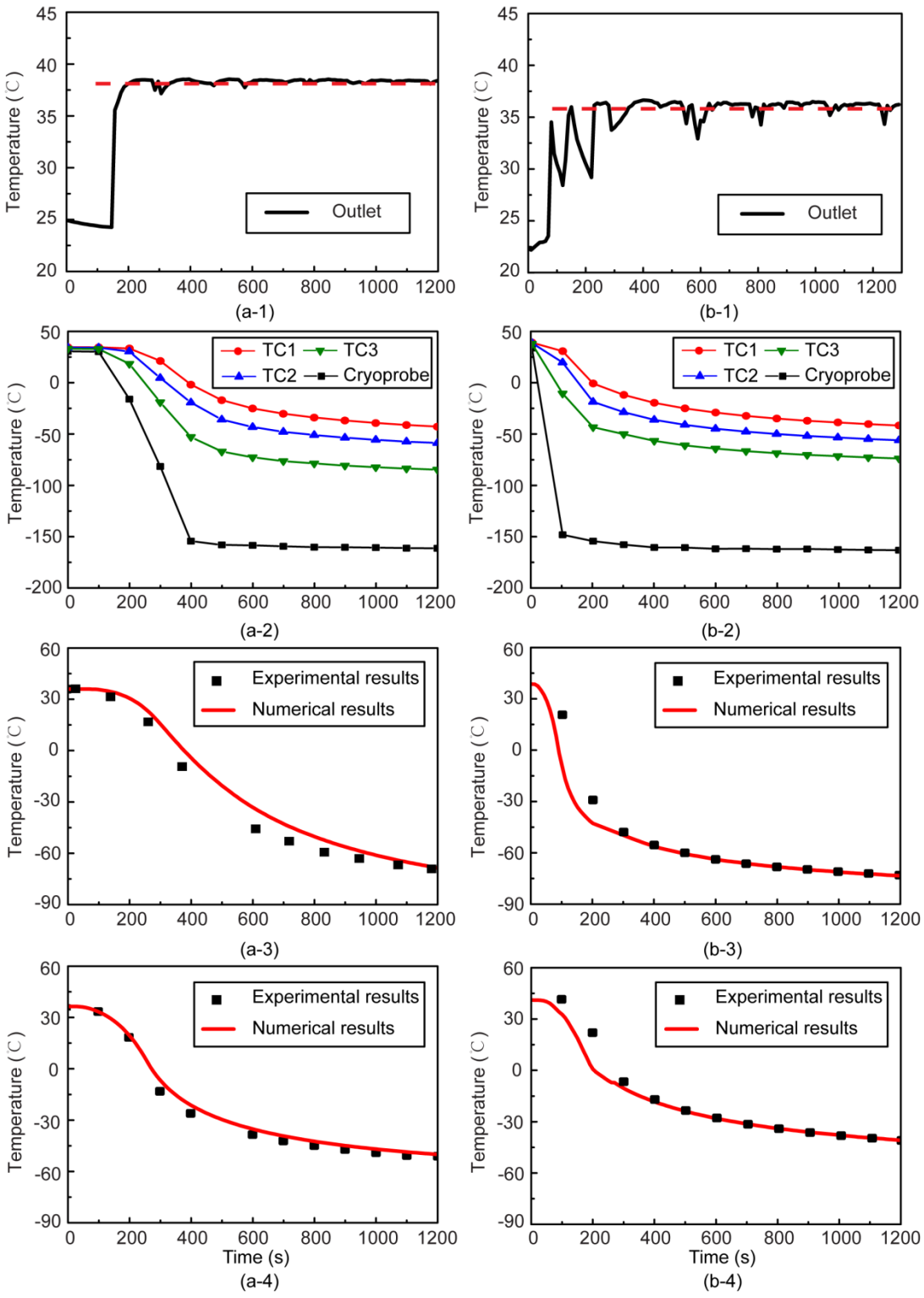

Figure 36 The experimental validation for Y shape blood vessel structure. (a) is for the vessel diameter of 4 mm and (b) is for the vessel diameter of 6 mm. (1) is the outlet temperature of the blood flow from the freezing area; (2) is the experimental data of temperature response for thermocouples and cryoprobe; (3) is the validation between

experimental data and the numerical results for TC3 and (4) is the validation between experimental data and the numerical results for TC1.

7.3 Comparison between 2D and 3D Clinically-extracted Vascular System

7.3.1 Complexity vs Irregularity

To better understand the vascular structure, a new parameter, the blood vessel complexity, is introduced to quantify this. The blood vessel complexity for the 3D model is based on the definition of blood vessel complexity for the 2D model. Considering a cube in a 3D case, the blood vessel structure can be projected onto the x-y plane, the y-z plane and the x-z plane. Following the definition of the 2D model, the complexity of the x-y plane, the y-z plane and the x-z plane can be presented as β_{x-y}, β_{y-z}, and β_{x-z}, respectively.

Consider the cube with the dimensions of

$$\begin{cases} X = a_x \\ Y = a_y \\ Z = a_z \end{cases} \tag{45}$$

The volume of the cube can be calculated as

$$V = a_x \cdot a_y \cdot a_z . \tag{46}$$

As a result, the vessel complexity for the 3D model is

$$\vec{\beta} = \left(\beta_{x-y}, \beta_{y-z}, \beta_{x-z}\right) \tag{47}$$

For comparison, the p-norm is used to represent the size of $\vec{\beta}$.

$$\left\|\vec{\beta}\right\|_p = \left(\left|\beta_{x-y}\right|^p + \left|\beta_{y-z}\right|^p + \left|\beta_{x-z}\right|^p\right)^{\frac{1}{p}} \tag{48}$$

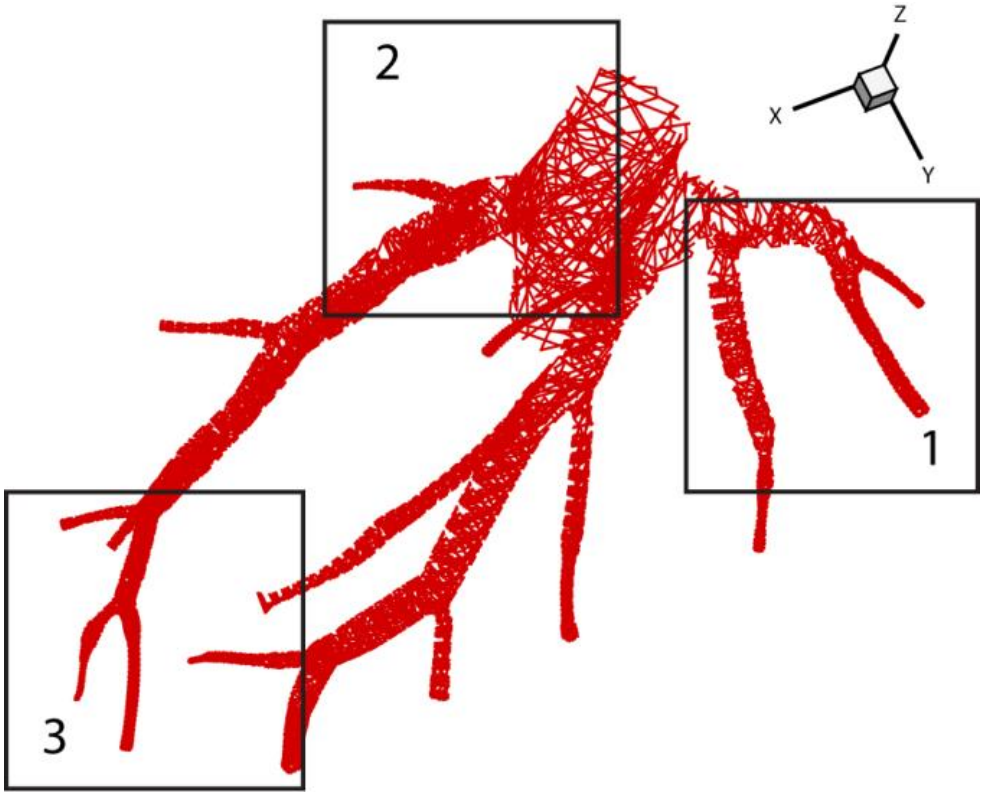

Figure 37 The 3D view of the hepatic vein. 1, 2, and 3 presents three different areas with different blood vessel complexities.

To analyze the influence of vessel complexity for both the 2D and 3D problems, we choose the areas as shown in Figure 37 for the next study. Changes in the ice ball irregularity with the blood vessel complexity are calculated for 2D problems along x-y plane. After projecting the isotherm to the x-y plane, we also calculate the ice ball irregularity for 3D problems. The results are shown in Figure 38.

As can be seen, for both the 2D and 3D cases, with the increasing of blood vessel complexity, the ice ball becomes more and more irregular. That is due to the

thermal effects brought by the large blood vessels. Considered as the Dirichlet boundary condition, the blood vessel complexity will highly impact the temperature change of the surrounding tumor, thus affecting the shape of the growing ice-ball.

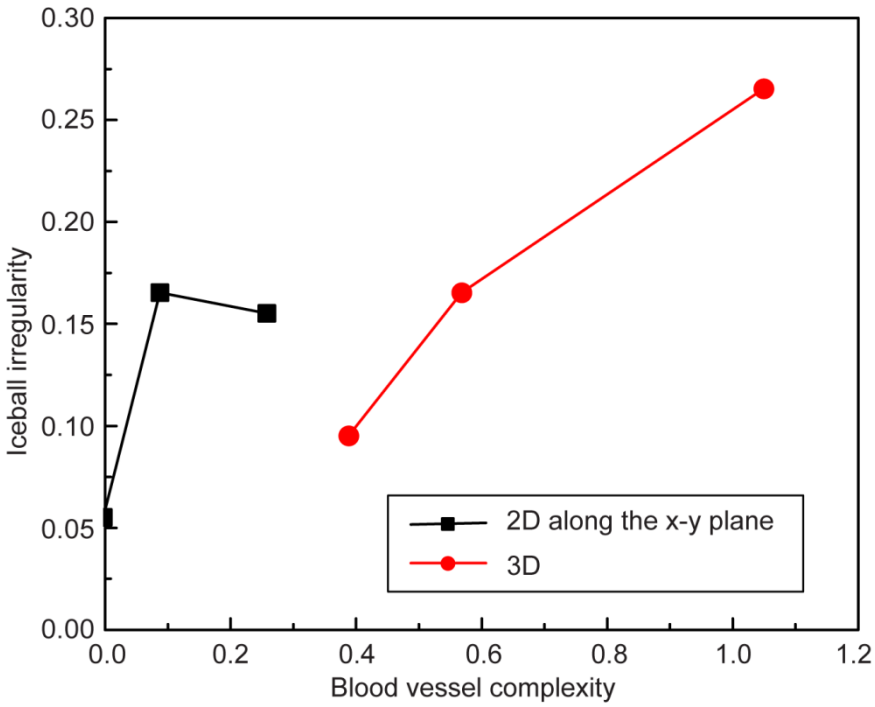

Figure 38 The ice-ball irregularity change with different blood vessel complexities for both 2D and 3D model.

7.3.2 The Growing of Vascular System

Literature reviews have shown that the arrangement of vessels in the organism is influenced by general physical laws as well as specific physiological requirements [148]. Murray first proposed Murray's law in 1926 to describe the branching network in cardiovascular system [149]. However, most studies on cryo-freezing with blood vessels did not consider the fractal tree-like branched network [6] or treated it as an effective one [121].

In this section, the branched network system is introduced and the tree-like fractal structure of blood vessel with N=2 and m=4 is shown in Figure 39. Each branch of the network is divided into N=2 branches until required branching level (m=4 in this case) is reached. The structure can be expanded by repeating the elemental branch. For the simulation case, the contact angle is set as 30 degree, which is the same as the experimental study.

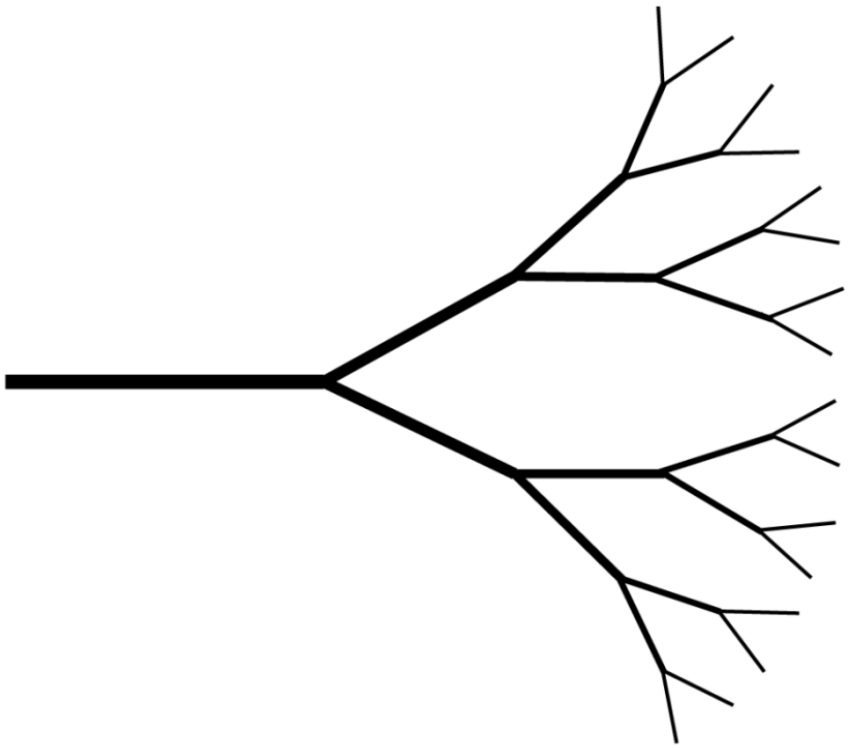

Figure 39 Diagram of tree-like branched fractal structure of blood vessels. The branch number N=2 and the branching level m=4.

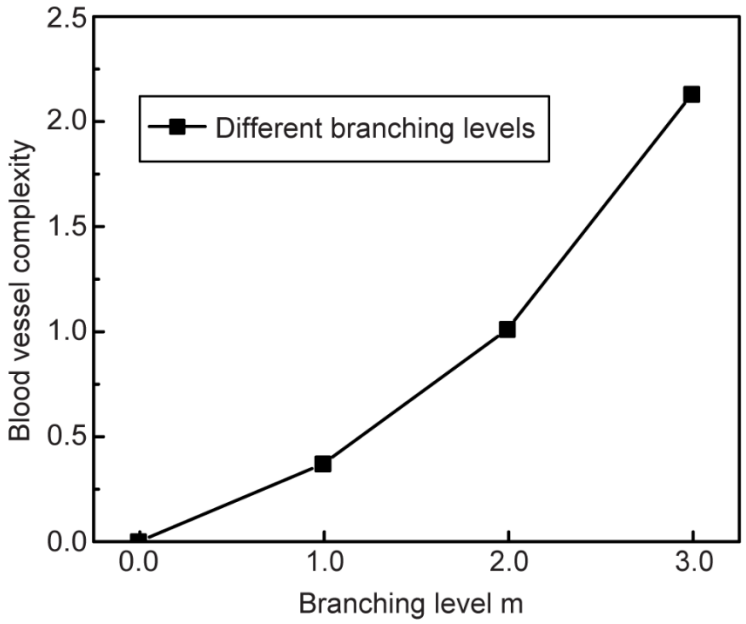

Figure 40 The Blood vessel complexity with increasing branching level m.

Figure 40 shows the blood vessel complexity change with the increasing branching level. It is apparent that with the increasing of branching levels, the blood vessel complexity is also increased. This will significantly enhance the difficulty in numerical calculations.

For the clinical application, the area of the ablation zone per unit time is an important parameter to evaluate the freezing efficiency. Figure 41 shows the area of the ablation zone during numerical calculation of cryo-freezing with different branching levels. As can be seen in both 2D and 3D studies, with the increasing of branching level, the total area of the ablation zone significantly reduces. This is because more heat will be brought into the computational area by the blood flow with larger branching levels. In the period between 0 s and 300 s, the area of the ablation zone increases at a rate much higher than the period between 300 s and 1800

s. That is because the temperature of the cryoprobe becomes stable after freezing for 300 s, thus leading to the low freezing rate of the tissue.

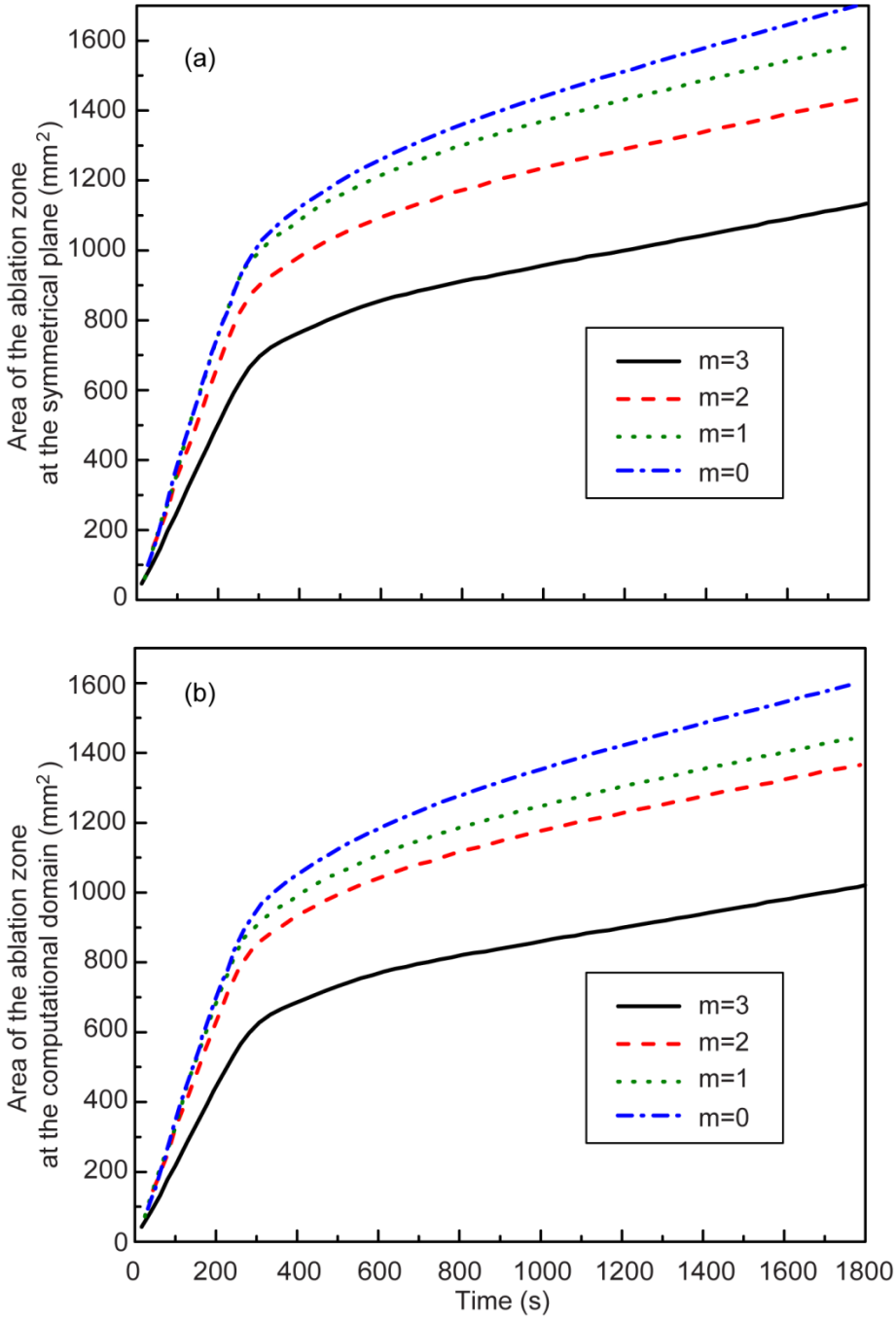

Figure 41 Comparison of the size of complete ablation zones for different branching levels. (a) is for 3D model and (b) is for the 2D model.

7.4 Summary

In this chapter, the developed IBM solver is applied in solving the three-dimensional cryo-freezing problem with immersed large blood vessels. A combination model of the Pennes bio-heat transfer model and the immersed boundary method is validated, by comparing with the in-vitro experiments with different configurations.

The temperature response predicted by the model is in great agreement with the experimental data after freezing for 1200 s. The maximum error of the validation study is 1.8 ℃ and 2.9 ℃ for blood vessel diameter of 4.0 mm and 6.0 mm, respectively. The comparison between the numerical results and the experimental results shows that the model can be successfully applied to simulate the cryo-freezing process for the 3D physical problem. More specific study presents that the structure and complexity of the vascular network can highly affect the ice ball deformation, with increasing ice-ball irregularity for greater blood vessel complexity.

This page has been left blank intentionally.

Chapter 8

Conclusions and

Future Recommendations

Conclusions of this thesis and the contributions to the knowledge obtained in this dissertation are summarized in this chapter. Besides, the limitations associated with this study are discussed. Several recommendations are proposed for the future work.

Chapter 8 Conclusions and Future Recommendations

8.1 Conclusions

This dissertation explored the analysis of the cryo-freezing process. With the background and literature review in Chapter 1 and Chapter 2, readers can have a brief understanding on the development of cryosurgery and its numerical analysis methods. Chapter 3 and Chapter 4 are the experimental and numerical methodologies used in this study, respectively.

Chapter 5, Chapter 6 and Chapter 7 contain all results obtained in this dissertation. Chapter 5 takes mesh independence study and validates the model with others researchers' work while Chapter 6 and Chapter 7 consider the 2D and 3D models of the physical vascular system for liver tumor. Both experiments and numerical simulations have been conducted. The influence of blood vessel complexity and the injected nanoparticles are studied. The results have shown that the model with the immersed boundary method can successfully be applied to predict the cryo-freezing process.

In Chapter 5, the performance of proposed bio-heat model with immersed boundary method is investigated based on the existing experimental and numerical data from literatures. The numerical results exhibit good agreement with maximum errors of 1.7 % and 1.5 % for simulation and experimental comparisons, respectively. In a selected case study, the model has demonstrated the existence of a threshold distance to effectively freeze on the tissue right next to a major blood vessel according to the tissue temperature response as well as the position of the freezing

fronts, namely, 0 ℃ and -40 ℃. Additionally, the model allows ease of tracking the position of the two critical freezing fronts when applied to tissue cryo-freezing.

In Chapter 6, the effects of parameters on the mechanisms underlying the cryo-freezing of a 2D liver tumor model are investigated. The model includes an accurately designed platform with complex blood vessel network taken from CT-scanned images. The accuracy of the method has been validated with in-vitro laboratory experiments, demonstrated a great agreement with a maximum error of 3.04 %. Additionally, introducing nanoparticles can significantly increase the freezing area by enhancing the rate of freezing. It is apparent from this work that applying the IBM to solve the bioheat model holds a huge potential for predicting tissue temperature distributions particularly when the tissue is embedded with complex vascularized network.

In Chapter 7, the developed IBM solver is applied in solving the three-dimensional cryo-freezing problem with immersed large blood vessels. The temperature response predicted by the model is in great agreement with the experimental data after freezing for 1200 s. The maximum error of the validation study is 1.8 ℃ and 2.9 ℃ for blood vessel diameter of 4.0 mm and 6.0 mm, respectively. More specific study presents that the structure and complexity of the vascular network can highly affect the ice ball deformation, with increasing ice-ball irregularity for greater blood vessel complexity.

8.2 Key Contributions to Knowledge

The model developed in this study has been shown to be efficient to predict the temperature distribution with time in the cryo-freezing process with large blood vessels. The contributions of this thesis are summarized as:

a) This study develops a novel mathematical model incorporating immersed boundary method (IBM) to study the thermal effect due to blood vessels and also the ice ball propagation. This model can be used for more complex vessels' structure and clinically situations as well as cut down the computational memory and reduce the modelling complexity. The major advantage of the present method is that the generation of complex mesh is no longer required.

b) By using the controlled experiments analysis, the flow rate is found to be the major influencing factor for the temperature response while the vessel structure exerts the major impact on the ice-ball formation.

c) The blood vessel complexity and the ice-ball shape irregularity are first proposed to evaluate the vessel structure and the cryo-freezing results. The lethal fronts and freezing fronts can help to evaluate the freezing efficiency quantitatively.

d) Incorporating a CT-scanned vascular image into cryosurgery planning enables cryosurgeons to achieve greater success rates by knowing how the isotherm at the critical temperature (i.e. 233 K) moves in the vascular tissue. The heating effects produced by large vessels generate less thermal impacts on tissue with low freezing temperatures than tissue with high freezing temperatures, due to the formation of the buffer zone.

e) The cryosurgical therapy with nanoparticles is efficient to enhance the freezing rate and reduce the size of unwanted frozen tissue. Although nanofluid with high concentration performs better, the nanoparticles' thermal conductivity plays a more important role on the cryo-freezing efficiency.

8.3 Limitations and Further Work

Considering the research in this area is still at an infant stage, the following aspects are recommended for the future work.

a) It is acknowledged that this model did not involve the material parameters of the human tissue and the real tumor at the low temperature, due to the limited experimental data for them. Further research is needed to measure such parameters as heat capacity and thermal conductivity. The main challenge is how to accurately measure the changing parameters at an extremely low temperature.

b) The heat conductive model developed in this study is not able to consider the influence of blood flow as well as the convective effects. In the area of heat transfer simulation, there is a need to extend the 1^{st} boundary condition to the 2^{rd} boundary condition, in order to solve the convective problems.

c) The mechanism of the cell freezing and the cell damage is not taken into account in the model, while the ambient tissue is assumed as homogenous. Future research should attempt to modify the present model by completing it and considering the cell freezing and cell damage mechanisms.

d) The comparison between the simulation results and clinical validation remains an open problem for almost all biomedical studies. It is recommended that an in-vivo or even clinical experiment of the cryo-freezing be carried out.

REFERENCES

[1] M. A. Solovchuk, T. W. H. Sheu, W. L. Lin, I. Kuo, and M. Thiriet, "Simulation study on acoustic streaming and convective cooling in blood vessels during a high-intensity focused ultrasound thermal ablation," *International Journal of Heat and Mass Transfer,* vol. 55, pp. 1261-1270, Jan 31 2012.

[2] A. Jemal, F. Bray, M. M. Center, J. Ferlay, E. Ward, and D. Forman, "Global cancer statistics," *CA: a cancer journal for clinicians,* vol. 61, pp. 69-90, 2011.

[3] J. Seifert and D. Morris, "Indicators of recurrence following cryotherapy for hepatic metastases from colorectal cancer," *British Journal of Surgery,* vol. 86, pp. 234-240, 1999.

[4] T. Mala, L. Frich, L. Aurdal, O. P. Clausen, B. Edwin, O. Soreide, *et al.*, "Hepatic vascular inflow occlusion enhances tissue destruction during cryoablation of porcine liver," *J Surg Res,* vol. 115, pp. 265-71, Dec 2003.

[5] C. Kim, A. P. O'Rourke, D. M. Mahvi, and J. G. Webster, "Finite-element analysis of ex vivo and in vivo hepatic cryoablation," *Ieee Transactions on Biomedical Engineering,* vol. 54, pp. 1177-1185, Jul 2007.

[6] C. Kim, A. P. O'Rourke, J. A. Will, D. M. Mahvi, and J. G. Webster, "Finite-element analysis of hepatic cryoablation around a large blood vessel," *Ieee Transactions on Biomedical Engineering,* vol. 55, pp. 2087-2093, Aug 2008.

[7] X. Xue, Z. Z. He, and J. Liu, "Computational study of thermal effects of large blood vessels in human knee joint," *Computers in biology and medicine,* vol. 43, pp. 63-72, 2013.

[8] C. S. Peskin, "Flow patterns around heart valves: a numerical method," *Journal of Computational Physics,* vol. 10, pp. 252-271, 1972.

[9] W. W. Ren, C. Shu, J. Wu, and W. M. Yang, "Boundary condition-enforced immersed boundary method for thermal flow problems with Dirichlet temperature condition and its applications," *Computers & Fluids*, vol. 57, pp. 40-51, Mar 30 2012.

[10] J. Ferlay and I. A. f. R. o. Cancer, *GLOBOCAN 2000: cancer incidence, mortality and prevalence worldwide*: IARC press, 2001.

[11] A. G. Knudson, "Two genetic hits (more or less) to cancer," *Nature Reviews Cancer*, vol. 1, pp. 157-162, 2001.

[12] P. Anand, A. B. Kunnumakara, C. Sundaram, K. B. Harikumar, S. T. Tharakan, O. S. Lai, *et al.*, "Cancer is a preventable disease that requires major lifestyle changes," *Pharmaceutical research*, vol. 25, pp. 2097-2116, 2008.

[13] J. Arnott, *On the treatment of cancer, by the regulated application of an anaesthetic temperature* vol. 1, 1855.

[14] L. Cailletet, "Recherches sur la liquéfaction des gaz," *Ann Chemie Physique*, vol. 15, pp. 132-44, 1878.

[15] S. Cooper and R. Dawber, "The history of cryosurgery," *Journal of the royal society of medicine*, vol. 94, pp. 196-201, 2001.

[16] H. T. Meryman, "Cryobiology," *Cryobiology*, 1966.

[17] E. J. Woods, J. D. Benson, Y. Agca, and J. K. Critser, "Fundamental cryobiology of reproductive cells and tissues," *Cryobiology*, vol. 48, pp. 146-156, 2004.

[18] P. Mazur, "The role of intracellular freezing in the death of cells cooled at supraoptimal rates," *Cryobiology*, vol. 14, pp. 251-272, 1977.

[19] P. Hewitt, J. Zhao, J. a. Akhter, and D. Morris, "A comparative laboratory study of liquid nitrogen and argon gas cryosurgery systems," *Cryobiology*, vol. 35, pp. 303-308, 1997.

[20] Y. Moore, P. Sofer, and M. Ilovich, "The science and technology behind cryosurgery," *Technical Notes*, vol. 3, pp. 1-4, 2001.

[21] R. C. Marcove and T. R. Miller, "Treatment of primary and metastatic bone tumors by cryosurgery," *Jama*, vol. 207, pp. 1890-1894, 1969.

[22] R. C. Marcove, D. S. Sheth, E. W. Brien, A. G. Huvos, and J. H. Healey, "Conservative surgery for giant cell tumors of the sacrum. The role of cryosurgery as a supplement to curettage and partial excision," *Cancer,* vol. 74, pp. 1253-1260, 1994.

[23] H. Bart Schreuder, H. B. Van Beem, and R. P. Veth, "Venous gas embolism during cryosurgery for bone tumors," *Journal of surgical oncology*, vol. 60, pp. 196-200, 1995.

[24] I. S. COOPER and A. S. J. LEE, "Cryostatic congelation: a system for producing a limited, controlled region of cooling or freezing of biologic tissues," *The Journal of nervous and mental disease,* vol. 133, pp. 259-263, 1961.

[25] K. L. Reed, T. D. Brown, and M. G. Conzemius, "Focal cryogen insults for inducing segmental osteonecrosis: computational and experimental assessments of thermal fields," *Journal of biomechanics,* vol. 36, pp. 1317-1326, 2003.

[26] T.-H. Yu, J. Liu, and Y.-X. Zhou, "Selective freezing of target biological tissues after injection of solutions with specific thermal properties," *Cryobiology,* vol. 50, pp. 174-182, 2005.

[27] A. A. Gage and J. Baust, "Mechanisms of tissue injury in cryosurgery," *Cryobiology,* vol. 37, pp. 171-186, 1998.

[28] P. Mazur, "Freezing of living cells: mechanisms and implications," *American Journal of Physiology-Cell Physiology,* vol. 247, pp. C125-C142, 1984.

[29] Z. Q. Sun, Y. Yang, and J. Liu, "In Vivo Experiments and Numerical Investigations on Nanocryosurgical Freezing of Target Tissues with Large

Blood Vessels," *Journal of Biomedical Nanotechnology,* vol. 8, pp. 10-18, Feb 2012.

[30] P. Rattanadecho and P. Keangin, "Numerical study of heat transfer and blood flow in two-layered porous liver tissue during microwave ablation process using single and double slot antenna," *International Journal of Heat and Mass Transfer,* vol. 58, pp. 457-470, Mar 2013.

[31] X. Zhao and K. J. Chua, "Studying the thermal effects of a clinically-extracted vascular tissue during cryo-freezing," *Journal of Thermal Biology,* vol. 37, pp. 556-563, 2012.

[32] X. Xue, Z. Z. He, and J. Liu, "Computational study of thermal effects of large blood vessels in human knee joint," *Comput Biol Med,* vol. 43, pp. 63-72, Jan 2013.

[33] J. Shi, Z. Chen, and M. Shi, "Simulation of heat transfer of biological tissue during cryosurgery based on vascular trees," *Applied Thermal Engineering,* vol. 29, pp. 1792-1798, 2009.

[34] P. Xu, B. Yu, M. Yun, and M. Zou, "Heat conduction in fractal tree-like branched networks," *International Journal of Heat and Mass Transfer,* vol. 49, pp. 3746-3751, 2006.

[35] Z. S. Deng and J. Liu, "Effect of configuration between cryoprobe and large blood vessels on the tissue freezing during cryosurgery," *2005 27th Annual International Conference of the IEEE Engineering in Medicine and Biology Society, Vols 1-7,* pp. 490-493, 2005.

[36] W. Jungraithmayr, M. Szarzynski, H. Neeff, J. Haberstroh, G. Kirste, A. Schmitt-Graeff, *et al.,* "Significance of total vascular exclusion for hepatic cryotherapy: an experimental study," *Journal of Surgical Research,* vol. 116, pp. 32-41, 2004.

[37] J. Chato, "Heat transfer to blood vessels," *Journal of biomechanical engineering,* vol. 102, pp. 110-118, 1980.

[38] O. I. Craciunescu and S. T. Clegg, "Pulsatile blood flow effects on temperature distribution and heat transfer in rigid vessels," *J Biomech Eng,* vol. 123, pp. 500-5, Oct 2001.

[39] Y. Zhang, J. Liu, and Y. Zhou, "Pilot study on cryogenic heat transfer in biological tissues embedded with large blood vessels," *Forschung im Ingenieurwesen,* vol. 67, pp. 188-197, 2002.

[40] J. Crezee and J. Lagendijk, "Temperature uniformity during hyperthermia: the impact of large vessels," *Physics in medicine and biology,* vol. 37, p. 1321, 1992.

[41] W. Berger and J. Poledna, "New strategies for the placement of cryoprobes in malignant tumors of the liver for reducing the probability of recurrences after hepatic cryosurgery," *International journal of colorectal disease,* vol. 16, pp. 331-339, 2001.

[42] T. Mala, L. Frich, L. Aurdal, O. P. Clausen, B. Edwin, O. Søreide, *et al.*, "Hepatic vascular inflow occlusion enhances tissue destruction during cryoablation of porcine liver 1," *Journal of Surgical Research,* vol. 115, pp. 265-271, 2003.

[43] J. C. Saliken, J. G. McKinnon, and R. Gray, "CT for monitoring cryotherapy," *AJR. American journal of roentgenology,* vol. 166, pp. 853-855, 1996.

[44] J. C. Rewcastle, G. A. Sandison, L. J. Hahn, J. C. Saliken, J. G. McKinnon, and B. J. Donnelly, "A model for the time-dependent thermal distribution within an iceball surrounding a cryoprobe," *Physics in Medicine and Biology,* vol. 43, p. 3519, 1998.

[45] T. Peng, D. O'Neill, and S. Payne, "A two-equation coupled system for determination of liver tissue temperature during thermal ablation," *International Journal of Heat and Mass Transfer,* vol. 54, pp. 2100-2109, 2011.

[46] F. Zhao, Z.-q. Chen, and M.-h. Shi, "Numerical study on freezing-thawing phase change heat transfer in biological tissue embedded with two cryoprobes," *Journal of Central South University of Technology,* vol. 16, pp. 326-331, 2009.

[47] M. R. Rossi and Y. Rabin, "Experimental verification of numerical simulations of cryosurgery with application to computerized planning," *Physics in medicine and biology,* vol. 52, p. 4553, 2007.

[48] E. Neufeld, N. Chavannes, T. Samaras, and N. Kuster, "Novel conformal technique to reduce staircasing artifacts at material boundaries for FDTD modeling of the bioheat equation," *Physics in medicine and biology,* vol. 52, p. 4371, 2007.

[49] L. A. Dombrovsky, V. Timchenko, and M. Jackson, "Indirect heating strategy for laser induced hyperthermia: An advanced thermal model," *International Journal of Heat and Mass Transfer,* vol. 55, pp. 4688-4700, 2012.

[50] Z. Z. He, X. Xue, and J. Liu, "An Effective Finite Difference Method for Simulation of Bioheat Transfer in Irregular Tissues," *Journal of Heat Transfer-Transactions of the Asme,* vol. 135, Jul 2013.

[51] C. Jin, Z. He, and J. Liu, "MRI-based finite element simulation on radiofrequency ablation of thyroid cancer," *Computer methods and programs in biomedicine,* vol. 113, pp. 529-538, 2014.

[52] C. Jin, Z. Z. He, Y. Yang, and J. Liu, "MRI-based three-dimensional thermal physiological characterization of thyroid gland of human body," *Medical engineering & physics,* vol. 36, pp. 16-25, 2014.

[53] M. Y. Ge, K. J. Chua, C. Shu, and W. M. Yang, "Analytical and numerical study of tissue cryofreezing via the immersed boundary method," *International Journal of Heat and Mass Transfer,* vol. 83, pp. 1-10, Apr 2015.

[54] J. D. Anderson and J. Wendt, *Computational fluid dynamics* vol. 206: Springer, 1995.

[55] T. Chung, *Computational fluid dynamics*: Cambridge university press, 2010.

[56] W. J. Gordon and C. A. Hall, "Construction of curvilinear co ‐ ordinate systems and applications to mesh generation," *International Journal for Numerical Methods in Engineering,* vol. 7, pp. 461-477, 1973.

[57] M. Prevost, M. G. Edwards, and M. J. Blunt, "Streamline tracing on curvilinear structured and unstructured grids," in *SPE Reservoir Simulation Symposium,* 2001.

[58] S. J. Owen, "A Survey of Unstructured Mesh Generation Technology," in *IMR*, 1998, pp. 239-267.

[59] C. Ollivier-Gooch and M. Van Altena, "A high-order-accurate unstructured mesh finite-volume scheme for the advection–diffusion equation," *Journal of Computational Physics,* vol. 181, pp. 729-752, 2002.

[60] S. Rebay, "Efficient unstructured mesh generation by means of Delaunay triangulation and Bowyer-Watson algorithm," *Journal of computational physics,* vol. 106, pp. 125-138, 1993.

[61] C. Bailey and M. Cross, "A finite volume procedure to solve elastic solid mechanics problems in three dimensions on an unstructured mesh," *International journal for numerical methods in engineering,* vol. 38, pp. 1757-1776, 1995.

[62] Y.-H. Tseng and J. H. Ferziger, "A ghost-cell immersed boundary method for flow in complex geometry," *Journal of computational physics,* vol. 192, pp. 593-623, 2003.

[63] D. Pan and T. T. Shen, "Computation of incompressible flows with immersed bodies by a simple ghost cell method," *International journal for numerical methods in fluids,* vol. 60, pp. 1378-1401, 2009.

[64] S. Majumdar, G. Iaccarino, and P. Durbin, "RANS solvers with adaptive structured boundary non-conforming grids," *Annual Research Briefs, Center for Turbulence Research, Stanford University*, pp. 353-466, 2001.

[65] T. Ye, R. Mittal, H. Udaykumar, and W. Shyy, "An accurate Cartesian grid method for viscous incompressible flows with complex immersed boundaries," *Journal of computational physics*, vol. 156, pp. 209-240, 1999.

[66] M.-H. Chung, "Cartesian cut cell approach for simulating incompressible flows with rigid bodies of arbitrary shape," *Computers & Fluids*, vol. 35, pp. 607-623, 2006.

[67] R. J. Leveque and Z. Li, "The immersed interface method for elliptic equations with discontinuous coefficients and singular sources," *SIAM Journal on Numerical Analysis*, vol. 31, pp. 1019-1044, 1994.

[68] R. J. LeVeque and Z. Li, "Immersed interface methods for Stokes flow with elastic boundaries or surface tension," *SIAM Journal on Scientific Computing*, vol. 18, pp. 709-735, 1997.

[69] Z. Li and M.-C. Lai, "The immersed interface method for the Navier–Stokes equations with singular forces," *Journal of Computational Physics*, vol. 171, pp. 822-842, 2001.

[70] D.-V. Le, B. C. Khoo, and J. Peraire, "An immersed interface method for viscous incompressible flows involving rigid and flexible boundaries," *Journal of Computational Physics*, vol. 220, pp. 109-138, 2006.

[71] S. Xu and Z. J. Wang, "Systematic derivation of jump conditions for the immersed interface method in three-dimensional flow simulation," *SIAM Journal on Scientific Computing*, vol. 27, pp. 1948-1980, 2006.

[72] R. Glowinski, T.-W. Pan, and J. Periaux, "A fictitious domain method for external incompressible viscous flow modeled by Navier-Stokes equations," *Computer Methods in Applied Mechanics and Engineering*, vol. 112, pp. 133-148, 1994.

[73] R. Glowinski, T.-W. Pan, and J. Periaux, "A Lagrange multiplier/fictitious domain method for the Dirichlet problem—Generalization to some flow problems," *Japan Journal of Industrial and Applied Mathematics,* vol. 12, pp. 87-108, 1995.

[74] Z. Yu, X. Shao, and A. Wachs, "A fictitious domain method for particulate flows with heat transfer," *Journal of Computational Physics,* vol. 217, pp. 424-452, 2006.

[75] M. C. Lai and C. S. Peskin, "An immersed boundary method with formal second-order accuracy and reduced numerical viscosity," *Journal of Computational Physics,* vol. 160, pp. 705-719, May 20 2000.

[76] C. S. Peskin, "The immersed boundary method," *Acta Numerica,* pp. 479-517, 2002.

[77] R. Mittal and G. Iaccarino, "Immersed boundary methods," *Annu. Rev. Fluid Mech.,* vol. 37, pp. 239-261, 2005.

[78] J. Deng, X. M. Shao, and A. L. Ren, "A new modification of the immersed - boundary method for simulating flows with complex moving boundaries," *International journal for numerical methods in fluids,* vol. 52, pp. 1195-1213, 2006.

[79] J.-I. Choi, R. C. Oberoi, J. R. Edwards, and J. A. Rosati, "An immersed boundary method for complex incompressible flows," *Journal of Computational Physics,* vol. 224, pp. 757-784, 2007.

[80] N. Zhang and Z. C. Zheng, "An improved direct-forcing immersed-boundary method for finite difference applications," *Journal of Computational Physics,* vol. 221, pp. 250-268, 2007.

[81] F. Paravento, M. Pourquie, and B. Boersma, "An immersed boundary method for complex flow and heat transfer," *Flow, Turbulence and Combustion,* vol. 80, pp. 187-206, 2008.

[82] C.-C. Liao and C.-A. Lin, "Simulations of natural and forced convection flows with moving embedded object using immersed boundary method," *Computer Methods in Applied Mechanics and Engineering,* vol. 213, pp. 58-70, 2012.

[83] D. Z. Noor, M.-J. Chern, and T.-L. Horng, "An immersed boundary method to solve fluid–solid interaction problems," *Computational Mechanics,* vol. 44, pp. 447-453, 2009.

[84] R. Ghias, R. Mittal, and H. Dong, "A sharp interface immersed boundary method for compressible viscous flows," *Journal of Computational Physics,* vol. 225, pp. 528-553, 2007.

[85] L. Chen, Y. Yu, and G. Hou, "Sharp-interface immersed boundary lattice Boltzmann method with reduced spurious-pressure oscillations for moving boundaries," *Physical Review E,* vol. 87, p. 053306, 2013.

[86] L. Zhu and C. S. Peskin, "Simulation of a flapping flexible filament in a flowing soap film by the immersed boundary method," *Journal of Computational Physics,* vol. 179, pp. 452-468, 2002.

[87] Y. Kim and C. S. Peskin, "Penalty immersed boundary method for an elastic boundary with mass," *Physics of Fluids (1994-present),* vol. 19, p. 053103, 2007.

[88] M. Francois and W. Shyy, "Computations of drop dynamics with the immersed boundary method, part 1: numerical algorithm and buoyancy-induced effect," *Numerical Heat Transfer: Part B: Fundamentals,* vol. 44, pp. 101-118, 2003.

[89] Y. Kim and C. S. Peskin, "2-D parachute simulation by the immersed boundary method," *SIAM Journal on Scientific Computing,* vol. 28, pp. 2294-2312, 2006.

[90] H. Udaykumar, H.-C. Kan, W. Shyy, and R. Tran-Son-Tay, "Multiphase dynamics in arbitrary geometries on fixed Cartesian grids," *Journal of Computational Physics*, vol. 137, pp. 366-405, 1997.

[91] M.-C. Lai and C. S. Peskin, "An immersed boundary method with formal second-order accuracy and reduced numerical viscosity," *Journal of Computational Physics*, vol. 160, pp. 705-719, 2000.

[92] D. Goldstein, R. Handler, and L. Sirovich, "Modeling a no-slip flow boundary with an external force field," *Journal of Computational Physics*, vol. 105, pp. 354-366, 1993.

[93] E. Fadlun, R. Verzicco, P. Orlandi, and J. Mohd-Yusof, "Combined immersed-boundary finite-difference methods for three-dimensional complex flow simulations," *Journal of computational physics*, vol. 161, pp. 35-60, 2000.

[94] J. Kim, D. Kim, and H. Choi, "An immersed-boundary finite-volume method for simulations of flow in complex geometries," *Journal of Computational Physics*, vol. 171, pp. 132-150, 2001.

[95] E. Balaras, "Modeling complex boundaries using an external force field on fixed Cartesian grids in large-eddy simulations," *Computers & Fluids*, vol. 33, pp. 375-404, 2004.

[96] J. Yang and E. Balaras, "An embedded-boundary formulation for large-eddy simulation of turbulent flows interacting with moving boundaries," *Journal of Computational Physics*, vol. 215, pp. 12-40, 2006.

[97] M. Uhlmann, "An immersed boundary method with direct forcing for the simulation of particulate flows," *Journal of Computational Physics*, vol. 209, pp. 448-476, 2005.

[98] S.-W. Su, M.-C. Lai, and C.-A. Lin, "An immersed boundary technique for simulating complex flows with rigid boundary," *Computers & fluids*, vol. 36, pp. 313-324, 2007.

[99] K. Taira and T. Colonius, "The immersed boundary method: a projection approach," *Journal of Computational Physics*, vol. 225, pp. 2118-2137, 2007.

[100] W. Wang, R. Yin, D. Hao, and Y. Yan, "Modeling and Simulation of Fish-Like Swimming in a Straight-Line Swimming State Using Immersed Boundary Method," *Advances in Mechanical Engineering*, vol. 6, p. 489683, 2014.

[101] J. Mohd-Yusof, "Combined immersed-boundary/B-spline methods for simulations of ow in complex geometries," *Annual Research Briefs. NASA Ames Research Center= Stanford University Center of Turbulence Research: Stanford*, pp. 317-327, 1997.

[102] C. Shu, N. Liu, and Y.-T. Chew, "A novel immersed boundary velocity correction–lattice Boltzmann method and its application to simulate flow past a circular cylinder," *Journal of Computational Physics*, vol. 226, pp. 1607-1622, 2007.

[103] J. Wu and C. Shu, "Implicit velocity correction-based immersed boundary-lattice Boltzmann method and its applications," *Journal of Computational Physics*, vol. 228, pp. 1963-1979, 2009.

[104] D. M. McQueen and C. S. Peskin, "Heart simulation by an immersed boundary method with formal second-order accuracy and reduced numerical viscosity," in *Mechanics for a New Mellennium*, ed: Springer, 2001, pp. 429-444.

[105] K. M. Arthurs, L. C. Moore, C. S. Peskin, E. B. Pitman, and H. Layton, "Modeling arteriolar flow and mass transport using the immersed boundary method," *Journal of Computational Physics*, vol. 147, pp. 402-440, 1998.

[106] C. D. Eggleton and A. S. Popel, "Large deformation of red blood cell ghosts in a simple shear flow," *Physics of Fluids (1994-present)*, vol. 10, pp. 1834-1845, 1998.

[107] R. P. Beyer, "A computational model of the cochlea using the immersed boundary method," *Journal of Computational Physics,* vol. 98, pp. 145-162, 1992.

[108] C. Wu and L. Wang, "Numerical simulations of self-propelled swimming of 3D bionic fish school," *Science in China Series E: Technological Sciences,* vol. 52, pp. 658-669, 2009.

[109] L. A. Miller and C. S. Peskin, "A computational fluid dynamics ofclap and fling'in the smallest insects," *Journal of Experimental Biology,* vol. 208, pp. 195-212, 2005.

[110] F. Sotiropoulos and X. Yang, "Immersed boundary methods for simulating fluid–structure interaction," *Progress in Aerospace Sciences,* vol. 65, pp. 1-21, 2014.

[111] S. Takahashi, T. Nonomura, and K. Fukuda, "A numerical scheme based on an immersed boundary method for compressible turbulent flows with shocks: application to two-dimensional flows around cylinders," *Journal of Applied Mathematics,* vol. 2014, 2014.

[112] Y. Li, E. Jung, W. Lee, H. G. Lee, and J. Kim, "Volume preserving immersed boundary methods for two‐phase fluid flows," *International Journal for Numerical Methods in Fluids,* vol. 69, pp. 842-858, 2012.

[113] J. Du, R. D. Guy, and A. L. Fogelson, "An immersed boundary method for two-fluid mixtures," *Journal of computational physics,* vol. 262, pp. 231-243, 2014.

[114] N. Zhang, Z. Zheng, and S. Eckels, "Study of heat-transfer on the surface of a circular cylinder in flow using an immersed-boundary method," *International Journal of Heat and Fluid Flow,* vol. 29, pp. 1558-1566, 2008.

[115] Z. Wang, J. Fan, K. Luo, and K. Cen, "Immersed boundary method for the simulation of flows with heat transfer," *International Journal of Heat and Mass Transfer,* vol. 52, pp. 4510-4518, 2009.

[116] Z. Wang, J. Fan, and K. Luo, "Combined multi-direct forcing and immersed boundary method for simulating flows with moving particles," *International Journal of Multiphase Flow,* vol. 34, pp. 283-302, 2008.

[117] D. Young, Y. Jan, and C. Chiu, "A novel immersed boundary procedure for flow and heat simulations with moving boundary," *Computers & Fluids,* vol. 38, pp. 1145-1159, 2009.

[118] Z.-G. Feng and E. E. Michaelides, "Heat transfer in particulate flows with direct numerical simulation (DNS)," *International Journal of Heat and Mass Transfer,* vol. 52, pp. 777-786, 2009.

[119] B. Kim, D. Lee, M. Ha, and H. Yoon, "A numerical study of natural convection in a square enclosure with a circular cylinder at different vertical locations," *International Journal of Heat and Mass Transfer,* vol. 51, pp. 1888-1906, 2008.

[120] J. Lee, J. Kim, H. Choi, and K.-S. Yang, "Sources of spurious force oscillations from an immersed boundary method for moving-body problems," *Journal of computational physics,* vol. 230, pp. 2677-2695, 2011.

[121] K. Chua, "Fundamental experiments and numerical investigation of cryo-freezing incorporating vascular network with enhanced nano-freezing," *International Journal of Thermal Sciences,* vol. 70, pp. 17-31, 2013.

[122] H. H. Pennes, "Analysis of Tissue and Arterial Blood Temperatures in the Resting Human Forearm," *Journal of Applied Physiology,* vol. 1, pp. 93-122, 1948.

[123] D. Tzou, "A unified field approach for heat conduction from macro-to micro-scales," *Journal of Heat Transfer,* vol. 117, pp. 8-16, 1995.

[124] C. Cattaneo, "Sur une forme de lequation de la chaleur eliminant le paradoxe dune propagation instantanee," *Comptes Rendus Hebdomadaires Des Seances De L Academie Des Sciences,* vol. 247, pp. 431-433, 1958.

[125] P. Vernotte, "Les paradoxes de la théorie continue de l'équation de la chaleur," *Comptes Rendus Hebdomadaires Des Seances De L Academie Des Sciences,* vol. 246, pp. 3154-3155, 1958.

[126] W. Roetzel and Y. Xuan, "Transient response of the human limb to an external stimulust," *International journal of heat and mass transfer,* vol. 41, pp. 229-239, 1998.

[127] L. A. Dombrovsky, N. B. Nenarokomova, D. I. Tsiganov, and Y. A. Zeigarnik, "Modeling of repeating freezing of biological tissues and analysis of possible microwave monitoring of local regions of thawing," *International Journal of Heat and Mass Transfer,* vol. 89, pp. 894-902, 2015.

[128] R. T. Duarte, M. C. Carvalho Simoes, and V. C. Sgarbieri, "Bovine blood components: fractionation, composition, and nutritive value," *J Agric Food Chem,* vol. 47, pp. 231-6, Jan 1999.

[129] D. Biswas and U. S. Chakraborty, "A Brief Review on Blood Flow Modeling in Arteries," *Assam University Journal of Science and Technology,* vol. 6, pp. 10-15, 2010.

[130] Z.-S. Deng, J. Liu, and H.-W. Wang, "Disclosure of the significant thermal effects of large blood vessels during cryosurgery through infrared temperature mapping," *International Journal of Thermal Sciences,* vol. 47, pp. 530-545, 2008.

[131] K. Chua, X. Zhao, and S. Chou, "Effects of crucial parameters on the freezing delivery in the cryosurgical system," *Applied Thermal Engineering,* vol. 51, pp. 734-741, 2013.

[132] J.-F. Yan, Z.-S. Deng, J. Liu, and Y.-X. Zhou, "New modality for maximizing cryosurgical killing scope while minimizing mechanical incision trauma using combined freezing-heating system," *Journal of Medical Devices,* vol. 1, pp. 264-271, 2007.

[133] J. Yu, P. Liang, X. Yu, F. Liu, L. Chen, and Y. Wang, "A comparison of microwave ablation and bipolar radiofrequency ablation both with an internally cooled probe: results in ex vivo and in vivo porcine livers," *European journal of radiology*, vol. 79, pp. 124-130, 2011.

[134] Z.-S. Deng and J. Liu, "Numerical simulation of selective freezing of target biological tissues following injection of solutions with specific thermal properties," *Cryobiology*, vol. 50, pp. 183-192, 2005.

[135] Z. Magalov, A. Shitzer, and D. Degani, "Isothermal volume contours generated in a freezing gel by embedded cryo-needles with applications to cryo-surgery," *Cryobiology*, vol. 55, pp. 127-137, 2007.

[136] J. K. Seifert, T. Achenbach, A. Heintz, T. C. Böttger, and T. Junginger, "Cryotherapy for liver metastases," *International journal of colorectal disease*, vol. 15, pp. 161-166, 2000.

[137] R. S. Okten, F. Kucukay, H. Dedeoglu, M. Akdogan, S. Kacar, B. Bostanci, *et al.*, "Branching patterns of the main portal vein: Effect on estimated remnant liver volume in preoperative evaluation of donors for liver transplantation," *European journal of radiology*, vol. 81, pp. 478-483, 2012.

[138] K. C. Leong, C. Yang, and S. M. S. Murshed, "A model for the thermal conductivity of nanofluids - the effect of interfacial layer," *Journal of Nanoparticle Research*, vol. 8, pp. 245-254, Apr 2006.

[139] S. M. S. Murshed, K. C. Leong, and C. Yang, "Investigations of thermal conductivity and viscosity of nanofluids," *International Journal of Thermal Sciences*, vol. 47, pp. 560-568, May 2008.

[140] R. L. Hamilton and O. K. Crosser, "Thermal Conductivity of Heterogeneous 2-Component Systems," *Industrial & Engineering Chemistry Fundamentals*, vol. 1, pp. 187-&, 1962.

[141] J.-F. Yan and J. Liu, "Nanocryosurgery and its mechanisms for enhancing freezing efficiency of tumor tissues," *Nanomedicine: Nanotechnology, Biology and Medicine*, vol. 4, pp. 79-87, 2008.

[142] S. M. S. Murshed, K. C. Leong, and C. Yang, "A combined model for the effective thermal conductivity of nanofluids," *Applied Thermal Engineering*, vol. 29, pp. 2477-2483, Aug 2009.

[143] F. Yuan, Y. Chi, S. Huang, and J. Liu, "Modeling n-furcated liver vessels from a 3-D segmented volume using hole-making and subdivision methods," *Biomedical Engineering, IEEE Transactions on*, vol. 59, pp. 552-561, 2012.

[144] J. Moore, D. Steinman, D. Holdsworth, and C. Ethier, "Accuracy of computational hemodynamics in complex arterial geometries reconstructed from magnetic resonance imaging," *Annals of biomedical engineering*, vol. 27, pp. 32-41, 1999.

[145] Q. Long, X. Xu, M. Bourne, and T. Griffith, "Numerical study of blood flow in an anatomically realistic aorto‐iliac bifurcation generated from MRI data," *Magnetic Resonance in Medicine*, vol. 43, pp. 565-576, 2000.

[146] K. C. Wang, R. W. Dutton, and C. A. Taylor, "Improving geometric model construction for blood flow modeling," *IEEE Engineering in Medicine and Biology Magazine*, vol. 18, pp. 33-39, 1999.

[147] I. Volkau, W. Zheng, R. Baimouratov, A. Aziz, and W. L. Nowinski, "Geometric modeling of the human normal cerebral arterial system," *IEEE transactions on medical imaging*, vol. 24, pp. 529-539, 2005.

[148] T. F. Sherman, "On connecting large vessels to small. The meaning of Murray's law," *The Journal of general physiology*, vol. 78, pp. 431-453, 1981.

[149] C. D. Murray, "The physiological principle of minimum work I. The vascular system and the cost of blood volume," *Proceedings of the National Academy of Sciences*, vol. 12, pp. 207-214, 1926.

[150] X. Zhao, “Effective treatment of solid tumors via cryosurgery”,2013.

This page has been left blank intentionally.

APPENDIX Experimental Data

Table A(1) The experimental data for the single blood vessel

TC1		TC2		TC3		Cryoprobe	
102(Seconds)	102(C)	103(Seconds)	103(C)	104(Seconds)	104(C)	106(Seconds)	106(C)
0.018	37.3	0.063	37.5	0.109	37.4	0.155	37.2
10.002	37.5	10.048	37.7	10.094	37.6	10.139	37.0
20.048	37.4	20.094	37.6	20.14	37.5	20.185	28.7
30.017	37.4	30.063	37.6	30.109	37.6	30.154	19.2
40.002	37.4	40.048	37.7	40.094	37.6	40.14	10.6
50.047	37.2	50.095	37.6	50.14	37.6	50.186	2.4
60.02	37.0	60.065	37.6	60.111	37.5	60.157	-5.5
70.053	36.6	70.099	37.5	70.144	37.5	70.19	-12.7
80.029	36.1	80.074	37.5	80.12	37.4	80.166	-19.5
90.006	35.5	90.052	37.4	90.098	37.4	90.143	-25.0
100.04	34.9	100.085	37.3	100.131	37.4	100.177	-33.9
110.012	34.2	110.058	37.2	110.104	37.4	110.149	-39.4
120.04	33.4	120.086	37.1	120.132	37.4	120.177	-46.3
130.013	32.3	130.058	36.9	130.104	37.4	130.15	-53.5
140.043	31.1	140.089	36.7	140.134	37.3	140.18	-60.2
150.019	29.7	150.065	36.5	150.111	37.3	150.156	-66.2
160.002	28.0	160.048	36.1	160.094	37.2	160.139	-73.5
170.031	26.2	170.076	35.8	170.122	37.2	170.168	-78.7
180.003	24.3	180.049	35.3	180.095	37.1	180.141	-85.2
190.033	22.1	190.079	34.9	190.125	37.0	190.17	-92.0
200.002	19.8	200.05	34.3	200.096	36.9	200.142	-98.4
210.037	17.4	210.083	33.7	210.128	36.8	210.174	-108.4
220.008	14.6	220.054	33.1	220.1	36.7	220.146	-107.2
230.041	11.3	230.087	32.4	230.132	36.6	230.178	-107.3
240.024	8.1	240.069	31.6	240.115	36.4	240.161	-109.9
250.002	4.6	250.048	30.7	250.094	36.3	250.139	-148.9
260.038	-0.6	260.083	29.8	260.129	36.1	260.175	-150.1
270.016	-5.2	270.062	28.8	270.108	35.9	270.153	-150.4
280.044	-7.8	280.09	27.6	280.136	35.7	280.181	-151.2
290.02	-9.8	290.066	26.4	290.112	35.4	290.157	-152.1
300.013	-11.6	300.058	25.1	300.104	35.1	300.15	-152.0
310.044	-13.2	310.09	23.8	310.135	34.9	310.181	-152.5
320.023	-14.7	320.069	22.5	320.115	34.6	320.16	-153.4
330.002	-16.2	330.05	21.1	330.096	34.2	330.142	-153.7
340.037	-17.7	340.083	19.6	340.129	33.8	340.174	-153.5
350.013	-19.0	350.059	18.1	350.105	33.5	350.15	-154.3

360.039	-20.2	360.084	16.5	360.13	33.0	360.176	-155.1
370.014	-21.4	370.06	14.9	370.106	32.5	370.151	-154.7
380.044	-22.5	380.089	13.4	380.135	32.0	380.181	-155.0
390.018	-23.5	390.064	11.8	390.109	31.5	390.155	-155.8
400.051	-24.4	400.097	10.2	400.142	31.0	400.188	-155.5
410.051	-25.4	410.097	8.6	410.143	30.4	410.188	-155.5
420.021	-26.2	420.066	7.0	420.112	29.9	420.158	-156.5
430.051	-27.0	430.099	5.4	430.145	29.3	430.191	-156.0
440.038	-27.7	440.084	3.8	440.129	28.8	440.175	-156.4
450.015	-28.5	450.061	2.2	450.107	28.2	450.152	-157.0
460.052	-29.2	460.098	0.5	460.143	27.5	460.189	-156.8
470.032	-29.9	470.078	-1.0	470.124	26.9	470.169	-156.8
480.012	-30.6	480.058	-2.4	480.103	26.2	480.149	-157.4
490.052	-31.2	490.098	-3.7	490.144	25.6	490.19	-157.1
500.03	-31.8	500.075	-4.8	500.121	24.9	500.167	-157.8
510.008	-32.4	510.053	-5.8	510.099	24.3	510.145	-157.4
520.037	-33.0	520.083	-6.7	520.128	23.6	520.174	-158.2
530.018	-33.6	530.063	-7.4	530.109	23.0	530.155	-157.4
540.002	-34.1	540.048	-8.1	540.094	22.3	540.139	-158.3
550.043	-34.6	550.089	-8.7	550.134	21.7	550.18	-157.7
560.016	-35.0	560.062	-9.2	560.109	21.1	560.155	-158.6
570.047	-35.5	570.095	-9.7	570.141	20.5	570.187	-157.8
580.021	-35.9	580.067	-10.2	580.112	19.9	580.158	-158.6
590.049	-36.4	590.095	-10.7	590.141	19.3	590.187	-158.0
600.016	-36.8	600.062	-11.2	600.108	18.6	600.154	-158.9
610.048	-37.2	610.094	-11.7	610.141	18.0	610.187	-158.3
620.023	-37.6	620.068	-12.1	620.115	17.3	620.161	-158.7
630.05	-38.0	630.096	-12.6	630.141	16.7	630.187	-158.5
640.021	-38.4	640.067	-13.0	640.112	16.1	640.158	-158.5
650.002	-38.8	650.05	-13.4	650.096	15.5	650.142	-159.2
660.033	-39.1	660.079	-13.8	660.125	14.8	660.17	-158.6
670.013	-39.5	670.06	-14.2	670.105	14.1	670.151	-159.4
680.053	-39.9	680.099	-14.7	680.145	13.5	680.19	-158.7
690.028	-40.2	690.074	-15.1	690.119	12.9	690.165	-159.6
700.004	-40.5	700.05	-15.5	700.096	12.2	700.141	-159.1
710.037	-40.8	710.083	-15.8	710.129	11.6	710.174	-159.6
720.016	-41.1	720.062	-16.1	720.107	11.0	720.153	-159.3
730.054	-41.3	730.1	-16.4	730.146	10.5	730.191	-159.4
740.034	-41.6	740.08	-16.7	740.125	9.9	740.171	-159.7
750.01	-41.9	750.056	-17.1	750.102	9.2	750.148	-159.1
760.044	-42.2	760.09	-17.4	760.135	8.6	760.181	-160.1
770.013	-42.4	770.058	-17.7	770.104	8.0	770.15	-159.3
780.049	-42.7	780.094	-18.1	780.14	7.4	780.186	-160.1
790.031	-43.0	790.076	-18.4	790.122	6.8	790.167	-159.4
800.002	-43.3	800.05	-18.7	800.096	6.2	800.141	-159.9

810.041	-43.5	810.086	-19.0	810.132	5.6	810.178	-160.0
820.021	-43.8	820.067	-19.3	820.112	5.0	820.158	-159.8
830.051	-44.0	830.096	-19.6	830.142	4.4	830.188	-160.4
840.029	-44.2	840.075	-19.9	840.121	3.8	840.166	-159.7
850.01	-44.5	850.056	-20.2	850.102	3.2	850.147	-160.4
860.052	-44.7	860.097	-20.4	860.143	2.6	860.189	-159.8
870.024	-44.9	870.069	-20.7	870.115	2.0	870.161	-160.4
880.002	-45.1	880.048	-21.0	880.094	1.4	880.14	-159.9
890.038	-45.4	890.083	-21.2	890.129	0.9	890.175	-160.6
900.03	-45.5	900.076	-21.5	900.121	0.3	900.167	-160.0
910.016	-45.7	910.063	-21.6	910.109	-0.2	910.154	-160.7
920.007	-45.9	920.052	-21.9	920.098	-0.7	920.144	-160.0
930.049	-46.1	930.094	-22.1	930.14	-1.3	930.185	-160.8
940.03	-46.3	940.076	-22.3	940.122	-1.8	940.167	-160.4
950.017	-46.5	950.063	-22.6	950.108	-2.3	950.154	-160.8
960.003	-46.7	960.049	-22.8	960.095	-2.9	960.14	-160.3
970.037	-46.9	970.082	-23.1	970.128	-3.4	970.174	-161.0
980.017	-47.1	980.063	-23.3	980.109	-3.8	980.155	-160.3
990.005	-47.3	990.051	-23.5	990.096	-4.3	990.142	-160.7
1000.049	-47.4	1000.095	-23.7	1000.141	-4.8	1000.187	-160.9
1010.035	-47.6	1010.083	-23.9	1010.129	-5.2	1010.175	-160.4
1020.016	-47.8	1020.062	-24.1	1020.109	-5.6	1020.155	-161.2
1030.004	-47.9	1030.05	-24.3	1030.096	-6.0	1030.141	-160.5
1040.051	-48.1	1040.097	-24.5	1040.143	-6.4	1040.188	-161.1
1050.031	-48.3	1050.077	-24.7	1050.122	-6.8	1050.168	-160.8
1060.016	-48.4	1060.064	-24.9	1060.11	-7.1	1060.156	-160.6
1070.05	-48.6	1070.096	-25.1	1070.142	-7.5	1070.187	-161.1
1080.013	-48.7	1080.059	-25.3	1080.105	-7.7	1080.151	-160.7
1090.053	-48.9	1090.099	-25.5	1090.144	-8.1	1090.19	-161.0
1100.025	-49.0	1100.07	-25.7	1100.116	-8.3	1100.161	-161.1
1110.002	-49.2	1110.048	-25.9	1110.094	-8.6	1110.139	-160.7
1120.031	-49.4	1120.077	-26.0	1120.122	-8.8	1120.168	-161.5
1130.017	-49.5	1130.063	-26.3	1130.109	-9.1	1130.154	-160.7
1140.002	-49.7	1140.048	-26.4	1140.094	-9.3	1140.139	-161.3
1150.043	-49.8	1150.089	-26.6	1150.134	-9.5	1150.18	-160.8
1160.033	-49.9	1160.079	-26.7	1160.124	-9.7	1160.17	-160.8
1170.022	-50.0	1170.067	-26.9	1170.113	-9.8	1170.158	-161.6
1180.002	-50.1	1180.048	-27.0	1180.094	-10.0	1180.139	-160.8
1190.038	-50.2	1190.084	-27.2	1190.13	-10.3	1190.176	-161.4
1200.02	-50.4	1200.066	-27.3	1200.111	-10.4	1200.157	-161.4

Table A(2) The experimental data for the parallel counter-current vessel pair

TC1		TC2		Cryoprobe	
101(Seconds)	101(C)	102(Seconds)	102(C)	106(Seconds)	106(C)
0.018	37.5	0.064	37.9	0.109	37.2
10.005	37.6	10.052	38.0	10.097	25.7
20.002	37.1	20.048	37.9	20.094	15.2
30.053	36.1	30.098	37.9	30.144	7.3
40.034	34.8	40.08	37.6	40.126	2.7
50.027	33.4	50.072	37.4	50.118	-3.1
60.033	31.9	60.078	37.0	60.124	-6.5
70.02	30.4	70.065	36.5	70.112	-11.8
80.007	28.9	80.052	36.0	80.1	-16.6
90.053	27.1	90.1	35.4	90.146	-21.8
100.043	25.0	100.091	34.8	100.136	-27.9
110.033	22.5	110.079	34.0	110.125	-33.9
120.022	19.7	120.067	33.2	120.113	-39.8
130.005	16.4	130.051	32.2	130.099	-46.4
140.045	12.6	140.091	31.0	140.137	-52.5
150.047	7.8	150.093	29.7	150.139	-58.9
160.046	2.2	160.091	28.3	160.137	-65.4
170.041	-1.0	170.087	26.6	170.135	-71.1
180.04	-3.2	180.086	25.1	180.132	-78.7
190.038	-6.0	190.084	23.4	190.13	-98.4
200.04	-9.9	200.086	21.4	200.132	-112.8
210.039	-14.0	210.084	19.1	210.13	-114.9
220.029	-20.5	220.075	16.3	220.121	-150.2
230.025	-25.5	230.073	12.2	230.118	-148.3
240.015	-29.0	240.061	6.8	240.107	-152.4
250.002	-31.1	250.048	1.3	250.094	-147.7
260.047	-27.1	260.093	-1.0	260.138	-105.0
270.029	-26.1	270.075	-1.8	270.121	-103.8
280.028	-34.8	280.073	-3.3	280.119	-153.9
290.018	-39.6	290.064	-5.6	290.109	-155.1
300.01	-41.9	300.056	-7.6	300.102	-155.6
310.005	-43.7	310.05	-9.6	310.096	-155.7
320.002	-45.2	320.048	-11.3	320.094	-156.1
330.047	-46.6	330.092	-12.9	330.138	-156.5
340.04	-47.9	340.086	-14.5	340.132	-156.6
350.025	-49.0	350.07	-15.9	350.116	-156.9
360.021	-50.1	360.069	-17.2	360.115	-156.9
370.011	-51.0	370.057	-18.4	370.103	-157.4
380.002	-51.9	380.048	-19.5	380.094	-157.2

390.043	-52.8	390.088	-20.6	390.134	-157.0
400.033	-53.6	400.079	-21.7	400.124	-157.4
410.027	-54.4	410.073	-22.8	410.119	-157.2
420.016	-55.2	420.062	-23.8	420.107	-157.7
430.052	-55.9	430.098	-24.8	430.144	-158.1
440.043	-56.6	440.091	-25.8	440.137	-157.9
450.038	-57.2	450.086	-26.6	450.131	-158.0
460.03	-57.8	460.076	-27.4	460.121	-158.2
470.024	-58.4	470.07	-28.2	470.116	-158.2
480.022	-59.0	480.068	-28.9	480.114	-158.5
490.015	-59.4	490.06	-29.6	490.106	-158.0
500.007	-60.0	500.053	-30.3	500.098	-157.7
510.048	-60.4	510.094	-30.9	510.14	-157.7
520.039	-60.9	520.086	-31.6	520.132	-157.7
530.029	-61.4	530.075	-32.2	530.12	-158.2
540.017	-61.8	540.063	-32.7	540.109	-158.2
550.015	-62.3	550.061	-33.3	550.107	-158.3
560.008	-62.7	560.053	-33.8	560.099	-158.3
570.004	-63.0	570.05	-34.3	570.095	-158.1
580.051	-63.5	580.097	-34.8	580.142	-158.2
590.041	-63.8	590.087	-35.3	590.133	-158.1
600.026	-64.1	600.072	-35.7	600.117	-158.6
610.012	-64.5	610.058	-36.1	610.104	-158.8
620.003	-64.9	620.048	-36.6	620.094	-159.1
630.047	-65.2	630.092	-37.0	630.14	-159.1
640.036	-65.5	640.082	-37.4	640.128	-158.7
650.029	-65.7	650.074	-37.7	650.12	-158.7
660.013	-66.0	660.059	-38.1	660.104	-158.8
670.007	-66.3	670.053	-38.4	670.099	-158.5
680.002	-66.6	680.05	-38.8	680.096	-158.5
690.051	-66.8	690.096	-39.1	690.142	-158.6
700.053	-67.1	700.099	-39.5	700.145	-159.1
710.033	-67.4	710.079	-39.8	710.125	-159.1
720.027	-67.6	720.073	-40.1	720.119	-158.7
730.014	-67.8	730.06	-40.4	730.105	-158.8
740.002	-68.0	740.049	-40.7	740.096	-158.7
750.043	-68.2	750.091	-41.0	750.137	-159.5
760.038	-68.5	760.083	-41.3	760.129	-159.0
770.034	-68.7	770.08	-41.6	770.125	-159.2
780.034	-68.9	780.082	-41.8	780.128	-158.9
790.021	-69.1	790.067	-42.1	790.115	-158.7
800.012	-69.3	800.057	-42.3	800.105	-159.0
810.002	-69.5	810.048	-42.5	810.094	-159.3
820.046	-69.7	820.092	-42.8	820.137	-158.8
830.035	-69.9	830.081	-43.0	830.127	-159.7

840.027	-70.1	840.073	-43.3	840.118	-159.1
850.016	-70.2	850.062	-43.5	850.11	-158.8
860.01	-70.4	860.056	-43.7	860.104	-159.0
870.012	-70.6	870.057	-43.9	870.103	-159.6
880.003	-70.7	880.048	-44.1	880.096	-159.0
890.049	-70.9	890.095	-44.3	890.141	-159.2
900.051	-71.0	900.097	-44.6	900.143	-159.3
910.032	-71.2	910.08	-44.7	910.125	-159.1
920.02	-71.4	920.066	-45.0	920.112	-159.1
930.011	-71.6	930.056	-45.1	930.102	-159.0
940.002	-71.7	940.048	-45.3	940.094	-159.3
950.007	-71.8	950.054	-45.5	950.099	-159.8
960.05	-71.9	960.096	-45.7	960.141	-159.3
970.042	-72.1	970.088	-45.9	970.134	-159.5
980.029	-72.2	980.075	-46.1	980.121	-159.4
990.015	-72.3	990.061	-46.2	990.107	-159.1
1000.002	-72.4	1000.048	-46.4	1000.094	-159.3
1010.043	-72.6	1010.088	-46.5	1010.134	-159.5
1020.027	-72.7	1020.073	-46.7	1020.119	-159.1
1030.011	-72.8	1030.056	-46.9	1030.102	-159.7
1040.002	-72.9	1040.048	-47.0	1040.095	-159.5
1050.002	-73.0	1050.048	-47.2	1050.095	-159.4
1060.002	-73.2	1060.048	-47.3	1060.094	-159.6
1070.05	-73.3	1070.095	-47.5	1070.141	-159.3
1080.042	-73.4	1080.088	-47.6	1080.134	-159.4
1090.033	-73.5	1090.079	-47.8	1090.124	-159.7
1100.017	-73.6	1100.063	-48.0	1100.109	-159.5
1110.003	-73.7	1110.049	-48.1	1110.094	-159.1
1120.047	-73.8	1120.093	-48.2	1120.139	-159.8
1130.05	-73.9	1130.096	-48.4	1130.142	-159.3
1140.034	-74.0	1140.08	-48.5	1140.126	-160.1
1150.017	-74.1	1150.063	-48.7	1150.109	-159.6
1160.014	-74.3	1160.059	-48.8	1160.105	-159.2
1170.002	-74.4	1170.048	-48.9	1170.094	-160.2
1180.055	-74.5	1180.1	-49.1	1180.146	-159.4
1190.038	-74.6	1190.084	-49.2	1190.13	-159.6
1200.025	-74.6	1200.07	-49.3	1200.116	-159.3

Table A(3) The experimental data for the case with flow rate of 80 ml/min

TC1		TC2		TC3		Cryoprobe	
102(Seconds)	102(C)	103(Seconds)	103(C)	104(Seconds)	104(C)	106(Seconds)	106(C)
0.064	37.6	0.109	37.8	0.155	37.7	0.246	37.5
10.076	37.4	10.122	37.6	10.167	37.5	10.259	16.8
20.086	37.1	20.132	37.4	20.177	37.2	20.269	-13.5
30.098	36.4	30.144	37.0	30.189	37.0	30.281	-24.4
40.048	35.3	40.094	36.4	40.14	36.7	40.231	-34.1
50.056	33.8	50.103	35.7	50.149	36.4	50.24	-47.7
60.061	32.1	60.107	34.8	60.153	36.0	60.244	-53.7
70.064	30.1	70.11	33.8	70.155	35.7	70.247	-63.0
80.068	27.9	80.114	32.6	80.16	35.3	80.252	-71.1
90.082	25.5	90.128	31.3	90.174	34.8	90.265	-78.1
100.091	23.1	100.138	29.9	100.185	34.2	100.276	-92.5
110.048	20.4	110.094	28.4	110.14	33.7	110.231	-118.5
120.056	17.1	120.102	26.8	120.147	33.1	120.239	-105.9
130.06	13.6	130.106	24.9	130.151	32.4	130.244	-102.0
140.075	10.1	140.121	22.9	140.166	31.7	140.258	-102.8
150.084	6.7	150.13	20.8	150.176	30.9	150.268	-143.9
160.098	2.5	160.144	18.7	160.189	30.1	160.28	-144.2
170.057	-0.6	170.102	16.6	170.148	29.4	170.24	-144.8
180.063	-3.2	180.109	14.4	180.154	28.5	180.246	-145.4
190.079	-5.5	190.125	12.0	190.171	27.7	190.262	-145.0
200.095	-7.6	200.14	9.5	200.186	26.7	200.277	-145.5
210.048	-9.5	210.094	6.9	210.139	25.8	210.232	-145.6
220.055	-11.3	220.101	4.3	220.147	24.8	220.238	-145.7
230.063	-12.9	230.109	1.9	230.155	23.7	230.246	-145.8
240.067	-14.5	240.113	0.1	240.159	22.6	240.25	-146.0
250.082	-15.9	250.128	-1.4	250.173	21.5	250.265	-145.9
260.099	-17.2	260.145	-2.7	260.191	20.4	260.282	-146.4
270.048	-18.4	270.094	-4.0	270.139	19.2	270.231	-146.2
280.056	-19.6	280.102	-5.3	280.148	18.1	280.239	-146.5
290.058	-20.7	290.104	-6.4	290.149	17.1	290.241	-146.2
300.062	-21.7	300.108	-7.5	300.154	16.0	300.246	-146.6
310.072	-22.6	310.118	-8.5	310.164	14.9	310.255	-146.5
320.088	-23.5	320.134	-9.6	320.179	13.8	320.271	-147.1
330.094	-24.4	330.14	-10.5	330.185	12.7	330.276	-146.7
340.098	-25.2	340.144	-11.4	340.189	11.6	340.281	-146.9
350.048	-26.0	350.094	-12.2	350.139	10.5	350.231	-146.9
360.055	-26.7	360.101	-13.0	360.147	9.3	360.238	-146.3
370.053	-27.5	370.099	-13.8	370.144	8.2	370.236	-146.8
380.066	-28.1	380.112	-14.5	380.157	7.1	380.249	-147.0

390.077	-28.7	390.123	-15.2	390.168	6.1	390.261	-147.1
400.081	-29.3	400.127	-15.9	400.172	5.0	400.264	-146.8
410.048	-29.9	410.094	-16.5	410.139	3.9	410.231	-147.2
420.06	-30.4	420.106	-17.1	420.151	2.9	420.243	-147.5
430.078	-30.9	430.123	-17.7	430.169	2.0	430.26	-147.3
440.097	-31.5	440.143	-18.3	440.189	1.1	440.28	-147.1
450.071	-32.0	450.118	-18.8	450.163	0.2	450.255	-147.1
460.081	-32.4	460.126	-19.3	460.172	-0.6	460.264	-147.3
470.09	-32.8	470.136	-19.8	470.181	-1.2	470.273	-147.5
480.049	-33.3	480.095	-20.3	480.14	-1.8	480.232	-147.4
490.067	-33.7	490.113	-20.7	490.159	-2.4	490.25	-147.2
500.082	-34.1	500.128	-21.1	500.174	-2.9	500.266	-147.1
510.094	-34.4	510.14	-21.6	510.185	-3.4	510.277	-147.8
520.048	-34.8	520.094	-22.0	520.139	-3.9	520.231	-147.7
530.063	-35.2	530.109	-22.5	530.155	-4.4	530.246	-147.5
540.087	-35.7	540.133	-22.9	540.179	-4.9	540.27	-147.8
550.099	-36.0	550.145	-23.3	550.19	-5.3	550.282	-147.2
560.052	-36.4	560.097	-23.7	560.143	-5.8	560.234	-147.9
570.056	-36.7	570.102	-24.1	570.147	-6.2	570.239	-148.1
580.073	-37.0	580.118	-24.4	580.164	-6.6	580.256	-147.9
590.086	-37.3	590.132	-24.7	590.178	-7.1	590.269	-147.9
600.049	-37.6	600.094	-25.1	600.14	-7.4	600.231	-147.5
610.072	-37.9	610.118	-25.4	610.163	-7.8	610.255	-147.5
620.09	-38.1	620.135	-25.6	620.181	-8.2	620.272	-147.6
630.1	-38.4	630.145	-26.0	630.191	-8.6	630.283	-147.6
640.073	-38.7	640.119	-26.3	640.164	-9.0	640.256	-147.9
650.098	-39.0	650.143	-26.6	650.189	-9.3	650.281	-147.9
660.048	-39.2	660.094	-26.9	660.139	-9.7	660.231	-147.9
670.061	-39.5	670.107	-27.2	670.152	-10.1	670.244	-147.8
680.079	-39.7	680.124	-27.4	680.17	-10.3	680.261	-147.8
690.048	-40.0	690.094	-27.7	690.139	-10.7	690.231	-148.4
700.06	-40.2	700.105	-28.0	700.151	-11.0	700.242	-147.8
710.078	-40.4	710.123	-28.2	710.17	-11.3	710.261	-147.7
720.091	-40.7	720.137	-28.5	720.182	-11.6	720.274	-147.6
730.05	-40.9	730.096	-28.8	730.141	-11.9	730.233	-148.3
740.066	-41.2	740.112	-29.1	740.157	-12.3	740.249	-148.3
750.088	-41.3	750.134	-29.3	750.18	-12.6	750.271	-148.1
760.05	-41.5	760.096	-29.5	760.142	-12.8	760.233	-148.0
770.068	-41.7	770.114	-29.8	770.16	-13.1	770.251	-147.9
780.076	-42.0	780.122	-30.0	780.168	-13.4	780.259	-148.0
790.1	-42.1	790.145	-30.2	790.191	-13.7	790.282	-148.1
800.056	-42.3	800.102	-30.4	800.147	-13.9	800.239	-148.1
810.072	-42.5	810.117	-30.6	810.163	-14.2	810.255	-148.3
820.095	-42.7	820.141	-30.7	820.186	-14.3	820.278	-148.2
830.053	-42.8	830.099	-30.9	830.145	-14.6	830.236	-147.9

840.065	-43.0	840.111	-31.2	840.156	-14.8	840.248	-147.7
850.073	-43.2	850.119	-31.3	850.164	-15.1	850.257	-148.0
860.081	-43.4	860.127	-31.5	860.172	-15.3	860.264	-148.2
870.091	-43.5	870.137	-31.7	870.182	-15.5	870.274	-147.9
880.058	-43.6	880.104	-31.8	880.15	-15.7	880.241	-147.8
890.07	-43.8	890.116	-32.0	890.162	-15.9	890.253	-147.9
900.081	-44.0	900.126	-32.2	900.172	-16.1	900.264	-148.1
910.093	-44.1	910.139	-32.4	910.184	-16.3	910.276	-147.9
920.056	-44.3	920.102	-32.5	920.148	-16.5	920.24	-148.3
930.061	-44.4	930.107	-32.7	930.152	-16.7	930.244	-148.7
940.068	-44.5	940.114	-32.8	940.16	-16.9	940.251	-148.4
950.088	-44.7	950.133	-33.0	950.179	-17.1	950.27	-148.3
960.048	-44.9	960.094	-33.2	960.14	-17.3	960.231	-148.5
970.062	-45.0	970.108	-33.3	970.153	-17.5	970.245	-148.3
980.075	-45.1	980.122	-33.4	980.168	-17.7	980.259	-148.3
990.085	-45.2	990.131	-33.6	990.177	-17.8	990.268	-148.3
1000.095	-45.3	1000.14	-33.7	1000.186	-18.0	1000.278	-148.3
1010.048	-45.5	1010.094	-33.9	1010.139	-18.2	1010.231	-148.3
1020.062	-45.6	1020.107	-34.0	1020.153	-18.3	1020.244	-148.4
1030.072	-45.8	1030.118	-34.2	1030.163	-18.5	1030.255	-148.2
1040.081	-45.9	1040.127	-34.3	1040.173	-18.7	1040.264	-148.4
1050.097	-46.0	1050.143	-34.4	1050.188	-18.8	1050.28	-148.4
1060.056	-46.1	1060.102	-34.6	1060.148	-19.0	1060.239	-148.6
1070.075	-46.2	1070.121	-34.7	1070.166	-19.1	1070.258	-148.7
1080.088	-46.3	1080.134	-34.8	1080.18	-19.3	1080.271	-148.4
1090.048	-46.4	1090.094	-34.8	1090.139	-19.4	1090.231	-148.3
1100.061	-46.5	1100.106	-34.9	1100.152	-19.5	1100.243	-148.2
1110.073	-46.6	1110.118	-35.1	1110.164	-19.7	1110.255	-148.5
1120.093	-46.7	1120.139	-35.3	1120.185	-19.9	1120.276	-148.6
1130.048	-46.9	1130.094	-35.4	1130.14	-20.0	1130.231	-148.6
1140.07	-47.0	1140.116	-35.6	1140.161	-20.2	1140.253	-148.6
1150.083	-47.1	1150.128	-35.7	1150.174	-20.3	1150.265	-148.3
1160.097	-47.1	1160.143	-35.7	1160.188	-20.4	1160.28	-148.3
1170.048	-47.2	1170.094	-35.9	1170.14	-20.5	1170.231	-148.2
1180.062	-47.3	1180.108	-35.9	1180.154	-20.7	1180.246	-148.2

Table A(4) The experimental data for the case with flow rate of 100 ml/min

TC1		TC2		TC3		Cryoprobe	
102(Seconds)	102(C)	103(Seconds)	103(C)	104(Seconds)	104(C)	106(Seconds)	106(C)
0.063	37.9	0.109	37.2	0.155	37.4	0.246	37.7
10.071	37.7	10.117	37.0	10.163	37.2	10.254	37.6
20.088	37.6	20.133	36.9	20.179	37.1	20.27	8.6
30.096	37.1	30.141	36.7	30.187	37.0	30.278	-10.6
40.048	36.2	40.094	36.4	40.139	36.8	40.231	-20.5
50.059	35.0	50.104	36.0	50.15	36.5	50.242	-31.5
60.068	33.4	60.113	35.4	60.159	36.1	60.251	-40.9
70.084	31.7	70.13	34.8	70.176	35.8	70.268	-52.7
80.096	29.8	80.142	34.1	80.188	35.5	80.279	-59.7
90.1	27.6	90.146	33.1	90.192	34.9	90.284	-69.8
100.051	25.3	100.096	32.1	100.142	34.3	100.234	-77.2
110.051	23.0	110.097	31.2	110.142	34.0	110.234	-86.9
120.057	20.7	120.103	30.2	120.148	33.5	120.24	-99.0
130.069	17.8	130.114	29.1	130.16	32.9	130.252	-146.5
140.077	13.3	140.122	27.5	140.168	32.0	140.26	-135.9
150.089	8.1	150.135	26.2	150.18	31.6	150.272	-144.0
160.048	3.3	160.094	24.2	160.139	30.5	160.231	-148.7
170.05	0.5	170.095	22.1	170.141	29.5	170.232	-126.5
180.048	-1.6	180.094	20.1	180.139	28.6	180.231	-120.0
190.048	-3.6	190.094	18.2	190.139	27.7	190.231	-149.4
200.048	-6.1	200.094	16.3	200.14	26.9	200.231	-149.9
210.062	-8.1	210.108	14.4	210.153	26.1	210.245	-150.5
220.066	-9.9	220.112	12.2	220.157	25.1	220.249	-150.3
230.066	-11.6	230.112	9.8	230.158	24.0	230.25	-150.3
240.072	-13.1	240.118	7.4	240.164	22.8	240.255	-149.9
250.081	-14.5	250.127	5.1	250.172	21.6	250.264	-149.8
260.084	-15.6	260.13	3.2	260.175	20.7	260.267	-150.2
270.091	-16.6	270.136	1.7	270.182	19.6	270.274	-150.4
280.048	-17.8	280.094	0.6	280.139	18.6	280.231	-150.1
290.057	-18.7	290.103	-0.4	290.149	17.6	290.24	-151.0
300.069	-19.1	300.115	-1.2	300.161	16.9	300.252	-150.2
310.087	-20.0	310.132	-2.0	310.178	16.0	310.269	-150.7
320.048	-20.9	320.094	-2.9	320.139	15.0	320.231	-150.7
330.058	-21.6	330.103	-3.7	330.149	14.1	330.24	-150.7
340.062	-22.5	340.107	-4.5	340.153	13.0	340.245	-150.9
350.077	-23.2	350.123	-5.3	350.169	12.0	350.26	-150.7
360.085	-23.7	360.131	-5.9	360.177	11.1	360.268	-151.0
370.098	-24.4	370.143	-6.7	370.189	10.0	370.28	-150.7
380.052	-25.1	380.098	-7.4	380.144	9.0	380.235	-151.3

390.058	-25.6	390.104	-7.9	390.15	8.0	390.241	-150.7
400.064	-26.0	400.11	-8.5	400.156	7.1	400.248	-151.2
410.082	-26.6	410.128	-9.1	410.173	6.1	410.265	-150.8
420.092	-27.0	420.137	-9.6	420.183	5.2	420.274	-151.5
430.057	-27.4	430.103	-10.0	430.149	4.4	430.241	-150.9
440.061	-27.3	440.107	-10.2	440.152	3.8	440.244	-151.3
450.067	-28.0	450.113	-10.8	450.158	3.0	450.25	-151.2
460.073	-28.5	460.118	-11.3	460.164	2.4	460.256	-151.3
470.079	-28.8	470.125	-11.7	470.17	1.9	470.262	-151.4
480.097	-29.3	480.142	-12.2	480.188	1.5	480.279	-151.1
490.05	-29.6	490.096	-12.6	490.141	1.2	490.232	-151.6
500.07	-29.9	500.115	-12.9	500.161	0.7	500.252	-151.2
510.081	-30.3	510.127	-13.4	510.173	0.4	510.264	-151.4
520.093	-30.6	520.139	-13.7	520.184	0.0	520.276	-151.8
530.056	-30.9	530.102	-14.0	530.148	-0.4	530.239	-151.2
540.068	-31.2	540.114	-14.4	540.159	-0.8	540.251	-151.4
550.089	-31.5	550.134	-14.8	550.18	-1.1	550.272	-151.4
560.053	-31.9	560.098	-15.2	560.144	-1.5	560.235	-151.5
570.064	-32.2	570.109	-15.5	570.155	-1.9	570.246	-151.8
580.078	-32.2	580.124	-15.6	580.17	-2.1	580.261	-151.2
590.098	-32.3	590.144	-15.8	590.189	-2.4	590.28	-151.5
600.048	-32.6	600.094	-16.1	600.139	-2.7	600.231	-151.9
610.062	-32.5	610.107	-16.1	610.153	-2.8	610.244	-151.5
620.072	-33.0	620.117	-16.6	620.163	-3.2	620.255	-151.3
630.083	-33.4	630.129	-17.0	630.174	-3.6	630.266	-151.5
640.097	-33.9	640.143	-17.5	640.188	-4.1	640.28	-151.8
650.049	-34.2	650.094	-17.8	650.14	-4.3	650.232	-151.8
660.05	-34.4	660.096	-18.1	660.142	-4.6	660.234	-151.4
670.058	-34.4	670.104	-18.1	670.149	-4.7	670.241	-151.4
680.063	-34.5	680.109	-18.2	680.154	-4.9	680.246	-151.7
690.071	-34.8	690.116	-18.5	690.162	-5.2	690.254	-151.7
700.072	-35.1	700.118	-18.8	700.163	-5.5	700.255	-151.9
710.086	-35.3	710.132	-19.1	710.177	-5.7	710.269	-151.9
720.051	-35.3	720.097	-19.1	720.142	-5.9	720.234	-151.9
730.071	-35.4	730.116	-19.3	730.162	-6.1	730.254	-151.7
740.096	-35.6	740.142	-19.5	740.188	-6.3	740.279	-151.6
750.053	-35.7	750.099	-19.7	750.145	-6.5	750.236	-151.5
760.064	-35.9	760.11	-19.9	760.156	-6.7	760.247	-151.5
770.095	-36.2	770.141	-20.2	770.186	-7.0	770.279	-151.9
780.052	-36.5	780.098	-20.5	780.144	-7.3	780.236	-151.8
790.062	-36.7	790.108	-20.7	790.154	-7.5	790.246	-151.8
800.08	-37.0	800.126	-21.0	800.172	-7.8	800.263	-152.0
810.048	-37.2	810.094	-21.3	810.139	-8.1	810.231	-152.0
820.056	-37.3	820.102	-21.4	820.148	-8.2	820.239	-152.4
830.068	-37.5	830.113	-21.6	830.159	-8.4	830.251	-152.4

840.094	-37.6	840.139	-21.7	840.185	-8.6	840.277	-152.2
850.054	-37.7	850.099	-21.8	850.145	-8.8	850.236	-152.0
860.076	-37.9	860.122	-22.1	860.167	-9.0	860.259	-152.0
870.094	-37.9	870.139	-22.2	870.185	-9.1	870.276	-151.7
880.057	-37.5	880.103	-21.9	880.148	-9.0	880.24	-151.7
890.083	-37.8	890.129	-22.2	890.175	-9.2	890.267	-151.7
900.098	-38.1	900.144	-22.4	900.189	-9.4	900.281	-151.9
910.067	-38.3	910.112	-22.6	910.158	-9.7	910.25	-152.4
920.087	-38.5	920.132	-22.9	920.178	-9.9	920.27	-152.0
930.048	-38.8	930.094	-23.1	930.139	-10.2	930.231	-152.4
940.059	-39.0	940.105	-23.4	940.151	-10.5	940.242	-152.0
950.071	-39.3	950.117	-23.7	950.162	-10.8	950.254	-151.7
960.082	-39.4	960.127	-23.8	960.173	-10.9	960.264	-151.9
970.097	-39.7	970.142	-24.1	970.188	-11.2	970.279	-152.0
980.056	-39.8	980.102	-24.2	980.147	-11.3	980.239	-152.2
990.064	-39.9	990.11	-24.4	990.155	-11.5	990.248	-152.0
1000.072	-40.1	1000.117	-24.5	1000.163	-11.6	1000.255	-152.7
1010.094	-40.2	1010.139	-24.7	1010.185	-11.8	1010.276	-152.1
1020.048	-40.4	1020.094	-24.9	1020.139	-12.0	1020.231	-152.5
1030.07	-40.5	1030.116	-25.0	1030.162	-12.2	1030.253	-152.6
1040.082	-40.8	1040.128	-25.3	1040.174	-12.4	1040.265	-152.4
1050.092	-40.7	1050.138	-25.3	1050.183	-12.4	1050.275	-152.2
1060.048	-40.7	1060.094	-25.3	1060.14	-12.5	1060.232	-152.4
1070.071	-40.8	1070.116	-25.4	1070.162	-12.6	1070.253	-152.7
1080.077	-41.0	1080.123	-25.6	1080.169	-12.9	1080.26	-152.3
1090.099	-41.1	1090.146	-25.7	1090.192	-12.9	1090.283	-153.1
1100.058	-41.1	1100.104	-25.8	1100.149	-13.0	1100.241	-153.1
1110.069	-41.2	1110.115	-25.8	1110.161	-13.0	1110.252	-153.1
1120.092	-41.2	1120.137	-25.9	1120.183	-13.2	1120.275	-152.3
1130.057	-41.3	1130.104	-26.0	1130.15	-13.3	1130.241	-152.5
1140.076	-41.4	1140.121	-26.2	1140.167	-13.5	1140.258	-152.9
1150.089	-41.6	1150.135	-26.3	1150.181	-13.7	1150.272	-152.3
1160.055	-41.7	1160.1	-26.4	1160.146	-13.8	1160.237	-152.2
1170.074	-41.7	1170.12	-26.5	1170.165	-13.9	1170.257	-152.6
1180.09	-41.8	1180.136	-26.6	1180.181	-14.0	1180.273	-152.4
1190.053	-42.0	1190.099	-26.8	1190.144	-14.2	1190.236	-152.4

Table A(4) The experimental data for the case with flow rate of 120 ml/min

TC1		TC2		TC3		Cryoprobe	
102(Seconds)	102(C)	103(Seconds)	103(C)	104(Seconds)	104(C)	106(Seconds)	106(C)
0.064	37.3	0.109	37.9	0.155	37.6	0.246	37.9
10.072	37.3	10.118	37.8	10.163	37.6	10.255	31.5
20.076	37.2	20.122	37.7	20.167	37.5	20.259	21.0
30.088	37.1	30.133	37.7	30.179	37.4	30.27	6.2
40.094	36.9	40.139	37.5	40.185	37.4	40.276	-5.7
50.05	36.4	50.096	37.3	50.142	37.2	50.233	-16.1
60.063	35.9	60.108	37.0	60.154	37.1	60.245	-25.9
70.069	35.2	70.114	36.6	70.16	36.9	70.251	-35.0
80.067	34.3	80.112	36.1	80.158	36.7	80.249	-44.6
90.069	33.4	90.115	35.5	90.161	36.4	90.252	-54.2
100.073	32.3	100.119	34.9	100.164	36.2	100.256	-66.5
110.089	31.3	110.135	34.3	110.181	35.9	110.273	-76.1
120.05	29.8	120.096	33.4	120.142	35.5	120.233	-85.4
130.064	28.4	130.11	32.5	130.156	35.1	130.247	-93.3
140.079	26.8	140.125	31.4	140.17	34.7	140.262	-110.6
150.085	25.0	150.131	30.3	150.177	34.2	150.268	-137.8
160.095	23.0	160.141	29.0	160.187	33.7	160.278	-139.4
170.05	21.0	170.096	27.6	170.142	33.1	170.233	-144.7
180.067	18.7	180.112	26.1	180.158	32.5	180.249	-145.6
190.088	16.3	190.133	24.5	190.179	31.8	190.27	-138.3
200.048	13.8	200.094	22.8	200.14	31.1	200.231	-128.6
210.051	11.3	210.097	21.1	210.142	30.3	210.234	-146.0
220.059	8.6	220.105	19.2	220.15	29.5	220.242	-146.4
230.074	6.0	230.119	17.4	230.165	28.5	230.258	-146.4
240.077	4.1	240.123	15.6	240.169	27.6	240.26	-146.3
250.086	2.5	250.131	13.9	250.177	26.6	250.268	-146.1
260.048	1.0	260.094	12.1	260.139	25.7	260.231	-146.5
270.053	-0.4	270.099	10.3	270.145	24.7	270.236	-147.1
280.066	-1.7	280.112	8.4	280.158	23.7	280.249	-147.4
290.083	-2.8	290.131	6.7	290.177	22.8	290.268	-147.5
300.099	-3.9	300.145	5.2	300.191	22.0	300.282	-147.6
310.055	-4.9	310.1	4.1	310.146	21.2	310.237	-147.5
320.064	-5.9	320.11	3.2	320.156	20.3	320.247	-147.8
330.07	-6.9	330.116	2.2	330.161	19.5	330.253	-147.8
340.07	-7.8	340.116	1.3	340.162	18.6	340.253	-147.9
350.084	-8.8	350.129	0.3	350.175	17.6	350.266	-148.0
360.096	-9.6	360.142	-0.5	360.187	16.7	360.279	-147.9
370.051	-10.4	370.097	-1.4	370.142	15.8	370.234	-147.6
380.049	-11.2	380.095	-2.2	380.14	14.9	380.232	-147.6

390.065	-12.0	390.111	-3.0	390.156	14.0	390.248	-147.5
400.065	-12.6	400.111	-3.7	400.156	13.1	400.248	-147.9
410.085	-13.3	410.131	-4.4	410.177	12.2	410.268	-147.7
420.096	-13.9	420.142	-5.1	420.188	11.3	420.279	-147.8
430.048	-14.5	430.094	-5.7	430.139	10.5	430.231	-147.6
440.064	-15.1	440.11	-6.3	440.156	9.5	440.247	-147.5
450.075	-15.6	450.121	-6.9	450.167	8.6	450.258	-147.6
460.081	-16.2	460.127	-7.5	460.173	7.7	460.264	-147.7
470.087	-16.6	470.133	-8.0	470.179	6.9	470.27	-147.9
480.092	-17.2	480.137	-8.5	480.183	6.1	480.275	-147.8
490.048	-17.6	490.094	-9.0	490.139	5.3	490.231	-148.2
500.064	-18.1	500.11	-9.5	500.156	4.7	500.247	-148.5
510.074	-18.5	510.12	-10.0	510.166	4.1	510.257	-148.7
520.096	-18.9	520.141	-10.4	520.187	3.7	520.279	-148.8
530.051	-19.3	530.097	-10.9	530.142	3.2	530.234	-148.2
540.059	-19.7	540.105	-11.3	540.15	2.8	540.241	-148.1
550.073	-20.1	550.118	-11.6	550.164	2.3	550.255	-148.1
560.084	-20.4	560.13	-12.0	560.176	1.9	560.267	-148.5
570.092	-20.6	570.138	-12.3	570.184	1.5	570.275	-148.9
580.057	-20.8	580.103	-12.4	580.149	1.3	580.24	-149.0
590.071	-21.0	590.117	-12.7	590.163	0.9	590.254	-148.9
600.088	-21.3	600.134	-13.1	600.179	0.6	600.271	-148.2
610.056	-21.7	610.102	-13.4	610.147	0.3	610.239	-148.5
620.066	-22.0	620.111	-13.8	620.157	-0.1	620.249	-148.8
630.074	-22.4	630.119	-14.1	630.165	-0.5	630.257	-149.1
640.088	-22.7	640.133	-14.4	640.179	-0.8	640.27	-149.2
650.052	-23.0	650.098	-14.8	650.144	-1.1	650.235	-148.5
660.062	-23.3	660.108	-15.1	660.154	-1.4	660.245	-148.7
670.082	-23.6	670.128	-15.4	670.175	-1.8	670.266	-149.0
680.096	-23.9	680.142	-15.7	680.188	-2.1	680.279	-149.3
690.051	-24.2	690.096	-16.0	690.142	-2.4	690.233	-149.2
700.061	-24.5	700.108	-16.3	700.154	-2.7	700.245	-148.5
710.071	-24.7	710.117	-16.5	710.162	-3.0	710.254	-149.2
720.073	-24.9	720.119	-16.7	720.164	-3.3	720.256	-149.4
730.086	-25.1	730.132	-17.0	730.178	-3.5	730.269	-148.7
740.098	-25.3	740.144	-17.2	740.19	-3.8	740.281	-148.9
750.06	-25.6	750.105	-17.5	750.151	-4.1	750.242	-149.7
760.068	-25.7	760.113	-17.7	760.159	-4.3	760.25	-148.8
770.093	-25.9	770.139	-17.9	770.184	-4.6	770.276	-149.0
780.052	-26.1	780.098	-18.0	780.143	-4.8	780.235	-149.5
790.073	-26.2	790.118	-18.2	790.164	-5.0	790.255	-148.8
800.087	-26.4	800.132	-18.4	800.178	-5.2	800.269	-149.1
810.048	-26.6	810.094	-18.6	810.139	-5.4	810.231	-149.9
820.057	-26.7	820.102	-18.8	820.148	-5.6	820.239	-149.0
830.084	-26.9	830.13	-18.9	830.175	-5.8	830.267	-149.1

840.096	-27.1	840.142	-19.1	840.187	-6.0	840.278	-149.8
850.053	-27.3	850.099	-19.3	850.144	-6.3	850.236	-148.9
860.087	-27.5	860.133	-19.5	860.178	-6.5	860.27	-149.3
870.048	-27.6	870.094	-19.7	870.139	-6.7	870.231	-150.1
880.066	-27.8	880.113	-19.9	880.159	-6.8	880.252	-149.0
890.087	-27.9	890.133	-20.0	890.179	-7.0	890.27	-149.3
900.048	-27.9	900.094	-20.0	900.139	-7.2	900.231	-149.9
910.064	-28.1	910.109	-20.2	910.155	-7.3	910.246	-149.1
920.073	-28.2	920.119	-20.4	920.165	-7.5	920.257	-149.6
930.048	-28.4	930.094	-20.5	930.139	-7.6	930.231	-149.8
940.054	-28.5	940.1	-20.7	940.146	-7.8	940.237	-149.4
950.072	-28.7	950.118	-20.8	950.163	-8.0	950.255	-150.1
960.095	-28.8	960.141	-21.0	960.187	-8.2	960.278	-149.2
970.058	-29.0	970.104	-21.2	970.15	-8.4	970.241	-150.0
980.066	-29.1	980.112	-21.3	980.158	-8.5	980.249	-149.4
990.078	-29.3	990.124	-21.5	990.169	-8.7	990.261	-149.5
1000.091	-29.4	1000.136	-21.6	1000.182	-8.9	1000.273	-149.7
1010.048	-29.5	1010.094	-21.7	1010.14	-8.9	1010.231	-149.7
1020.063	-29.6	1020.109	-21.8	1020.155	-9.1	1020.246	-150.0
1030.088	-29.7	1030.134	-21.9	1030.18	-9.2	1030.271	-149.5
1040.058	-29.8	1040.104	-22.0	1040.149	-9.3	1040.241	-150.0
1050.067	-29.9	1050.113	-22.1	1050.159	-9.5	1050.25	-149.3
1060.083	-30.0	1060.128	-22.2	1060.174	-9.6	1060.266	-150.2
1070.092	-30.1	1070.137	-22.3	1070.183	-9.7	1070.275	-149.4
1080.048	-30.2	1080.094	-22.5	1080.139	-9.9	1080.231	-150.1
1090.07	-30.3	1090.115	-22.6	1090.161	-10.0	1090.253	-149.3
1100.093	-30.4	1100.139	-22.7	1100.184	-10.1	1100.276	-150.2
1110.05	-30.5	1110.096	-22.8	1110.142	-10.2	1110.233	-149.4
1120.068	-30.6	1120.114	-22.9	1120.159	-10.3	1120.251	-150.1
1130.09	-30.7	1130.135	-23.0	1130.181	-10.4	1130.272	-149.5
1140.102	-30.8	1140.148	-23.1	1140.193	-10.6	1140.285	-150.2
1150.061	-30.9	1150.107	-23.2	1150.152	-10.7	1150.244	-149.7
1160.086	-31.1	1160.132	-23.3	1160.178	-10.8	1160.269	-150.6
1170.048	-31.2	1170.094	-23.5	1170.139	-11.0	1170.231	-150.0
1180.061	-31.3	1180.107	-23.6	1180.153	-11.1	1180.244	-150.3
1190.079	-31.4	1190.125	-23.7	1190.171	-11.2	1190.263	-149.9